Master's thesis

NTNU
Norwegian University of Science and Technology
Faculty of Natural Sciences
Department of Physics

Tor Inge Thorsen

Heterostructured GaAs/GaAsSb nanowires characterized by scanning precession electron microscopy

Master's thesis in MSPHYS
Supervisor: Antonius T.J. van Helvoort
June 2020

Norwegian University of Science and Technology

NORGES TEKNISK-NATURVITENSKAPELIGE UNIVERSITET

FY4900 MASTER OF SCIENCE IN PHYSICS

Heterostructured GaAs/GaAsSb nanowires characterized by scanning precession electron microscopy

- Tor Inge Thorsen

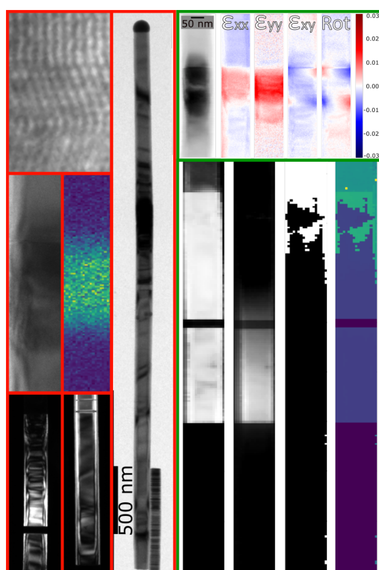

June 15, 2020

Cover image: Collage of results including HRTEM, DFTEM, BFTEM, EDS measurements, VDF, phase mapping using template matching and NMF and strain measurements.

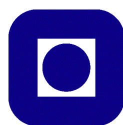

NTNU
Norwegian University of
Science and Technology

Abstract

III-V semiconductor nanowires can be the basis for future optoelectronic devices. To optimise the synthesis and properties, the structural characteristics have to be determined. In this thesis the crystal structure, orientation, composition and strain in heterostructured GaAs/GaAsSb nanowires are studied. Conventional transmission electron microscopy (TEM) techniques are applied including high-resolution transmission electron microscopy (HRTEM) imaging, bright-field (BF) and dark-field (DF) imaging and selective area electron diffraction techniques for structural characterisation. The nanowires include both the zink-blende and the wurtzite structure, each with typical stacking faults. The same nanostructures can be studied by scanning (precession) electron diffraction (S(P)ED). This collects a stack of diffraction patterns by raster scanning the studied material with a nm-sized, focused (precessed) electron beam probe. Structural characteristics can then be obtained by using post-processing routines available in the open-source pyXem package. The conventional TEM imaging techniques outperforms the S(P)ED routine when a high spatial resolution is central through HRTEM imaging. However, S(P)ED allows for large areas to be studied and semiautomatic analysis of crystal phases and crystal orientations to be used. Post processing gives flexibility, as for example in virtual dark-field imaging relative to conventional dark-field imaging in the TEM. The SPED data stacks allow for template matching against candidate phases and unsupervised machine learning which are not possible for conventional TEM. The analysis of larger areas however is hampered by bending of the nanowires. Overall the amount of data that can be extracted in post-processing routines from a single scan make it a valuable tool for crystal characterisation at the nm-scale.

Strain at heterostructure interfaces affect the materials properties but are not easy to quantify using conventional TEM techniques. From SPED data stacks, the strain can be analysed from relative shifts in selected reflections in these data stacks. In this study strain measurements are performed around axially inserted heterostructures of GaAsSb in GaAs nanowires. Experimental conditions like beam convergence angle, camera length, orientation and choice of reflections are systematically varied to determine which settings result in the most trustworthy strain maps. It is found that, precession and a small convergence angle result in reflections with a more even intensity which is crucial for determining the sub-pixel position of a reflection through a center-of-mass approach. Using reflections as far out in reciprocal space as possible before the signal-to-noise limits the final results are found to be optimum. For this reason improved results are expected through the use of a larger direct electron detector with less noise compared to acquiring patterns indirectly as done in the present study by images from a fluorescence screen using an optical camera.

Sammendrag

III-V halvleder nanotråder kan være basisen for fremtidens optoelektroniske enheter. For å omptimalisere syntesen og egenskaper må strukturelle karakteristikker bestemmes. I denne oppgaven har krystall strukturen, orientering, komposisjon og mekaniske spenninger i krystallstrukturen for GaAs/GaAsSb nanotråder blitt studert. Til dette blir konvensjonelle transmisjons elektron mikroskopi (TEM) teknikker brukt som inkluderer høyoppløsnings transmisjons elektron mikroskopi (HRTEM), lysefelts (BF) og mørkefelts (DF) bilder og selektivt område elektron diffraksjon teknikker for strukturell karakterisering. Nanotrådene opptrer i både zink-blende og wurtzite struktur som hver har sine typiske stable feil. De samme nanostrukturene kan bli studert med skannende (presesjons) elektron diffraksjon (S(P)ED). Denne prosedyren samler en stabel med diffraksjonsmønster ved å skanne det studerte materialet med en fokusert (preseserende) elektron stråle på størrelse med noen få nm. Strukturelle karakteristikker kan da bli funnet gjennom prosessering av dataen ved hjelp av rutiner som er tilgjengelige i en åpen kilde kode kalt pyXem. Konvensjonelle TEM teknikker utkonkurrerer S(P)ED når det kommer til høy oppløsning gjennom HRTEM bilder. S(P)ED derimot kan gjøres over større områder og halv-automatiske prosedyrer kan brukes for å studere krystall faser og orienteringer. Etterbehandling av samlet data gir fleksibilitet, gjennom for eksempel virtuell mørkefelt relativt den konvensjonelle mørkefelt metoden i en TEM. SPED dataen kan bukes til sammenligning med mal, hvor diffraksjonsmønstrene sammenlignes mot simulerte kandidat faser, og uovervåket maskinlæring som ikke er mulig med konvensjonelle TEM teknikker. Analysen av større områder kan derimot få problemer når nanotrådene er bøyd. Mengden data som kan hentes i etterbehandlings rutiner fra en enkelt skanning gjør at SPED er et verdifullt verktøy for krystall karakterisering på nm nivå.

Mekaniske spenninger i krystallstrukturen ved heterostrukturer påvirker materialets egenskaper men er ikke enkle å tallfeste med konvensjonelle TEM teknikker. Fra SPED data kan dette bli analysert fra relative forflytninger av bestemte refleksjoner i dataen. I denne studien blir målinger av mekanisk spenning i krystallstrukturen rundt aksialt innsatte heterostrukturer av GaAsSb i GaAs nanotråder utført. Eksperimentelle verdier som konvergens vinkel til elektron strålen, kamera lengde, orientering og valg av refleksjoner vil bli systematisk variert for å bestemme hvilke innstillinger som resulterer i best resultat. Det blir funnet at presesjon og en liten konvergens vinkel gir refleksjoner med en mer uniform intensitet som er avgjørende for å bestemme sub-pixel posisjonen for en refleksjon gjennom en massesenter metode. Ved å bruke refleksjoner så langt ute i det resiproke rom som mulig, før signalet blir for svakt oppnås bedre resultater. Av denne grunn er det forventet at bedre resultater kan oppnås med en større direkte elektron detektor hvor det vil være mindre støy sammenlignet med den indirekte metoden som blir brukt i denne studien fra en fluorescende skjerm ved hjelp av et optisk kamera.

Preface

This thesis is submitted to the Norwegian University of Science and Technology (NTNU) as the final part of my M.Sc degree in Physics. The experimental work has been done at the TEM Gemini Centre. All work presented have been done by me, both experimental data acquisition and data processing, unless otherwise explicitly stated. The crystal visualisation and TEM theory also use my own results.

I would like to give my thanks to my brilliant supervisor Professor Antonius T. J. van Helvoort. Our discussions and routinely meetings have been of great help for completing my work. He always showed great interest in my problems and have given me generous amounts of help at all hours of the day, all days of the week towards the end. Completing the masters have been a trial at times but our discussions always left me feeling hungry to get back to work. I greatly appreciate having been given the opportunity to work together. I would also like to give a special thanks to Post doctoral researcher Dipanwita Chatterjee for helpful discussions and feedback on my work. I am also grateful to senior engineers Ragnhild Sæterli and Bjørn Soleim for teaching me the operation of the TEM and always being helpful when I encountered problems. Finally, a thanks to the entire TEM group here at NTNU for being very welcoming and willing to help. The talks given by fellow students and PhDs on Fridays have been very interesting and inspiring.

Table of Contents

Summary i

Sammendrag i

Preface ii

Table of Contents vi

Abbreviations vii

1 Introduction 1

2 Theory 5

2.1 Crystalline materials 7

2.2 Stacking and crystal phases 9

2.3 Crystal growth 10

2.4 Defects 11

2.5 Reciprocal space 12

2.6 TEM introduction 13

2.7 Electron-matter interaction in a TEM 14
2.8 Diffraction 15
2.9 Structure factor 17
2.10 Diffraction Patterns 18
2.11 Intensity 21
2.12 TEM mechanics 22
2.12.1 The condenser lens system 24
2.12.2 The objective lens system 25
2.12.3 The intermediate and projector lens system 26
2.13 Bright-Field and Dark-Field 26
2.14 Kikuchi lines 27
2.15 Scanning Precession Electron Diffraction 28
2.15.1 Virtual imaging 29
2.15.2 Template matching 29
2.15.3 Non-negative Matrix Factorisation 30
2.15.4 Strain measurements 30
2.16 EDS 31

3 Experimental **33**
3.1 Material growth and specimen preparation 35
3.2 TEM 35
3.3 Scanning Precession Electron Diffraction 36
3.4 EDS 36
3.5 Simulations and data processing 36

4 Results **37**

4.1 Crystal structure 39
4.2 Orientation 46
4.3 Composition 48
4.4 Strain 49

5 Discussion **53**

5.1 Crystal structure 55
5.2 Orientation 60
5.3 Composition 61
5.4 Strain 62

6 Conclusion **69**

7 Future work **71**

7.1 Ideal nanowire strain measurements 71
7.2 Additional convergence angles 72
7.3 Routine characterisation 72
7.4 Beyond nanowires 72

Bibliography **72**

Appendix **77**

A Scan step calibration 77
B SPED diffraction calibration 78
C Convergence angle (α) calibration 80
D Precession angle (ϕ) calibration 81
E Camera length calibration 82
F SPED camera pixel width calibration 83

G Fast Fourier transform of high-resolution TEM images 84

H Crystal orientation from Ewald sphere considerations 84

I Additional strain maps 85

J Code for convergence angle determination 86

K Code for determining camera length for desired reflection 88

L Code for pre processing SPED data 90

M Code for crystal characterisation 91

N Code for strain mapping 95

O Code for EDX mapping 99

P Other smaller calibration codes 103

Abbreviations

1D one-dimensional

2D two-dimensional

AP aperture

BF bright-field

CCD charge-coupled device

CIF crystallographic information file

CBED convergent beam electron diffraction

DF dark-field

DP diffraction pattern

EDX energy dispersive X-ray spectroscopy

EDS energy dispersive X-ray spectroscopy

FOLZ first-order Laue zone

FEG field-emission gun

FFT fast Fourier transform

GPA geometrical phase analysis

HOLZ higher-order Laue zone

HAADF high-angle annular dark-field

HRTEM high-resolution transmission electron microscopy

MBE molecular beam epitaxy

NW nanowires

NMF non-negative matrix factorization

NBED nanobem electron diffraction

QW quantum well

SOLZ second-order Laue zone

SC simple-cubic

SAED selective area electron diffraction

SF stacking fault

SDD silicon-drift detector

SAG selective-area growth

SPED scanning precession electron diffraction

STEM scanning transmission electron microscopy

TEM transmission electron microscopy

TPL triple-phase-line

VLS vapor-liquid-solid

VS vapor-solid

VBF virtual bright-field

VDF virtual dark-field

WZ wurtzite

ZOLZ zeroth-order Laue zone

ZB zink-blende

Chapter 1

Introduction

Semiconductor nanowires (NW) have the potential to allow for great advances in electronic components. In solar cells they can provide a low cost solution as the restrictions on material quality can be relaxed and the amount of material needed reduced relative to conventional solar cells [1]. For use in transistors it can allow further advances in scaling of MOSFETs and improved device performance [2]. In LEDs the NWs one-dimensional (1D) structure have the potential to increase the overall efficiency and colour purity relative to planar two-dimensional (2D) thin films [3]. The direct band gap of III-V compounds such as GaAs make them promising for optoelectronic devices as this results in strong optical response in the material. For high performance and high efficiency devices these compounds have received a lot of interest [4]. Therefore much research has been done on the growth of III-V NWs and the control of their properties. This has led to rapid progress in the understanding and application of these NWs in recent years [5].

It is possible to tune the properties of III-V materials by introducing hetero structures within the NWs where some of the group III atoms are exchanged for another group III atom (or similar for the group V atoms). This can be used to alter the band gap, mediate a transition from growth substrate to a desired active material, creating a specific active segment and much more [6, 7]. Sb has received interest in this regard for GaAs materials where it can take the place of As atoms creating $GaAs_{1-y}Sb_y$ (hereafter denoted GaAsSb). III-Sb compound semiconductors have a high carrier mobility and when Sb in introduced into GaAs NWs, band gaps can be tuned in the range of $0.813 - 1.43$ eV [8]. But GaSb has a larger lattice parameter than GaAs and so this substitution introduces strain in GaAs/GaAsSb heterostructures. The small dimensions of the NWs allow for some relaxationwhich can help to reduce defects introduced by the strain [9]. However, strain will still be present and can affect the growth of NWs and the local bandgap [10]. Sometimes these effects can be utilised, in GaAs/GaAsSb materials it has for example been found that the band gap transition in thin films can be controlled by the amount of strain [10]. If this

is to be used in NWs as well, it is important to be able to determine the strain in these which is practically difficult.

NWs are small with a typical diameter of $10 - 200$ nm and a length of a few μm, heterostructures within will logically be even smaller. transmission electron microscopy (TEM) is one of the most essential characterisation tools for determining the morphology, crystal structure and composition of a material on these small scales. TEM can be used to determine local crsytallography through diffraction pattern (DP)s and high-resolution transmission electron microscopy (HRTEM) images. These can reveal structural details like stacking faults and twin planes on a close to atomic level resolution. The composition of materials can be analysed from energy dispersive X-ray spectroscopy (EDS) measurements [11] and quantitative high-angle annular dark-field (HAADF) scanning transmission electron microscopy (STEM) [12]. TEM is an essential part of NW research, but strain, despite its importance to all kind of properties, is relatively seldom included in routine characterisation studies. This is because measuring strain is a more demanding process.

There are several techniques that can be used for strain measurements. X-ray diffraction is one, but this has a spatial resolution in the order of hundreds of nanometers [13]. This is too large for the study of single NWs and heterostructures within them. These are better studied with electron based techniques due to the higher spatial resolution achievable. An initial view of the strain present in a NW can be found through analysing the contrast in bright-field (BF) and dark-field (DF) imaging, but only to a qualitative degree [14]. Higher resolution images can be used to quantify strain from deviations in lattice images through a routine called geometrical phase analysis (GPA) [15]. To perform this, HRTEM images with an atomic resolution are required. This results in a small field of view and a high dependence on specimen orientation to obtain images of sufficient quality. At the cost of spatial resolution, a much higher field of view can be obtained through a method called nanobem electron diffraction (NBED) [16]. Here a small, close to parallel, electron beam is used to obtain DPs. By scanning the probe across the sample, a stack of DPs is created from which the lattice spacings can be found for a larger area of the sample. The DP stack then have be analysed in post-processing to calculate strain from changes in reflection positions. But in order to get good quality DPs the beam needs to be close to parallel which limits the spatial resolution of this method [16]. By focusing the electron beam on the sample, a higher spatial resolution can be achieved, but the range of incoming angles broadens the reflections in the obtained DPs and an uneven intensity is observed within the reflections. For thicker specimen this leads to additional features that allow accurate lattice parameter determination through a method called convergent beam electron diffraction (CBED) [14], but NWs are typically too thin for this to be used in strain analysis. These same features cause intensity variations within reflections and complicate the determination of reflection positions. However, there exists a workaround for this problem. By introducing a precession of the electron beam, the intensity of the reflections can be made more even. This is performed in the measurement technique called scanning precession electron diffraction (SPED). This technique can achieve smaller spatial resolution than NBED through a focused electron beam whilst maintaining good quality DPs by precession [16]. This also increase the field of view in reciprocal space, making more reflections available for analysis. To date SPED measurements of strain in NWs are hardly

reported but some early measurements have been performed which show the potential [17]. The SPED procedures are not common in electron microscopes and typically utilise an external in-direct image collection of DPs. Post-processing routines for SPED data has recently become available through an open-source package called pyXem [18]. Routines for crystal phase and orientation analysis are also available in this package. In this thesis SPED measurements will be performed on GaAs NWs with axial heterostructures of GaAsSb. The phases, orientations and composition of the NWs will be studied using both SPED measurements and conventional TEM methods for comparison and to complement the structural characterization of these nanostructures.

In chapter two background theory for crystalline materials and the crystal phases relevant for the studied NWs are presented. An introduction to the TEM and its different components and working principle is given. Some common measurement techniques for TEM will be explained and post-processing routines for SPED measurements. The experimental details of the work is given in chapter three. Chapter four presents the results where phase, orientation, composition and strain results are presented. The same topics will be discussed in chapter five and chapter six gives the conclusions. Finally, suggestions for further TEM based characterisation of heterostructured NWs are given based on work done in this study. Important calibrations, pre-processing steps and calculations performed are given in the appendices.

Chapter 2

Theory

2.1 Crystalline materials

The following text on crystalline materials is based on an introductory book on Solid State Physics by Kittel [19]. Ideal crystals have a long range order which can be described by a lattice convoluted with groups of atoms placed on each lattice point. These atom groups are called the basis of the lattice. In three dimensions the crystal lattice can be described by three vectors, typically called $\mathbf{a_1}$, $\mathbf{a_2}$ and $\mathbf{a_3}$. These vectors define the crystal axes and make up the unit cell of the crystal structure. If the vectors $\mathbf{a_i}$ are chosen such that they form the cell with the smallest possible volume, the vectors are called the primitive translation vectors and form the primitive unit cell.

A translation within the crystal from a point $\mathbf{r}$ by a combination of an integer number of the translation vectors will give a new position $\mathbf{r}'$ whose surroundings look identical to the previous.

$$\mathbf{r}' = \mathbf{r} + n_1\mathbf{a}_1 + n_2\mathbf{a}_2 + n_3\mathbf{a}_3 \tag{2.1}$$

n_1, n_2 and n_3 in the equation above are integers. Once the crystal lattice is defined the atom positions within the unit cell, making the basis, can be determined. The distance from a lattice point to an atom i can be written as

$$\mathbf{r_i} = x_i\mathbf{a}_1 + y_i\mathbf{a}_2 + z_i\mathbf{a}_3 \tag{2.2}$$

In three dimensions there are 14 different types of lattice systems that can be subcategorized into 7 types of cells; triclinic, monoclinic, orthorhombic, tetragonal, cubic, trigonal and hexagonal. The III-V NWs of interest in this study crystallize in cubic and hexagonal systems and so those will be explained in further detail. For the cubic structure, three crystal axes are used as seen in Figure 2.1a. These axes are perpendicular to each other and $|\mathbf{a_1}| = |\mathbf{a_2}| = |\mathbf{a_3}| = a$. The angles between them are called α, β, γ also seen in Figure 2.1a. The hexagonal structure can also be described by three crystal axes, but it is common to use four as seen in Figure 2.1b. Here $|\mathbf{a_1}| = |\mathbf{a_2}| = a$ and the angle

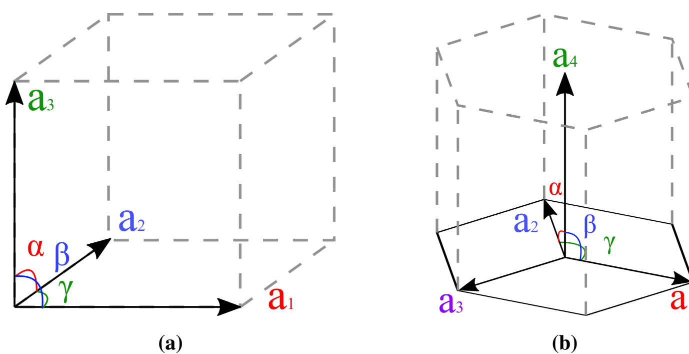

Figure 2.1: (a) Unit vectors $\mathbf{a_i}$ making a unit cell for the cubic structure (b) Crystal axes for hexagonal structure using four vectors.

between them $\gamma = 120°$. The additional vector is defined as $\mathbf{a}_3 \equiv \overline{(\mathbf{a}_1 + \mathbf{a}_2)}$ and is added for convenience when describing crystal orientations. The last axis $\mathbf{a}_4$ is perpendicular to the other three axes and is commonly referred to as $\mathbf{c}$.

The crystal orientation and planes of atoms are described using Miller indices. The Miller indices of a plane are defined as the smallest integer numbers of the reciprocals of the points at which the plane intercepts the crystal axes. The interception points are given in units of the lattice constants. For the cubic crystal structure, described by three crystal axes, these points make a specific plane named (hkl). General planes are denoted as $\{hkl\}$. Specific directions in the crystal are labelled $[hkl]$ (and general directions by $\langle hkl \rangle$). In the cubic system the $[hkl]$ direction is perpendicular to the corresponding (hkl) plane. For the hexagonal crystal structure with four crystal axes the planes in the crystal are named $\{hkil\}$ and the directions $\langle hkil \rangle$ where $i = \overline{(h+k)}$. The convenience of this notation can be seen when comparing for example the planes (110) and $(\bar{2}10)$ in the hcp wurtzite (WZ) structure. These planes are actually symmetrically equivalent, but this is not directly obvious using the three index notation. When described with the four axis system the same planes would be named $(11\bar{2}0)$ and $(\bar{2}110)$. This makes the symmetrical relationship immediately apparent.

When studying and characterising crystal structures, the distance d_{hkl} from the central beam to a $\{hkl\}$ plane is used. For the cubic system the distance is calculated through the following equation:

$$\frac{1}{d_{hkl}^2} = \frac{h^2 + k^2 + l^2}{a_0^2}, \tag{2.3}$$

and for the hexagonal structure it becomes

$$\frac{1}{d_{hkl}^2} = \frac{4}{3}\left(\frac{h^2 + hk + k^2}{a_0^2}\right) + \frac{l^2}{c^2}. \tag{2.4}$$

Also the angle between planes and directions is important in the characterisation process. Again the formula is different for the two crystal structures. For the angle φ_{12} between two directions 1 and 2 in the cubic structure we have

$$\cos\varphi_{12} = \frac{h_1h_2 + k_1k_2 + l_1l_1}{\sqrt{h_1^2 + k_1^2 + l_1^2}\sqrt{h_2^2 + k_2^2 + l_2^2}}, \tag{2.5}$$

and for the hexagonal structure

$$\cos\varphi_{12} = \frac{h_1h_2 + k_1k_2 + i_1i_1 + \lambda^2 l_1l_2}{\sqrt{h_1^2 + k_1^2 + i_2^2 + \lambda^2 l_1^2}\sqrt{h_2^2 + k_2^2 + l_2^2\lambda^2 l_2^2}} \tag{2.6}$$

where $\lambda^2 = \frac{2c^2}{3a^2}$ [20].

2.2 Stacking and crystal phases

III-V NWs crystallise in layers with a symmetry that can be described by Figure 2.2. The layers can have 3 different positions relative to each other, called A, B and C in the figure. If the layers are stacked as an A layer first and then a B layer on top of that and repeated as ABABAB... it results in a structure called WZ. The WZ structure can be described as a

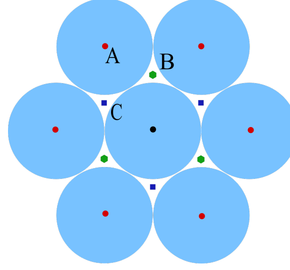

Figure 2.2: The three possible positions of close packed layers seen from the top. The figure is adapted from [19].

combination of two hcp lattices. The first containing atom type a is placed at $(\frac{1}{3}, \frac{2}{3}, 0)$ and the second with atom b is placed at $(\frac{1}{3}, \frac{2}{3}, u)$. The displacement u is along the **c**-axis (or $[0001]$ direction) and is material dependent (For GaAs NWs $u \approx 0.373$ [11]). The result is a lattice with 4 atoms in the unit cell as depicted in Figure 2.3a. The positions of the atoms in the basis of the WZ cell are

$$\begin{aligned} a: \quad & r_1 = (1/3, 2/3, 0), \quad r_2 = (2/3, 1/3, 1/2), \\ b: \quad & r_3 = (1/3, 2/3, u), \quad r_4 = (2/3, 1/3, 1/2 + u). \end{aligned}$$

The WZ structure can also be defined as belonging to space group $P6_3mc$ with atoms in Wyckoff position b $(\frac{1}{3}, \frac{2}{3}, 0)$ and $(\frac{1}{3}, \frac{2}{3}, u)$.

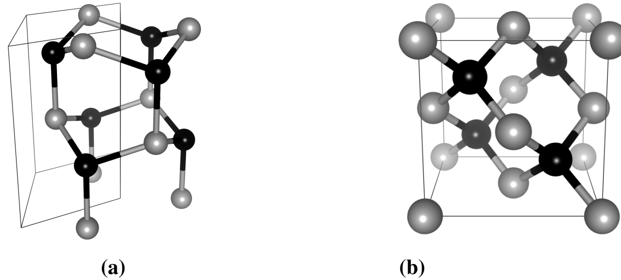

(a) **(b)**

Figure 2.3: (a) The unit cell of the WZ crystal structure seen through zone axis $[401]$ (b) The unit cell of the zink-blende (ZB) crystal structure seen through zone axis $[401]$. For GaAs, white atoms represent Ga and black As.

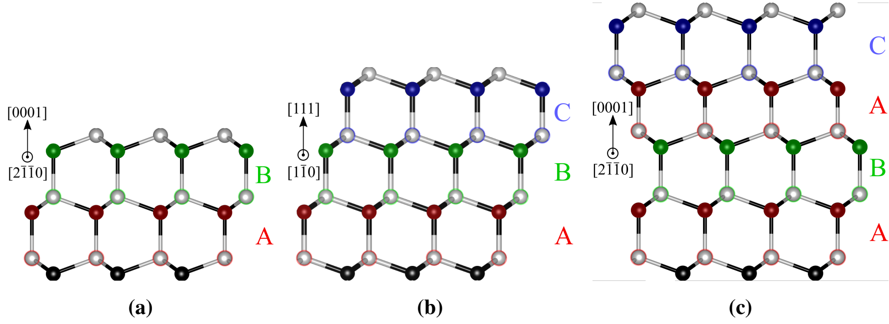

Figure 2.4: (a) 2H stacking sequence of the WZ structure, (b) 3C stacking sequence of the ZB structure and (c) 4H stacking sequence.

The AB stacking of WZ is called 2H. Another, often seen, possible stacking sequence is ABAC, called 4H stacking. A model of this can be seen in Figure 2.4c. The fcc ZB structure is obtained from a stacking sequence of ABC. This ABC stacking is also called 3C and the crystallization then happens in the $[111]$ direction of the ZB structure. These three stacking sequences are depicted in Figure 2.4 for comparison. When describing the ZB structure it is conventional to use the primitive translation vectors of a simple-cubic (SC) structure along the lengths of the cube in Figure 2.3b. This choice of axes make up the conventional cell for ZB [19] and is what will be used in this study. For the ZB structure there are 8 atoms in the basis of the conventional cell as seen in Figure 2.3b. As for the WZ structure this too can be seen as a combination of two lattices, in this case two fcc structures. The first contain atoms of type a and the second atoms of type b, where the second lattice is displaced by $({}^1/_4, {}^1/_4, {}^1/_4)$ relative to the first. The positions of the atoms a and b in the conventional cell are

$$
\begin{aligned}
a:\quad & r_1 = (0,0,0), && r_2 = ({}^1/_2, {}^1/_2, 0), && r_3 = ({}^1/_2, 0, {}^1/_2), && r_4 = (0, {}^1/_2, {}^1/_2),\\
b:\quad & r_5 = ({}^1/_4, {}^1/_4, {}^1/_4), && r_6 = ({}^3/_4, {}^3/_4, {}^1/_4), && r_7 = ({}^3/_4, {}^1/_4, {}^3/_4), && r_8 = ({}^1/_4, {}^3/_4, {}^3/_4).
\end{aligned}
$$

For the GaAs NWs studied $a =$ Ga and $b =$ As. The ZB structure can be more densely described as belonging to the space group $F\bar{4}3m$ with atoms in Wyckoff positions a $(0,0,0)$ and b $(\frac{1}{4}, \frac{1}{4}, \frac{1}{4})$.

2.3 Crystal growth

There are a multitude of techniques available for growing nanowires. One of the most common methods used is the vapor-liquid-solid (VLS) method developed by Wagner and Ellis in 1964 [21]. This method starts with a liquid metal droplet placed on a crystalline substrate. The droplet acts as a catalyst for the crystallisation of the NW. A precursor is then heated to a temperature at which it evaporates. This vapor is introduced to the droplet where is is absorbed and crystallise in the contact area, or the triple-phase-line

(TPL), between the liquid droplet and the solid substrate/NW [22]. The growth of the NW happens by formation on mono-layers at the TPL. This starts at the edge of the TPL and works its way across the cross-section of the wire [23]. Gold droplets are one of the most used catalysts as this does not oxidize and works well with many precursors. But it is not suitable to make Si based devices [24]. And so other materials must be found for this purpose. For the growth of GaAs NWs, Ga droplets can be used. In this case some of the droplet will be consumed in the making of the NW and so the precursor vapor must contain both Ga and As so that the total flux of Ga for the droplet is zero. Another advantage of this is the ability to change the size and thus contact angle between the droplet and the NW by changing the Ga concentration in the vapor. Another way to avoid the use of a gold droplet is to not using a droplet at all. This method is commonly called vapor-solid (VS). The NWs can then start randomly on the substrate in what is called a self-assembled way or on selective spots imprinted on the substrate called selective-area growth (SAG). To perform these procedures one can use molecular beam epitaxy (MBE). This uses a vacuum chamber where the substrate is placed and introduced to the vaporised precursors. The precursors are heated in effusion cells pointing toward the substrate. The flux on the substrate can be controlled by changing the temperature of the effusion cells. The flux can also be rapidly closed by closing shutters in front of the cells [11]. quantum well (QW)s and core shells in NWs can be made during growth by changing the composition for a limited duration of the NW growth. If the new material has a different lattice parameter than the main material of the NW the resulting crystal will be strained. Strain can also be a result of external forces such as pressure or bending. The strain component of a NW, commonly denoted as ϵ, is defined as the change in an atom position relative to the unstrained atom position

$$\epsilon = \frac{\delta a}{a_0}. \tag{2.7}$$

The introduction of other materials in the NWs during the NW growth to create the QWs is a common cause for defects. In theory the QWs can provide qualities that are attractive for a specific application of the NWs. However, if defects and stacking faults are introduced as a result they could negate these advantages.

2.4 Defects

The III-V NWs are stable both in the ZB and the WZ phase. This can be used as an advantage to create desired properties for the NWs. But during growth, unintended stacking sequences can occur which might prove detrimental to the NW properties [4]. The most common defect observed in ZB is called twinning [11]. This corresponds to a rotation of the crystal structure about the $[111]_{ZB}$-direction by 60°. In terms of the stacking sequence it can be described as ABCAB$\underline{\text{C}}$BACBA where the underlined C-layer becomes a boundary layer of the twinning. Figure 2.5a shows a HRTEM image of a GaAs NW with ZB twinning present. For the WZ phase it is common with stacking faults where an extra layer is introduced [11]. This could lead to the stacking sequences AB$\underline{\text{ABC}}$BA...

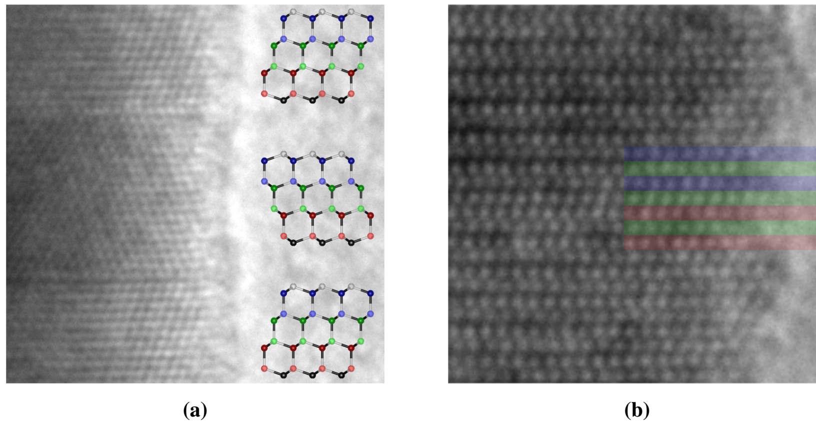

(a) (b)

Figure 2.5: (a) Twinning in the ZB phase of a GaAs NW seen through zone axis $[1\bar{1}0]_{ZB}$ (b) Single layer stacking fault in the WZ phase of an InGaN NW as ...AB<u>ABC</u>BC... In this process the stacking changes from ABAB to BCBC as marked in the figure with red, blue and green representing A, B and C layers respectively.

or AB<u>ABC</u>BC... both having a ZB segment of type ABC in them. This last case can be seen in Figure 2.5b. Similarly it could be AB<u>ACB</u>AB... or AB<u>ABC</u>BC... where the ZB segment ACB is a twinned version of the ABC sequence. Longer segments of stacking faults can occur in the WZ phase as well, but if they extend beyond two ZB segments, ABCABC, it is considered to be a region with ZB phase rather than a stacking fault [11].

2.5 Reciprocal space

With every crystal structure there are two lattices of importance. This is the crystal lattice in real space, as explained in the beginning of this chapter, and the lattice in reciprocal space. The reciprocal lattice is useful to explain diffraction in crystals which will be described in section 2.8. It is also important to understand when interpreting a DP. The reciprocal lattice can be described by reciprocal crystal axes defined as

$$\mathbf{b}_i = 2\pi \frac{\epsilon_{ijk}\mathbf{a}_j \times \mathbf{a}_k}{\mathbf{a}_1 \cdot \mathbf{a}_2 \times \mathbf{a}_3}, \tag{2.8}$$

using Einstein notation. This means that

$$\mathbf{b}_i \cdot \mathbf{a}_j = 2\pi\delta_{ij}, \tag{2.9}$$

where δ_{ij} is the Kroenecker delta. Using these definitions a vector $\mathbf{r}^*$ between two points in the reciprocal space can be written as

$$\mathbf{r}^* = m_1\mathbf{b}_1 + m_2\mathbf{b}_2 + m_3\mathbf{b}_3, \tag{2.10}$$

where m_i are integers [19]. Every point in the reciprocal lattice is related to a plane (hkl) in the crystal lattice. We therefore define the reciprocal lattice vector to a point as

$$\mathbf{g}_{hkl} = h\mathbf{b}_1 + k\mathbf{b}_2 + l\mathbf{b}_3. \tag{2.11}$$

This vector is perpendicular to the corresponding (hkl) plane and has an inverse relation to the distances d_{hkl} between parallel planes (hkl) in the crystal lattice as

$$|\mathbf{g}_{hkl}| = \frac{1}{d_{hkl}} \tag{2.12}$$

The reciprocal space is also commonly referred to as the Fourier space of the crystal. This is because the reciprocal space share important relations with the Fourier components of the periodic properties of the crystalline material. As the electron density of the material is periodic it can be modelled by a Fourier series. For a one dimensional case this could be written as

$$n(x) = n_0 + \sum_p [C_p \cos(2\pi px/a) + S_p \sin(2\pi px/a)], \tag{2.13}$$

where p is an integer and C and S are constants. The resulting Fourier series have a periodicity of a as it should when describing the crystal structure and the term $2\pi p/a$ describes the points in the crystals reciprocal space. Expanding to three dimensions the equivalent Fourier expansion can be written as

$$n(\mathbf{r}) = \sum_{\mathbf{g_{hkl}}} n_{\mathbf{g_{hkl}}} e^{i\mathbf{g_{hkl}}\cdot\mathbf{r}} \tag{2.14}$$

where g_{hkl} determine the allowed terms in the Fourier expansion and thus represent the the reciprocal lattice vectors described above making up the reciprocal crystal space [19].

2.6 TEM introduction

In this thesis a TEM is used to study the crystal structure in NWs. The resolution of optical microscopes are limited by the wavelength of the photons used. In the TEM on the other hand, electrons are used. The electrons are excited to a high kinetic energy in an electron gun and directed to the material as an ionizing electron beam. The electrons can achieve very small wavelengths rendering it capable of resolving details down to an atomic level. The TEM can perform a lot of measurements, some of which will be explained further in section 2.12. Two of the most central measurements of the TEM is the HRTEM imaging and measurements of DPs. The HRTEM images are images of the crystal lattice in real space with a resolution that is high enough to distinguish different columns of atoms in the crystal. It is important to remember that these images are created through diffraction events as the electron beam propagates through the material and so caution should be taken when analyzing them. The DPs can be used to determine the phase of a material, its orientation,

strain measurements and more. The DP is essentially a projection of the reciprocal space of the crystal in its current orientation. To realise the potential of these measurement techniques and using them for measurements, some theory on electron matter interaction and diffraction events is necessary.

2.7 Electron-matter interaction in a TEM

When the specimen is illuminated by the electron beam in the TEM, a lot of secondary signals are generated in the interaction. Some of the signals are presented in Figure 2.6a. Perhaps the most important signals for studies in a TEM are the electrons that have been scattered in the forward direction due to Coulomb forces from the atoms in the sample. These are called forward scattered electrons and are used to create the DPs and HRTEM images in the TEM. The forward scattered electrons are scattered through small angles and depend very strongly on the crystal phase. [14]

Not all incoming electrons interact with the material. The chance for an electron to interact and scatter from an atom is described by its scattering cross section σ_{atom}. This can be found from the differential scattering cross section of the atom, $d\sigma/d\Omega$, which describes the scatterings angular distribution. These processes are modelled in Figure 2.6b. From this it can be shown that

$$\frac{d\sigma}{d\Omega} = \frac{1}{2\pi \sin\theta} \frac{d\sigma}{d\theta}, \tag{2.15}$$

and in turn that the scattering cross section of the atom is described by

$$\sigma_{atom} = \int_{\theta}^{\pi} d\sigma = 2\pi \int_{\theta}^{\pi} sin\theta d\theta. \tag{2.16}$$

For a particular specimen with N number of atoms per unit of volume the total scattering cross section per unit of length in the specimen can be described as

$$\sigma_{total} = N\sigma_{atom}, \tag{2.17}$$

where $N = N_0\rho/A$, where N_0 is Avogadros number, A the atomic weight and ρ the density of the specimen. Thus, we get

$$\sigma_{total} = \frac{N_0 \sigma_{atom} \rho}{A}. \tag{2.18}$$

The probability that an atom is scattered as it passes through a specimen of thickness t in the beam direction can then be found by multiplying (2.18) by the thickness t. [14] Another important parameter in describing the scattering from atoms is the atomic-scattering factor $f(\theta)$. This can be found from (2.15) through the following equation

$$|f(\theta)|^2 = \frac{d\sigma}{d\Omega}. \tag{2.19}$$

This parameters importance in describing the intensities for different reflection in a DP will become apparent in section 2.9.

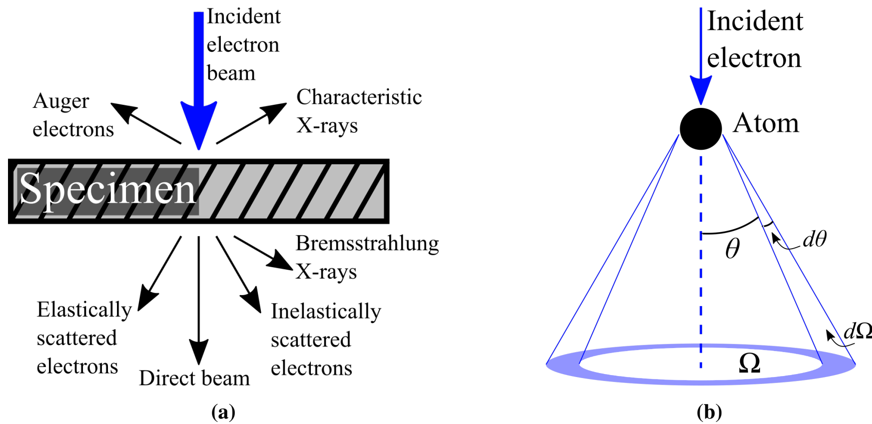

Figure 2.6: (a) As an electron beam hits a sample it excites the atoms and several signals are sent out from the sample which can be used for different purposes. (b) When an electron approaches an atom it can scatter to an angle θ giving a total solid angle of scattering Ω. A small increase in the scattering angle, $d\theta$, gives a small increase in the solid angle of scattering. The figures are adapted from a book by Williams and Carter [14].

2.8 Diffraction

When electrons hit a periodic surface their wave properties result in a diffraction event to take place. This effect can be utilised to study the structure of materials on an atomic scale. When the electrons hit the sample material in the TEM they are scattered to different angles from the atoms in the crystal structure. A distance from the objective lens, equal to the respective focal length, a DP will appear as a result from constructive and destructive interference. This plane, the back focal plane of the objective lens, maps a 2D projection of the reciprocal space of the crystal in its current orientation.

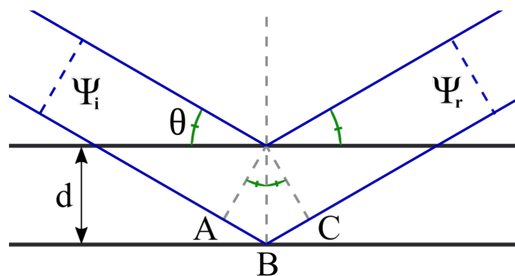

Figure 2.7: An incoming electron beam Ψ_i is reflected from parallel planes with spacing d between them to an outgoing beam Ψ_r. The path difference for beams reflected from the two planes can be expressed as AB+BC. This is depicts the Bragg description of diffraction. The figure is adapted from a book by Williams and Carter [14]

Bragg's Law is a useful concept to describe the constructive interference that needs to happen for a DP to appear. Bragg's Law deals with reflections from planes rather than scattering from atoms. And so it does not truly describe the physical reason for the DP seen in the TEM which is due to diffraction events. But it is a special case of the Laue conditions which do describe the effects in the TEM and mathematically the Bragg description it is correct [14]. Bragg's Law is built upon the assumption that when an incoming electron beam hits the planes of the crystal it is reflected from them as if the planes were semi-transparent mirrors. In Figure 2.7 an incoming plane wave Ψ_i is reflected on two parallel planes to Ψ_r. These "mirrors" reflect some fraction each of the incoming electron beam. The reflected beams from different planes travel different lengths equal to $2d\sin\theta$ where d is the spacing between the planes and θ is the angle between the incoming wave vectors $\mathbf{k}_I$ and the crystal planes. If the angle θ is such that the path difference of the two reflections is equal to an integer number of wavelengths λ, they will constructively interfere. This is expressed by Bragg's Law:

$$2d\sin\theta_B = n\lambda. \tag{2.20}$$

where the angle θ_B is called the Bragg angle and n is an integer [14]. When we are at the Bragg condition we have that the change in wave vector is

$$\Delta\mathbf{k} = \mathbf{k}_I - \mathbf{k}_D = \mathbf{g}, \tag{2.21}$$

where $\mathbf{g}$ is a vector in the reciprocal space of the crystal. The Laue equations can be found by multiplying (2.21) by the crystal axes individually. These equations state that we have constructive interference when

$$\mathbf{a}_1 \cdot \Delta\mathbf{k} = 2\pi h, \tag{2.22a}$$

$$\mathbf{a}_2 \cdot \Delta\mathbf{k} = 2\pi k, \tag{2.22b}$$

$$\mathbf{a}_3 \cdot \Delta\mathbf{k} = 2\pi l. \tag{2.22c}$$

Only when all of these conditions are true simultaneously a diffraction spot will appear. The planes that satisfy this condition can be illustrated using the Ewald sphere. The Ewald sphere is a sphere in the reciprocal space of the crystal with a radii equal to the length of the incoming electrons k-vector. Figure 2.8 presents a 2D representation of the Ewald sphere together with the reciprocal space. At the points where the Ewald sphere intersects with reciprocal points the Bragg condition is satisfied and we get a bright DP spot.

The Bragg condition is only satisfied when the Ewald sphere perfectly intersects with the points in reciprocal space. But this would mean that if we are perfectly aligned on a zone axis, we would have only the central beam appearing in the DP. This is clearly not the case and can be explained by the finite physical size of the crystal. The NWs studied here have a small dimension in the radial direction and so the points in reciprocal space will be extended in the corresponding directions [14]. This includes the direction of the beam as the NWs are studied from the side. As a result the reciprocal points of the NW will not be singular points but lines stretched in the short dimension directions. These lines are commonly called rel-rods [14]. The diffraction condition for the finite crystal is thus described by the Ewald sphere as it intersects the rel-rods. The deviation from the Bragg

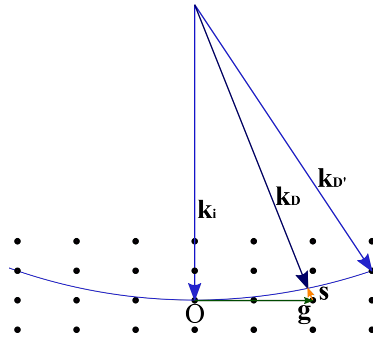

Figure 2.8: A cross section of the Ewald sphere as it overlaps with the reciprocal space of the crystal. The length of the incoming wave vector, $\mathbf{k}_i$, determines the radii of the sphere. The points that overlap with the sphere are at a Bragg angle and contributes to the observed DP. Also points that do not fully satisfy the Bragg condition can appear in the DP if the excitation error $\mathbf{s}$ is not too large. Adapted from [14]

condition is represented by a vector $\mathbf{s}$ called the excitation error. The scattering condition can then be written as

$$\Delta\mathbf{k} = \mathbf{g} + \mathbf{s} \tag{2.23}$$

The Ewald sphere corresponding to the electrons in the TEM with a beam energy of 200kV will result in a sphere with a much larger radii than the one in Fig. 2.8. This means that it essentially cuts out a 2D subspace in the plane perpendicular to the beam direction of the 3D reciprocal space. This plane is called the zeroth-order Laue zone (ZOLZ) and is the DP what we usually see in the TEM. For higher angles the Ewald sphere will curve enough to hit the planes above the ZOLZ called first-order Laue zone (FOLZ), second-order Laue zone (SOLZ) and higher-order Laue zone (HOLZ) [14]. These can be seen for higher camera lengths as this allows higher scattering angles to hit the viewing screen. Once the DP has been recorded it must be indexed to define the orientation of the crystalline material. For this the structure factor is used.

2.9 Structure factor

The structure factor is defined as

$$F_{hkl} = \sum_j f_j e^{-2\pi i(hx_j + ky_j + lz_j)} \tag{2.24}$$

where j runs over the atoms in the unit cell and f_j is the respective atomic form factor [19]. Using these tools the structure factor of the two crystal symmetries present in the studied NWs can be found. If only kinematic theory is considered the intensity of the reflections

in a DP follows $I_{hkl} \propto |F_{hkl}|^2$. Putting the atomic positions for ZB in (2.24) and tidying the expression results in

$$F_{hkl}^{ZB} = \left\{1 + (-1)^{h+k} + (-1)^{h+l} + (-1)^{k+l}\right\}\left[f_a + f_b e^{-i\frac{\pi}{2}(h+k+l)}\right] \tag{2.25}$$

which gives the following extinction rules for the reflections seen in DPs

$$|F^{ZB}|^2 = \begin{cases} 0, & hkl \text{ mixed odd/even} \\ 16(f_a^2 - 2f_af_b + f_b^2), & h+k+l = 4n+2 \\ 16(f_a^2 + f_b^2), & h+k+l = 4n+1 \\ 16(f_a^2 + f_b^2), & h+k+l = 4n+3 \\ 16(f_a^2 + 2f_af_b + f_b^2), & h+k+l = 4n \end{cases} \tag{2.26}$$

Doing the same for the WZ phase using cartesian coordinates gives

$$F_{hkl}^{WZ} = \left\{e^{-i\frac{2\pi}{3}(h+2k)} + e^{-i\frac{2\pi}{3}(2h+k+\frac{3}{2}l)}\right\}\left[f_a + f_b e^{-i2\pi ul}\right]. \tag{2.27}$$

From 2.27 the following extinction rules can be found

$$|F^{WZ}|^2 = \begin{cases} 0, & \text{l odd \& h-k = 3n} \\ 3(f_a^2 \pm \sqrt{2}f_af_b + f_b^2) & \text{l odd \& h-k} \neq \text{3n} \\ 4(f_a^2 + f_b^2) & \text{l = 4m + 2 \& h-k = 3n} \\ (f_a^2 + f_b^2) & \text{l = 4m + 2 \& h-k} \neq \text{3n} \\ 4(f_a \pm f_b)^2 & \text{l = 4m \& h-k = 3n} \\ (f_a \pm f_b)^2 & \text{l = 4m \& h-k} \neq \text{3n.} \end{cases} \tag{2.28}$$

The difference in I_{hkl} for the different spots is not easily seen, or may not even be distinguishable at all, from the DP as dynamical effects will effect the intensity too.

2.10 Diffraction Patterns

By measuring angles and distances for reflections in the DP and comparing with theoretical values, using Eqs. (2.3)-(2.6), the zone axis can be determined and the DP indexed. A model of the $[1\bar{1}0]_{ZB}$ orientation can be seen in Figure 2.9 together with a HRTEM image and a corresponding DP. This is the crystal orientation observed when looking at NWs with ZB phase from one of the hexagonal sides. It is also the orientation used in section 2.2 to describe the stacking sequence of the ZB structure. The next low index zone axis of interest is the $[2\bar{1}\bar{1}]_{ZB}$. This orientation is found by rotating the NW about the crystal growth direction, $[111]_{ZB}$, by 30° relative to the $[1\bar{1}0]_{ZB}$ orientation. A model of this orientation can be seen in Figure 2.10 together with its HRTEM image and DP. For the WZ structure it is the $[2\bar{1}\bar{1}0]_{WZ}$ presented in Figure 2.11 which is seen through the hexagonal sides of the NW. When describing the 2H WZ stacking order in section 2.2 this orientation

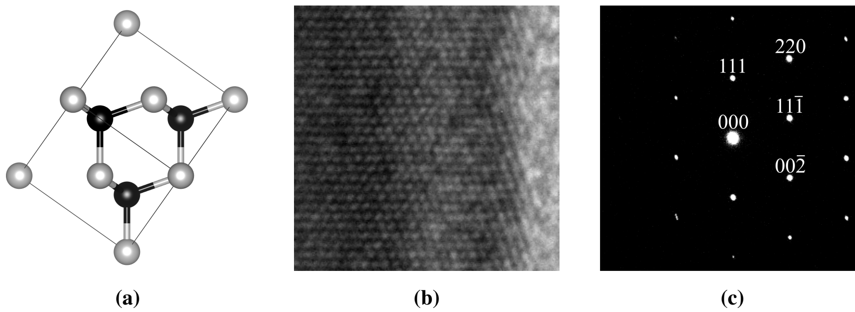

Figure 2.9: ZB seen through the $[1\bar{1}0]$ zone axis for (a) the modelled crystal structure, (b) a HRTEM image of a GaAs NW and (c) the indexed DP for this orientation.

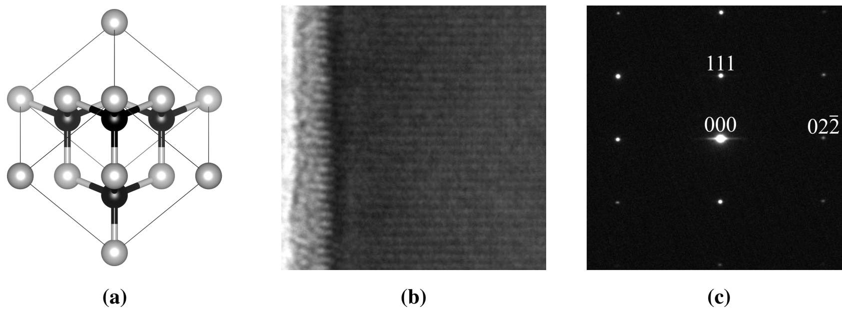

Figure 2.10: ZB seen through the $[2\bar{1}\bar{1}]$ zone axis for (a) the modelled crystal structure, (b) a HRTEM image of a GaAs NW and (c) the indexed DP for this orientation.

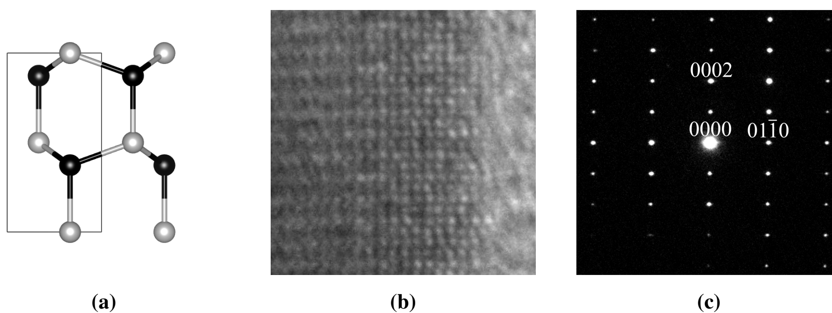

Figure 2.11: WZ seen through the $[2\bar{1}\bar{1}0]$ zone axis for (a) the modelled crystal structure, (b) a HRTEM image of a GaAs NW and (c) the indexed DP for this orientation.

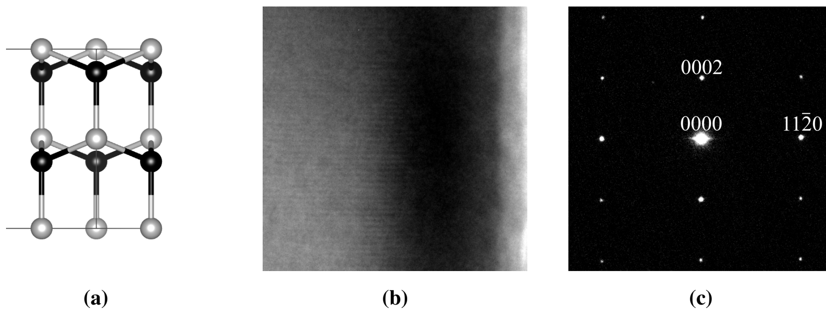

Figure 2.12: WZ seen through the $[1\bar{1}00]$ zone axis for (a) the modelled crystal structure, (b) a HRTEM image of a GaAs NW and (c) the indexed DP for this orientation.

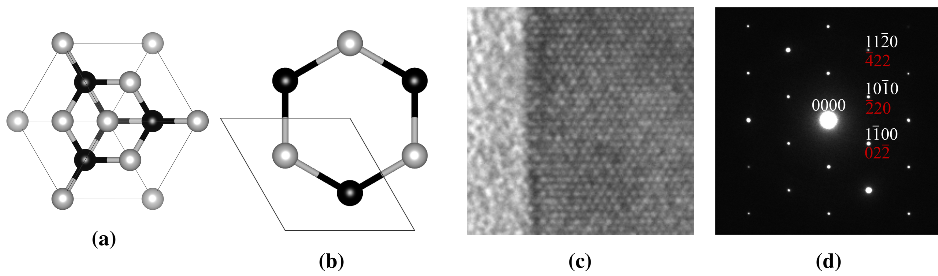

Figure 2.13: (a) Model of ZB at $[111]_{ZB}$ zone axis, (b) model of WZ at $[0001]_{WZ}$ zone axis, (c) HRTEM as observed for both phases (d) the indexed DP for ZB in red and WZ in white. HRTEM and DPs were collected from a cross section of a AlGaAs NW.

was used. Rotating the WZ phase by 30° from the $[2\bar{1}\bar{1}0]_{WZ}$ direction about the $[0001]_{WZ}$, corresponding to the length of the NW, brings the NW to the $[1\bar{1}00]_{WZ}$ direction. This orientation can be seen in Figure 2.12. Looking back at Figures 2.10 of the $[2\bar{1}\bar{1}]_{ZB}$ the two phases can be seen to look the same along these orientations. By making very thin cross-sectional slices of the NWs samples can be made which are transparent to the electron beam through the growth direction $[111]_{ZB}$ and $[0001]_{WZ}$. This case can be seen in Figure 2.13. The reflections labelled with three indexes correspond to the ZB structure and the white WZ.

2.11 Intensity

The intensity of a Bragg diffracted beam in a crystalline material can be described by

$$I = \left(\frac{\pi t}{\xi_{\mathbf{g}}}\right) \cdot \frac{\sin^2(\pi t s_{eff})}{(\pi t s_{eff})^2} \tag{2.29}$$

where t is the sample thickness as experienced by the diffracted beam, $\xi_{\mathbf{g}}$ is the extinction distance and s_{eff} is the effective excitation error [14]. The effective excitation error is related to s as

$$s_{eff} = \sqrt{s^2 + \frac{1}{\xi_{\mathbf{g}}^2}} \tag{2.30}$$

and so it is never zero, for large excitation errors $s_{eff} \approx s$ [14]. Two reasons for intensity fringes in TEM images can be explained by (2.29). From this equation it can be seen that the intensity of a diffracted beam from the specimen is periodic in both t and s_{eff}. The t dependence results in thickness fringes or contours as seen in Figure 2.14a. As the NWs have a hexagonal shape the thickness varies on the edges giving rise to this effect. In Figure 2.14b fringes are present in the axial direction of the NW as a result of bending. The NW has been oriented at a zone axis (in this case $\{2\bar{1}\bar{1}0\}_{WZ}$) where the dark region is very close to the zone in the middle of the image. As the NW bends it is only perfectly on zone in a very small region. On one side it is bent so that the excitation error s is negative. Moving along the NW it bends through the zone to positive s on the other side. For the effective excitation error this would mean that it shifts gradually from a large value to a small and back to large again. From (2.29) it can be seen that this gives a periodic change in intensity called bend contours. It is important to note that fringes could appear for many other reasons as well. One example is strain due to lattice mismatch. This could easily be confused for bend or thickness fringes and so care should be taken when determining the cause for fringes. In Figures 2.14a and 2.14b the NWs consists of pure GaAs. The only changes are in crystal phase. For Figure 2.14b the phase change from WZ to ZB going from the top of the image and down. but this change will not cause the fringes seen in the image. The only reasonable cause for these that the author of this study can see is bending.

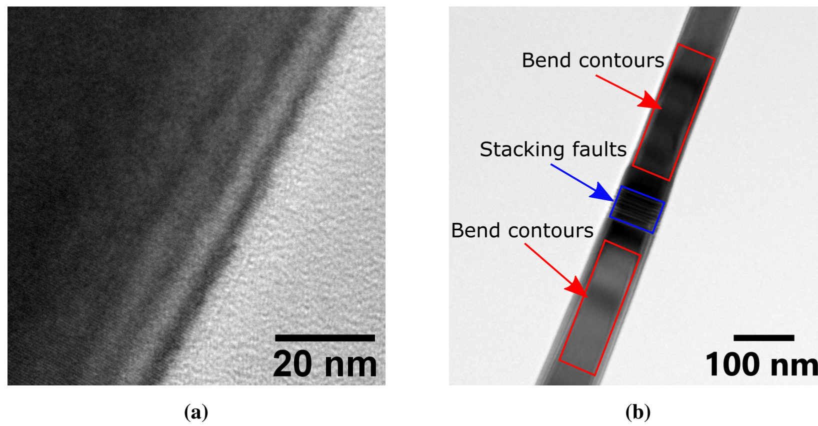

(a) (b)

Figure 2.14: BFTEM images of NWs with presence of (a) thickness fringes on the edge of hexagonal shaped NW and (b) bend contours (marked in red boxes) along the NW due to atomic planes bending through the diffraction condition.

2.12 TEM mechanics

The TEM is schematically built as presented in Figure 2.15. It can be divided into three main sections; the condenser system, the objective system and lastly the intermediate and projector lens system. The TEM combine aperture (AP)s, lenses, deflectors and stigmators to manipulate the electron beam. The APs are simply small holes in a thin plate which can be used to block unwanted electrons from going further. These can be used for several reasons from increasing the collimation of the beam to selecting electrons diffracted to a specific angle in the DP. The lenses are coils in which a current is applied to form a magnetic field. The electromagnetic lenses work in a similar fashion to glass lenses, but in a glass lens systems the focusing power of the lens is constant and the lenses are physically

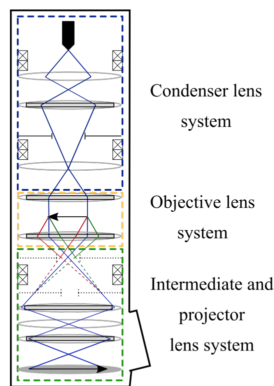

Figure 2.15: A schematic overview of the TEM machine. The figure is adapted from [14]

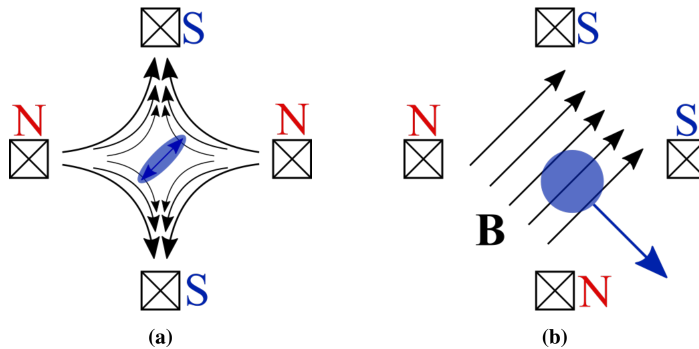

Figure 2.16: Figures of a quadrapole setup as (a) a stigmator and (b) a beam deflector. Figures adapted from [14]

moved to change the bending of the beam. For the electromagnetic lenses the strength is changed by increasing or decreasing the current through the coils and the position is constant. The effect of the lenses on the electrons is described by the Lorentz force on charged particles q moving in a magnetic field $\mathbf{B}$

$$\mathbf{F} = q(\mathbf{E} + \mathbf{v} \times \mathbf{B}). \tag{2.31}$$

Here $\mathbf{v}$ is the velocity of the electron through the field. In the lenses the electric field $\mathbf{E}$ is zero. As the electrons never move exactly parallel to the magnetic field in the lenses the magnetic force on the electrons cause them to move through the lens in spirals. This rotates the image seen on the viewing screen relative to the physical position. Another lens with a strength appropriate to rotate the image back to the ”original” position can be used to correct for this effect.

The electromagnetic lenses are far from perfect and introduce aberration effects and astigmatism to the beam. The aberration effects can be reduced with advanced systems but this is the limiting factor on the resolution one can achieve in the TEM. The quality of the lens is best close to the optical axis and so the measurements done in the TEM are usually done as close to this as possible. The astigmatism can be introduced as a result of the magnetic field not being perfectly uniform as the electrons move through the lenses and from contamination on the APs. This causes the cross-section of the beam to become elliptical rather than circular. Using a quadrapole lens setups as seen in Figure 2.16a the astigmatism can be adjusted. This creates a magnetic field that ”stretches” the cross-section of the beam counteracting the astigmatism. If the condenser AP is misaligned astigmatism will also occur. The correct way to fix this would then be to align the AP. The quadrapole setup can also be used as in Figure 2.16b. In this configuration it is called a deflector. By placing two deflectors successively in the beam path the beam can be shifted and tilted as seen in Figure 2.17.

At the very top of the TEM there is an electron gun and a beam accelerator that produce the electron beam for illumination of the sample. The electron beam can typically have an energy of a few tens of keV to a few hundred keV. The electron source used can be

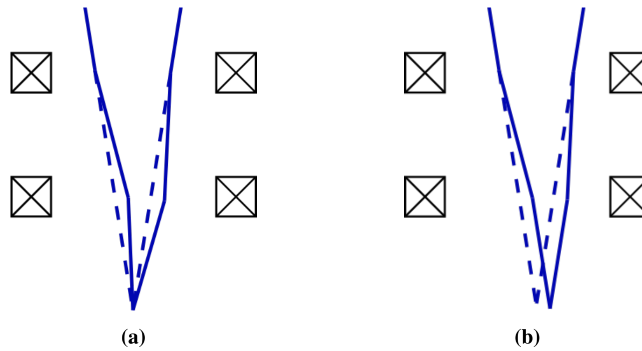

Figure 2.17: Figures of (a) beam shift and (b) beam tilt. Figures adapted from [14]

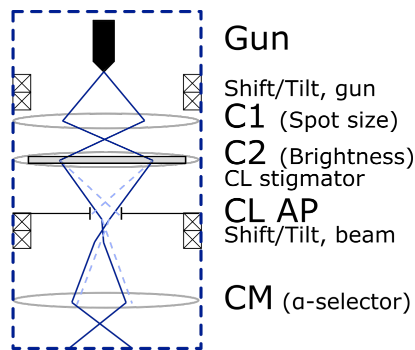

Figure 2.18: Ray diagram of the condenser lens system. Figure adapted from [14]

either a thermoionic device or a field-emission source, commonly called a field-emission gun (FEG). the thermoionic source is typically made of LaB_6 and the FEG is typically made of a tungsten needle. The FEG gives a more monochromatic beam which can be of interest in several measurements like HRTEM imaging. On the other hand the FEGs small size makes it less able to sufficiently illuminate large areas for quick overview images. Going back to the beam path in the TEM, as it exits the gun it passes a deflector that control the gun tilt and gun shift. Putting together the parts explained above, the three main sections of the TEM can be described starting with the condenser system.

2.12.1 The condenser lens system

The purpose of the condenser lens system is to control the beam illuminating the sample. A ray diagram of this system is displayed in Figure 2.18. In normal TEM mode the condenser lenses are used to make the beam parallel as it hits the sample. This is controlled using the C1 and C2 lens. The C2 control the brightness of the beam. This is used to adjust the convergence angle α of the beam as it hits the sample. Ideally the beam should be

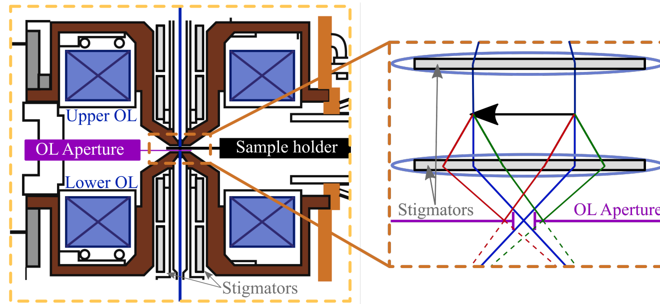

Figure 2.19: Split polepiece objective lens system and a focused schematic view on the diffraction events in the sample. The figure is adapted from [14]

perfectly parallel but this would make the intensity of the image on the viewing screen too low, and so the C2 lens is adjusted so that the beam converges enough to barely fill the viewing screen. The angle α required for this is small enough that the beam can still be considered as parallel.

This section also has a condenser lens AP which increase the collimation of the electron beam by stopping electrons passing at a too high angle relative to the optical axis. The smaller this AP is the more parallel the beam hitting the sample will be, but at the cost of lower intensity. To control the position of the beam by shifting it before it hits the sample, deflectors are present in this part of the system as well in addition to the one after the electron gun. These can also be used to tilt the beam to change the angle at which the beam hits the sample which is useful for DF imaging. There is also a condenser lens stigmator present to correct for any astigmatism introduced by the condenser lenses and AP.

2.12.2 The objective lens system

This next section of the TEM is perhaps the most important part of the microscope. The objective system consists of an objective lens, the sample in its holder and the objective AP. For the TEM apperature used in this study a split polepiece objective lens is used. This can be seen in Figure 2.19 In the middle of the pole-pieces the sample is placed in a sample holder. The sample holder has a flat surface with a hole in it where a TEM grid can be placed. In this study the sample can be moved in the xy-plane perpendicular to the beam and tilted around the x- and y-axis. The maximum tilt angle is 35°.

The objective lens is the most powerful lens in the TEM and it limits the resolution of the TEM [25]. It is this lens that give us the image and diffraction plane we look at in the viewing screen. Both the sample and the objective AP is placed between the polepieces. The objective AP is placed in the back focal plane of the objective lens and is used to select which scattering angles are to contribute to the final image.

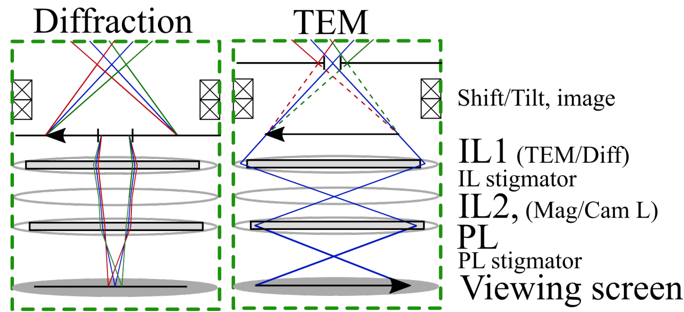

Figure 2.20: Left: Ray diagram for TEM in selective area diffraction mode. Right: Ray diagram for TEM in imaging mode.

2.12.3 The intermediate and projector lens system

The objective lens makes the diffraction and image plane and the intermediate lens that focuses one or the other to the viewing screen. Figure 2.20 shows a ray diagram for this part in both diffraction and image mode. Both the objective lens and the projector lens have a fixed strength. The intermediate lens is adjusted so that we get something we can interpret on the viewing screen. In this section there is also an AP placed in the image plane of the objective lens as seen in Figure 2.20. This AP is used in selective area electron diffraction (SAED) where it is used to select what part of the material should contribute to a diffraction pattern when the TEM is put in diffraction mode.

Finally, at the bottom of the machine there is an imaging system for recording the data obtained in the TEM. This is done with a charge-coupled device (CCD) camera placed below the projector lens. When the electrons hit the CCD some charge is created in the sensor and stored. The CCD consists of a grid of sensors with a typical resolution of $4k \times 4k$ for TEM measurements. The charges in this grid is most commonly shifted out serially and stored as a digital signal.

2.13 Bright-Field and Dark-Field

The image seen in the normal imaging mode of the TEM, with no objective AP inserted, is a result of the sum of all the electrons scattered through the sample. If a large objective AP is inserted the contrast can be increased as highly scattered electrons are filtered from the image. By decreasing the size of the AP further more scattering angles will be removed and if the AP is chosen so small that only the central beam is allowed to pass the TEM is in BF imaging mode. The intensity in the BF image consists of electrons that have not been scattered, or only very weakly, through the sample. Regions where the electrons pass through vacuum, or little to no scattering effect on the electrons path, appear bright in the image hence the name BF.

In DF imaging on the other hand most of the diffracted electrons are filtered out and the image is built from the electrons scattered from specific plane(s). This can be done by placing the objective AP to only allow one or a few DP spots to pass through it. To get the best result the DP spot(s) used should be on the optical axis of the microscope. This is achieved by using the deflectors in the condenser system of the TEM to tilt the incoming electron beam on the sample. This effectively moves the DP in the focal plane so that the desired diffraction spot is in the centre of the optical axis. The resulting image is what is called a DF image. Only regions of the NW with planes that scatter electrons to the chosen DP spot(s) will now show intensity in the image. This makes it a great way of distinguishing regions with different crystal structures and/or orientations.

In Figure 2.21 the DF images of a GaAs NW from three different DP spots can be seen. The DP is from a region of the NW where there is ZB structure and twinning present. The first image uses a $(111)_{ZB}$ spot present in both orientations. And so in Figure 2.21a all the ZB parts of the NW can be seen. In 2.21b only one of the ZB orientations can be seen. And in 2.21c only the corresponding twin orientation contributes to the intensity.

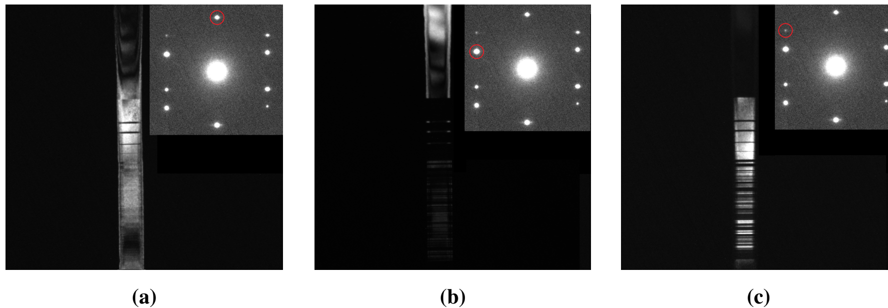

Figure 2.21: DF TEM images from a GaAs NW using (a) $(111)_{ZB}$ reflection present in both ZB orientations, (b) $(\bar{1}\bar{1}1)_{ZB}$ reflection only present in one ZB orientation and (c) t$(002)_{ZB}$ spot of the ZB twin regions

2.14 Kikuchi lines

Before any HRTEM images or DPs can be collected the sample will have to be oriented to the correct zone axis. This is done by using Kikuchi lines as illustrated in Figure 2.22. To obtain these images the beam is focused to a spot on the sample and the TEM is put in diffraction mode. As the beam hits the sample the electrons are scattered on the crystal to all directions within the sample but with higher intensity in the forward direction. The electrons that hit the plane at Bragg's angle will be Bragg diffracted. As the planes are illuminated from all angles the Bragg condition will be fulfilled for incoming electrons travelling along the sides of a cone with angle θ_B relative to the plane. These cones are called Kossel cones and on the viewing screen they are seen as parabolas called Kikuchi

lines. This process happens to all the planes in the crystal and the result is a Kikuchi map made by the overlapping Kikuchi lines. If the sample is too thin, or the beam is perfectly parallel as it hits the sample, the scattered electrons will be dominant in the forward direction and the Kikuchi pattern will not be obtained. By focusing the beam on the sample the electron flux from directions not parallel to the optic axis increases and the Kikuchi lines becomes visible.

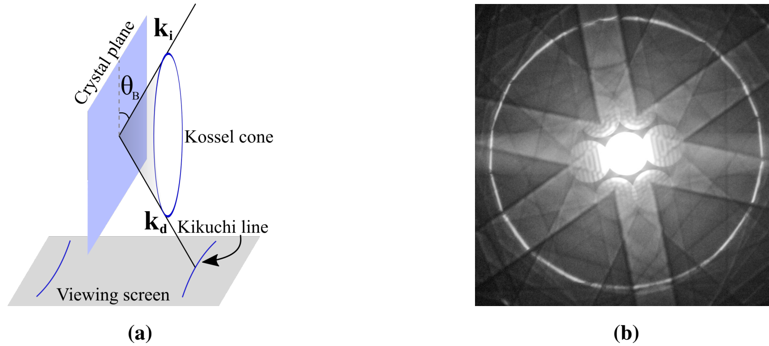

Figure 2.22: (a) Electrons hitting crystal plane with braggs angle θ_B creates Kossel cones. Where the Kossel cones intersect with the viewing screen parabolas are seen. Figure is adapted from [14] (b) Image taken in the TEM of a Kikuchi pattern from GaAs aligned on the $[1\bar{1}0]$ zone axis. The small angles θ_B make the parabolas look like lines on the viewing screen.

2.15 Scanning Precession Electron Diffraction

SPED is a STEM technique where the electron beam in the TEM is focused to a small point on the sample with a convergence angle $\alpha > 0$ and is precessed around the optic axis [26] with a typical precession angle $\phi \in (0, 1)°$. The angle ϕ tilts the Ewald sphere in reciprocal space so that it cuts out a circle with an angular radii of 2ϕ in the ZOLZ as illustrated in Figure 2.23a. When the beam is then precessed at this angle the circle is rotated about the optical axis which excites more scattering angles. STEM techniques can achieve a spatial resolution of ~ 1 nm, making it possible to probe very small parts of the samples for various properties with high resolution [17]. The precession in SPED degrades the spatial resolution somewhat depending on the sample thickness. But in return it excites more reflections, giving a higher field of view in the reciprocal space as illustrated in Figure 2.23b. Another advantage with the precession is that it makes the DP more like the kinematically explained DP as it effectively averages out dynamical effects [26]. The dynamic scattering is very dependent on the incoming beam direction and some dynamical scattering events present at one angle will disappear as the beam precesses and hits the sample from a different direction [14]. The precessed probe is used to scan the area of interest in the crystal space creating a four-dimensional data set of DPs. In post-processing these stacks of DPs can be used to simulate many of the functions of the TEM.

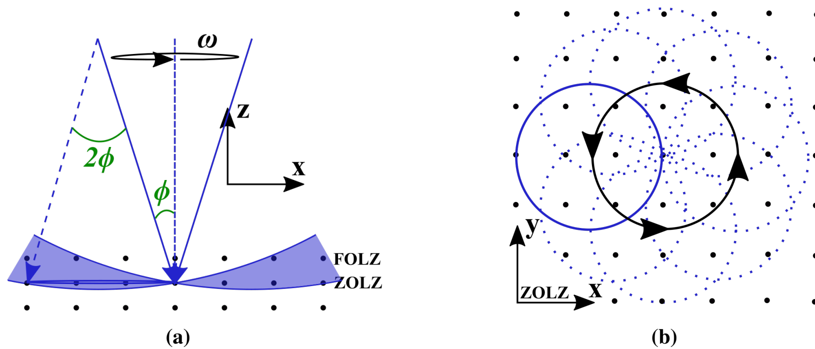

Figure 2.23: (a) The Ewald sphere intercepts the ZOLZ in a circle when the beam is titled by an angle ϕ. As the beam precess it the scattering condition is fulfilled for all points in side the opaque blue areas. (b) The field of view is then increased in the ZOLZ as illustrated with the dotted circles representing the intersection between the Ewald sphere and the ZOLZ as the beam is precessed.

2.15.1 Virtual imaging

When studying crystals in the TEM it is useful to use BF and DF imaging to clearly separate different phases and orientations as explained in section 2.13. For SPED measurements the same thing can be done with virtual bright-field (VBF) and virtual dark-field (VDF). This is done by creating an image of the scanned points where only scan points with a specific chosen reflection present in the associated DP will have intensity in the virtual image. The NWs studied in this thesis have a known phase and are oriented very close to the $[1\bar{1}0]_{ZB}/[2\bar{1}\bar{1}0]_{WZ}$ when initially put into the TEM. This makes it easy to characterise and separate the phases present in the NWs from well known zone axis.

2.15.2 Template matching

In general samples are more randomly oriented and may have crystal structures that are less obviously different which makes the virtual imaging less useful for determining the phase and orientation. In these circumstances a more rigorous approach called template matching is of more use. This is a process where a DP is simulated from a given structure. This is done for several orientations of the crystal depending on a given resolution. The simulated DPs are then compared to the observed DP in the SPED data to determine the corresponding phase and orientation. From the complete data set a phase map and orientation map can be obtained. This method can be efficient for characterising a material, but as the DPs must be simulated and compared for each scan point, the process can be quite computationally demanding for larger data sets. Some knowledge about the material must also be known in advance in order to simulate possible DPs which will be used for phase and orientation determination. Once the simulated DPs are obtained they are compared to the observed DP to find the best match.

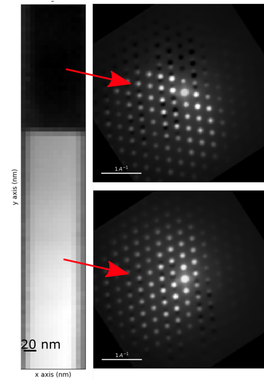

Figure 2.24: NMF results from SPED scan of a NW with a twin plane present. The two elements found by the NMF algorithm corresponds in this case to the DPs of the two different ZB orientations.

2.15.3 Non-negative Matrix Factorisation

Machine learning routines can be used to great effect for analyzing large amounts of data with minimum user input. In crystollography machine learning can be used to gain useful information of the observed structures. An example of this is non-negative matrix factorization (NMF). This is a linear factorization which divides the data into a desired number of components and their weighted position in the data set [27]. This is done through finding an approximate factorization for a matrix V of measurements as

$$V = WH, \tag{2.32}$$

where the elements of W describe the components of the data set and H gives the weight of each component. Both of the factorization matrices are required by the algorithm to have positive elements, hence the name NMF. This results in the different components being combined additively rather than finding differences. In many applications this can make it more intuitively understandable [28]. Figure 2.24 is an example of an image obtained from NMF where the algorithm has separated between two different orientations of ZB when analyzing a ZB twin. NMF results should be interpreted with care as they are merely components determined by the algorithm and does not necessarily have any real interpretation.

2.15.4 Strain measurements

The strain in NWs can be also be analysed using SPED measurements. The distances between reflections in the DPs of the studied material will be inversely proportional to the strain. Careful measurement of the distance to reflections in the DPs gives a value for the corresponding lattice spacing in the crystal. Comparing this distance to the corresponding distance from a DP of a reference region of unstrained material gives a value for the change

in lattice spacing, or strain, in that region. Doing these measurements for each DP in a SPED scan gives a map of the strain in the NW. It is done by selecting two reflections of interest and measuring the distance in every DP and mapping the result out in a plot. These maps can present the strain in the horizontal direction, vertical direction, shear stress and local rotation of the crystal structure.

2.16 EDS

When electrons with a high kinetic energy interact with a material two types of X-ray emission is created. One is bremsstrahlung as a result of charged particles experiencing an acceleration. The other is called characteristic X-rays and this is used in EDS. When the electrons hit the atoms in the material they can excite electrons from core orbital. This creates a vacancy in that orbital. An electron from a higher orbital can then de-excite to lower the total energy state of the atom and bring it closer to its ground state again. This process is accompanied by the release of a photon. This photon will have an energy equal to the energy difference of the two orbitals. The resulting X-ray has an energy characteristic of the atom it came from. By measuring these X-rays it is then possible to determine the composition of a material. Another possible event when the higher orbital electron de-excites is the release of an Auger electron in place of the characteristic X-ray. This effect is not of interest for the EDS measurements [14].

To measure the energy of the X-rays a detector is placed in the objective system as close to the sample as possible. The X-ray signal from the elements quickly dissipates as the radiation is travelling from the sample as a spherical wave and so the closer the detector is the better. But there are limits to how close the detector can be placed to the sample as the split-polepiece system in the TEM leaves little free space around the sample(see Fig. 2.19). When the detector senses an X-ray it shuts the detector from further incoming radiation while the energy of the X-ray is measured. Once this is done it will open up again and count a new one. This is done over a time interval of adequate length to get reasonably good statistics. The general composition of a larger area can be found as a whole or a more localised view of the composition can be found by focusing the beam to a small spot and raster-scan the material surface [14].

The detector used for this measurement is usually a silicon-drift detector (SDD). When X-rays hit the semiconductors, electron-hole pairs are generated. The characteristic X-ray energies are typically higher than 1keV and the energy required to excite an electron-hole pair in Si is about 3.8eV. This means that a lot of hole pairs can be generated when an X-ray is absorbed. The current generated as a result from the absorbed X-ray is used to calculate the X-ray energy. To avoid miscalculations, by summing two different X-rays, the detector blocks all incoming X-rays after one has been detected. The amount of time that the detector is closed is called dead-time and is measured in percentage of the total operational time. In order to reduce the summation of X-rays the dead-time should be kept low. This means the X-ray flux on the detector is low and summation is less likely

to happen. Another effect that can occur is escape peaks. These are typically a result of the incoming X-ray exciting Si atoms which de-excites by sending out a photon of energy equal to its K_α X-ray of 1.74keV. This results in an X-ray photon of energy $E - 1.74$keV being measured [14].

Chapter 3

Experimental

3.1 Material growth and specimen preparation

The studied NWs are made of GaAs with axially inserted heterostructures of GaAsSb. These were grown using the VLS method described in section 2.3 using an MBE system and Ga as the calatyst droplet. For this growth a substrate of p-Si(111) was used. The TEM samples are prepared by scraping the NWs from the substrate that they have been grown on with a small diamond scraper. A TEM grid made of copper, with a $\sim$ 20 nm thin carbon film on it, is then humidified with isopropyl alcohol or ethanol and wiped over the scraped area. The loose NWs then stick to the grid and are ready for observation in the TEM. In order to be able to study the same NW several times numbered TEM grids were used as presented in Figure 3.1. The NWs hexagonal shape cause them to have a very similar initial axial orientation on the TEM grid. When the NWs are scraped off the substrate and placed on the TEM grid the most stable position is to lie on one of the hexagonal facets.

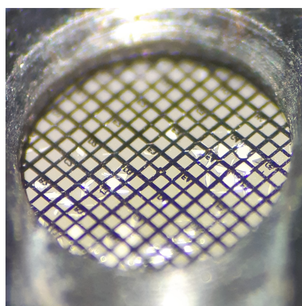

Figure 3.1: A numbered copper TEM grid with a thin carbon film placed in the goniometer of the TEM.

3.2 TEM

In this study two TEM machines from JEOL has been used, a Jeol Jem 2100 and a Jeol Jem 2100F. Both were operated with a beam energy of 200 kV and use Gatan Digital Micrograph acquisition software.The 2100 has a LaB_6 thermoionic electron source. It uses a 2k Gatan Orius CCD camera for collecting images which is placed above the viewing screen. The JEOL JEM 2100F is very similar to the 2100 but it has a tungsten FEG electron source. It uses a 2k Gatan Ultrascan CCD camera placed under the viewing screen. Processing of the images obtained from these TEM machines were performed using ImageJ.

3.3 Scanning Precession Electron Diffraction

The SPED measurements presented in this thesis have been acquired on the JEOL JEM 2100F (See section 3.2). The SPED system is provided by NanoMEGAS and uses their ASTAR acquisiton software. This system controls the precession of the beam and the descan done after the electron beam has passed through the sample. The descan is important and must be adjusted when setting up the machine for SPED measurements. The measurements taken in this study has been done using a precession angle of $0.7°$ in the ASTAR software. From calibrations taken, the true value of the precession angle was found to be $0.62°$ (See Appendix D). The SPED data is collected using a Stingray optical camera with a resolution of 144 by 144 pixels. This camera is mounted outside the viewing window of the TEM and takes an image of the DPs seen on the fluorescent viewing screen.

In post-processing routines for phase mapping, libraries of simulated DPs are created for each phase which are then used to determine the observed phase and orientation. These libraries have been created from simulated models of the ZB and WZ structure in .cif format. A rotational resolution of $1°$ has been used and an angular range of $180°$.

3.4 EDS

The detector used to record EDS data is an Oxford X-Max 80 SDD provided by Oxford Instruments. A map from raster scanning the sample can be created to give a detailed look of the material composition. The EDS data presented in this thesis were collected by Professor Antonius T.J. van Helvoort. It was performed in STEM mode and with a scanning step size of 1 nm has been used and X-Rays with energies between $1 - 20$ keV were collected. The acquisition is controlled by a software from AZtecEnergy and the energy dispersive X-ray spectroscopy (EDX) data analysis is performed using HyperSpy (see Appendix O).

3.5 Simulations and data processing

The models of the crystal structures presented in the theoretical section has been created using the VESTA software [29]. SPED measurements in this study have been analysed in post-processing procedures using the python coding language with the open-source library pyXem v0.11.0 created for the study of crystallographic diffraction microscopy [18]. Simulations of diffraction patterns for use in template matching has been done within the pyXem environment. To perform these measurements a crystallographic information file (CIF) for the crystal structures for this purpose were created using the ReciPro software package [30].

Chapter 4

Results

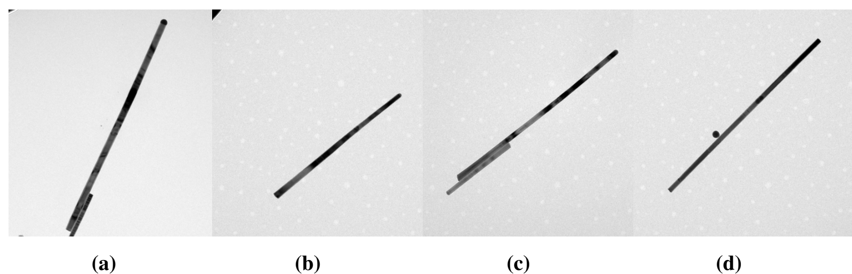

(a) (b) (c) (d)

Figure 4.1: Some NWs considered for closer study having a typical morphology. These are all aligned to the y-axis of the TEM making them relevant for closer study requiring specimen tilting.

The studied NWs grow with varying degrees of defect densities and stacking fault (SF)s. Some examples of the typically observed NWs from initial TEM imaging can be seen in Figure 4.1. They have a width of about $80 - 130$ nm and lengths around $3 - 4$ μm. In Figures 4.1a and 4.1c the NWs can be seen to touch a neighbouring NW which could be a problem if it happens at an area of interest. In Figures 4.1b and 4.1d no droplet is present at the top of the NW. In Figure 4.1d the catalyst Ga droplet can be seen next to the NW. The goal of this work has been to characterise all aspects of the NWs relevant for their properties. This includes the crystal phases, defects like twinning and SFs, composition and strain due to a change in composition. Different acquisition parameters for the strain measurements will also be studied to find the most reliable method. The work has been done using both conventional TEM and SPED measurements. The NW presented in Figure 4.1a, representing the typically observed NW, was chosen for these closer studies. For this NW the catalyst droplet is still on top, stacking faults and twin planes are present, an inserted heterostructure is present and it has a typical length and shape observed for the NWs. The length is about 4 μm and it has a diameter of about 133 nm when oriented at the $[1\bar{1}0]_{ZB}$ zone axis. NW-to-NW variations will not be studied further in this work.

This chapter will start with presenting the crystal structure and observed defects. Next the orientation of the phases and bending present in the NW will be presented. A composition EDS map for the NW where the GaAsSb heterostructure is placed will then be given and lastly the strain introduced as a result of this inserted heterostructure will be given for different values of electron beam convergence angles α and camera lengths.

4.1 Crystal structure

For initial studies of the crystal structure the NW was oriented at the $[1\bar{1}0]_{ZB}$ and $[2\bar{1}\bar{1}0]_{WZ}$ zone axis. The reason for this is that in this orientation the different stacking sequences of the two phases, and of twinned ZB, are distinguishable as presented in section 2.10. Also for BF TEM images this can be seen, in Figure 4.2a a change in stacking inside the blue square results in a sharp change in contrast for the $[1\bar{1}0]_{ZB}$. If the NW is rotated 30° about the $[111]_{ZB}$ direction, to the $[2\bar{1}\bar{1}]_{ZB}$ zone, this is no longer there.

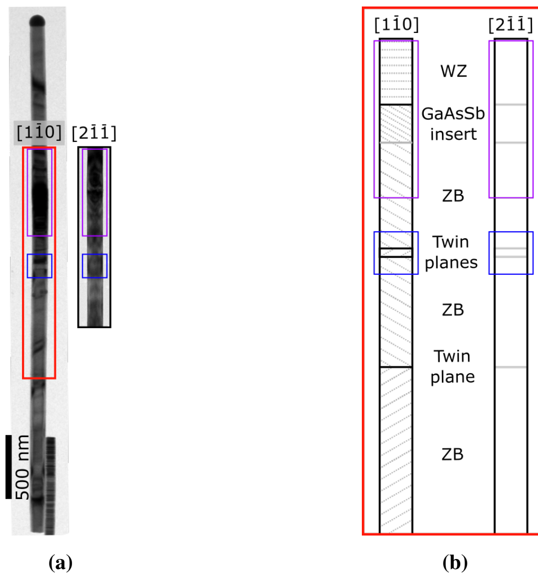

(a) (b)

Figure 4.2: (a) BF images of the more closely studied NW oriented at $[1\bar{1}0]$ (full length) and $[2\bar{1}\bar{1}]$ as marked in the figure. (b) A schematic of the main area of interest (red squares) for $[1\bar{1}0]$ and $[2\bar{1}\bar{1}]$ orientations. The grey dotted lines represent the phases of the different regions, angled for ZB and vertical for WZ.

Going forward mainly three sections of this NW, marked by squares in Figure 4.2a, have been studied and will be presented. The red square marks the main region of interest where both the insert is found and twin planes for the ZB phase. This area will in the continuing be referred to as the main area. The purple square marks the insert region and will be referred to as the insert area. Below the insert area a blue square covers a small region where two closely spaced twin planes are found, this will be referred to as the twin area. In Figure 4.2b a schematic map for the main area is presented in the two orientations of interest. The dotted lines represent the different stacking sequences seen at the $[1\bar{1}0]_{ZB}$ orientation. The angled lines represent the ZB phase and the horizontal WZ. A schematic for the crystal structure as seen through the $[2\bar{1}\bar{1}]_{ZB}$ zone axis is also given to emphasise the fact that there is no discernible difference in the stacking sequence in this orientation.

DF images at low magnification of the upper part of the NW using the $11\bar{1}_{ZB}$ reflection of the ZB phase is given in Figure 4.3a. A varying contrast along the NW is present due to dynamical effects. But a sharp transition can still be seen at the top where the stacking changes. A dark region inside the ZB phase towards the bottom of the image is seen. This can be found to be a twinned ZB region from a DF image using the $00\bar{2}_{ZB}$ reflection as shown in the green squares in Figure 4.3a. By placing the aperture around the $01\bar{1}0_{WZ}$ reflection of WZ, the image seen in Figure 4.3b is obtained. Again a lot of dynamical effects are present, altering the intensity, but a sharp transition can be seen towards the bottom marking the point of the phase change. In this image SFs towards the top of the NW is visible as well. In Figure 4.4 a HRTEM image of the stacking faults is given.

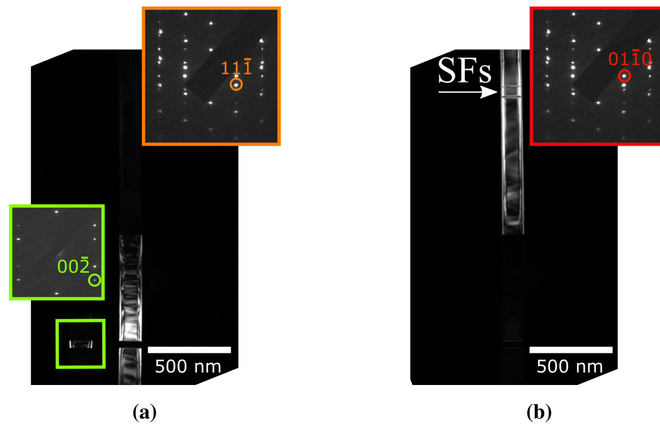

Figure 4.3: DF images of (a) ZB region using the $11\bar{1}_{ZB}$ reflection as marked in the red square together with a DF of the twin region using the $00\bar{2}_{twin}$ reflection seen in the orange squares and (b) WZ region using the $01\bar{1}0_{WZ}$ reflection marked in the red square.

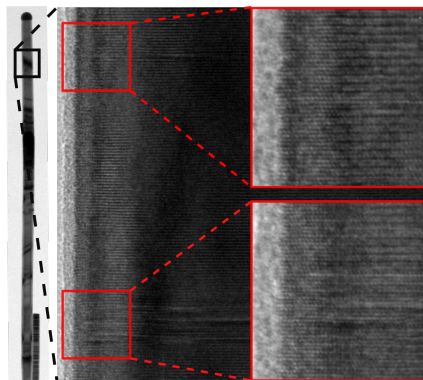

Figure 4.4: HRTEM of the SFs found in the upper part of the studied NW as marked in the model on the left side. NW is oriented at the $[2\bar{1}\bar{1}0]$ zone axis.

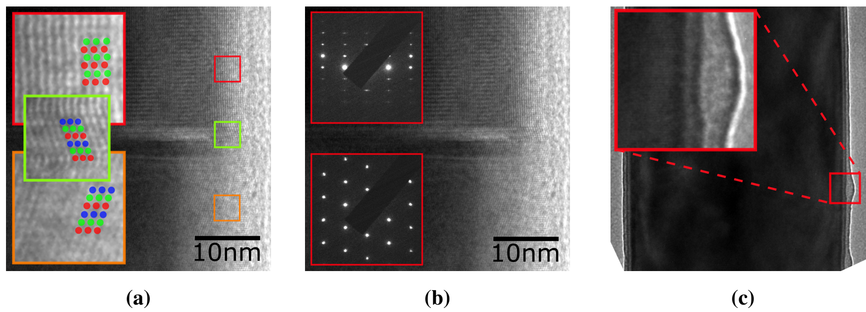

Figure 4.5: (a) HRTEM image of insert region with NW oriented at $[1\bar{1}0]$ and $[2\bar{1}\bar{1}0]$. The top has AB WZ stacking and bottom has ABC ZB stacking. The different stacking layers have been illustrated by red circles for the A layer, green for the B layer and blue for the C layer. Green square marks a twinned ZB section. (b) DPs for the two phases from (a). (c) A HRTEM image of the insert area when aligned at the $[2\bar{1}\bar{1}]$ and $[1\bar{1}00]$ zone axis.

HRTEM images have also been collected to study the point of phase change as seen in Figure 4.5a. In this image the stacking sequence of the two phases can be observed to be the AB stacking of WZ at the top and the ABC stacking of ZB at the bottom. A twinned ZB region is observed to be present at the phase change marked by the green square. The extent of the twinned section is found to be about 6 d_{111} stacking layers, or a little less than 2 nm. DPs collected for the two regions can be seen in Figure 4.5b. A similar symmetry would be observed when taking an fast Fourier transform (FFT) from a section of each phase in the HRTEM images (see Appendix G) and so can be used as an extra tool to distinguish the two phases. A HRTEM image was also taken of the insert area with the NW aligned at the $[2\bar{1}\bar{1}]_{ZB}$ and $[1\bar{1}00]_{WZ}$ zone axis as presented in Figure 4.5c. In this orientation the exact position of the phase change cannot be found as the two structures look the same. But some *bumps* can be seen on the side of the NW which seem to be roughly at the phase change. The zoomed in view makes it possible to discern the stacking in this orientation which is much more dense as also seen before in section 2.10.

Moving on, SPED measurements were taken for the areas described in Figure 4.2a which can be used to distinguish the different phases as well. As explained in section 2.15 this method collects a stack of DPs pertaining to a specific spot on the NW, by scanning across it with a small electron beam probe. Images of the observed DPs from this technique with and without precession has been collected with the CCD camera in the TEM to illustrate the effect of the precession. This can be seen in Figure 4.7 for two different convergence angles α. For the precessed DPs in Figures 4.7b and 4.7d, the field of view in reciprocal space can be seen to increase and dynamical effects are suppressed. This affects the VDF images obtained from the SPED data. In Figure 4.6a a VBF image of the insert area oriented at the $[2\bar{1}\bar{1}]$ and $[01\bar{1}0]$ is presented. This region was scanned using SPED procedures both with precession of the electron beam and without precession. In Figure 4.6b VDF images created from the region in the black square in Figure 4.6a can be seen. In the red squares the beam has been precessed and in the orange squares it has not. In the collected DPs without precession a lot of dynamical effects altering the reflection intensi-

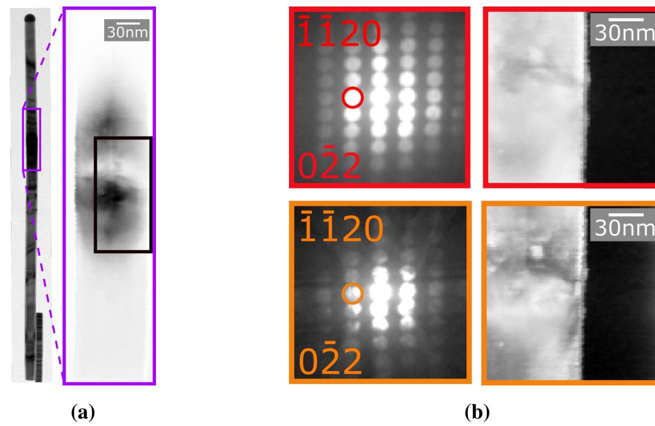

(a) (b)

Figure 4.6: (a) VBF image of the insert area oriented at the $[2\bar{1}\bar{1}]_{ZB}$ and $[1\bar{1}00]_{WZ}$ orientation. (b) DPs and VDF images from the region marked by a black box in (a). The images in red boxes are precessed and the orange boxes are not. The used reflections are labelled in the DPs for both the ZB and WZ phase in the DPs.

ties can be seen. Also weak Kikuchi lines, as explained in section 2.14, can be discerned in the DP. The VDF image created from the data set without precession have a more varying contrast than the precessed VDF in red boxes.

To separate the phases with SPED a large scan for the main area was done with the NW oriented at the $[1\bar{1}0]_{ZB}$ and $[2\bar{1}\bar{1}0]_{WZ}$ zone axis using a step size of $\sim$ 8.3 nm so as to be able to cover the larger area with a reasonable collection time for the data. VDF images created from this data to separate the phases can be seen in Figure 4.8a. This gives a clear view of the different phases along the NW. From the DPs seen in Figure 4.8a the NW can be seen to bend considerably along the length leaving the top and bottom of the scanned region to be quite far off zone. But as the reflections close to the central beam are present for most areas of the scan this is not a serious problem for the VDF procedure

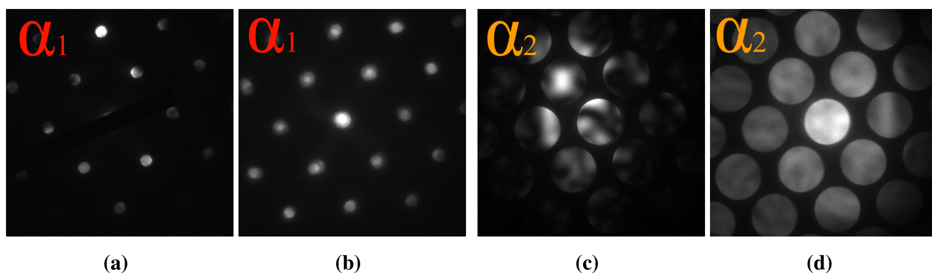

(a) (b) (c) (d)

Figure 4.7: DPs obtained from ZB oriented at $[1\bar{1}0]_{ZB}$ with (a) no precession and convergence angle $\alpha_1 \approx 1.3$ mrad, (b) with precession for same convergence angle as in (a), (c) no precession and convergence angle $\alpha_2 \approx 3.5$ mrad and (d) with precession for the same convergence angle as in (c).

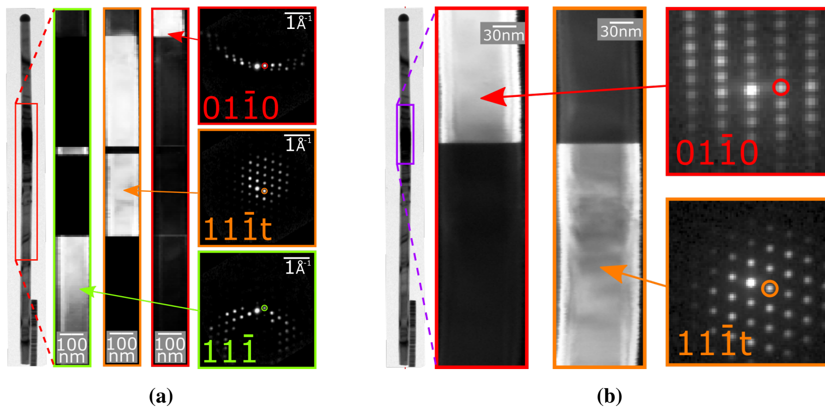

(a) **(b)**

Figure 4.8: (a) VDF images for a large scan of the main area oriented at $[1\bar{1}0]_{ZB}$ and $[2\bar{1}\bar{1}0]_{WZ}$ covering the insert at the top and the lower twin planes with DPs for the different regions along the NW. (b) VDF images for the insert area oriented at $[1\bar{1}0]_{ZB}$ and $[2\bar{1}\bar{1}0]_{WZ}$. The used reflections for each VDF image are marked in their respective DPs.

when choosing appropriate reflections. Keeping the NW orientation the same, decreasing the scan step size to $\sim$ 1.69 nm and moving the the insert area a more detailed view is found for the insert. VDF images created from this area can be seen in Figure 4.8b. In this orientation the two phases are easily separated in the VDF. The same area was investigated after rotating the NW by 30° around the $[111]_{ZB}$ growth direction to orient it at the $[2\bar{1}\bar{1}]_{ZB}$ and $[1\bar{1}00]_{WZ}$. A VDF image from this scan was presented in Figure 4.6b.

The NWs have a well known structure and are usually oriented very close to a low index zone axis when the specimen is inserted into the TEM. This makes separating the phases manually through conventional DF and VDF a simple task. But in general the studied materials might have several phases and might be randomly oriented making this a more work intensive procedure. In these cases the template matching available in pyXem can be a powerful tool. Phase maps for both the main area and the insert area were created and are presented in Figures 4.9a and 4.9b. For the insert area the template matching procedure show a good correlation to the VDF images in Figure 4.8b. For the larger scan the simulated DPs are correctly fit for most of the ZB but the model for WZ is deviating towards the top of the scan.

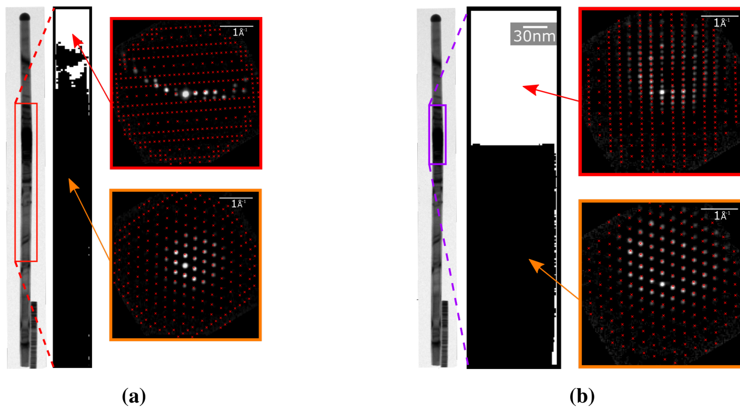

Figure 4.9: (a) Phase map from the main area obtained from template matching together matched simulated DPs for selected areas. (b) Phase map for the insert area together with matched simulated DPs.

In addition to VDF and template matching the SPED data can be analysed using the NMF routine also available in pyXem to identify the phases through machine learning. The partition of the crystal structures found using this method is presented in Figures 4.10a and 4.10b. The large scan have two different orientations of ZB due to the twin planes and WZ and so a partition of three was used for this scan giving three images with their respective pattern. For the small scan of the insert region the NMF routine was required to partition the data set into two parts.

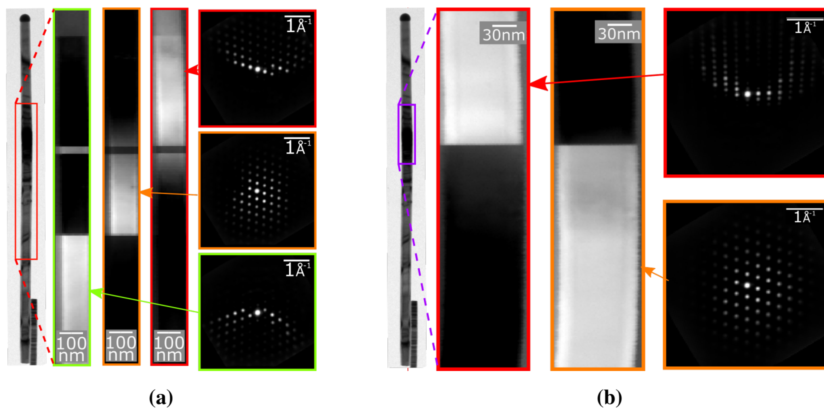

Figure 4.10: (a) NMF from main area requiring three partitions of the observed DPs (b) NMF results for the insert region requiring the data set to be sorted in two different patterns.

4.2 Orientation

Three twin planes were found in the lower part of the studied NW as marked in Figure 4.2b. This can also be seen from an orientation map using template matching as presented in Figure 4.11a. Here the differently oriented ZB regions are clearly separated as opposed to the phase map created from template matching. The template matching procedure is again observed to fit for most of the ZB phase but at the top some deviation is present. A

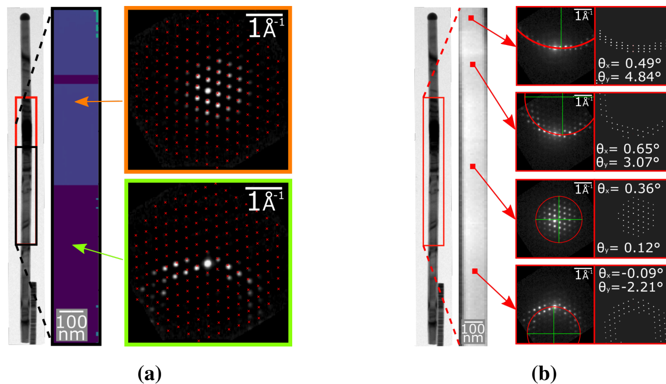

Figure 4.11: (a) An orientation map of the ZB part of the main area studied with SPED as marked by the black square on the BF NW map. (b) Estimated Ewald sphere intersections for different scan points of the NW and simulations from ReciPro of estimated tilt.

closer study of the twin area was performed. In Figure 4.12a a HRTEM image of the twin area in the NW can be seen together with FFTs created from the different orientations for clarification. From the HRTEM image this twin section was found to be 128 ± 1 stacking layers in the growth direction translating to 418 ± 4 Å. In Figure 4.12b a DF image, using the $00\bar{2}_{ZB}$ reflection of the twin section, can be seen. A SPED scan was performed on the twin section as well for analysis. A VDF image can be seen in Figure 4.13a where the $00\bar{2}_{ZB}$ reflection of the ZB region between the twin planes has been used as marked in the same figure. This gives a clear map of the twin section with sharp edges. Some thickness fringes can be seen towards the sides of the NW. Using template matching the different twin sections has been separated by creating an orientation map as seen in Figure 4.13b. In the upper left corner the simulated DP for the twin section can be seen marked as red crosses on top of the real DP. The observed twin region from this procedure can be seen to extend outside of the NW on the right side. Some increase in width toward the right side is also present in the orientation map. Finally the same twin sections can be separated using NMF methods. This was done for the same data set resulting in a clean map as seen in Figure 4.13c.

A gradual change in orientation is also observed along the growth direction of the NW due to bending. As the electron beam is moved along the NW the Ewald circle can be seen to shift in reciprocal space due to this bend as presented in Figure 4.11b obtained from SPED measurements. By estimating the position of the Ewald spheres intersection

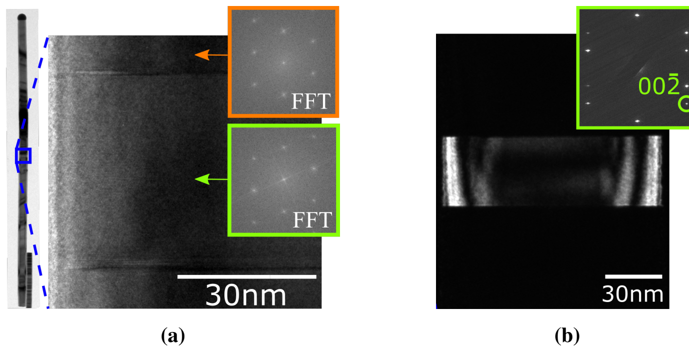

Figure 4.12: (a) HRTEM image of twin area together with FFT from the twinned section in green square and FFT above in orange square. (b) DF image of twin section created from $00\bar{2}_{ZB}$ reflection.

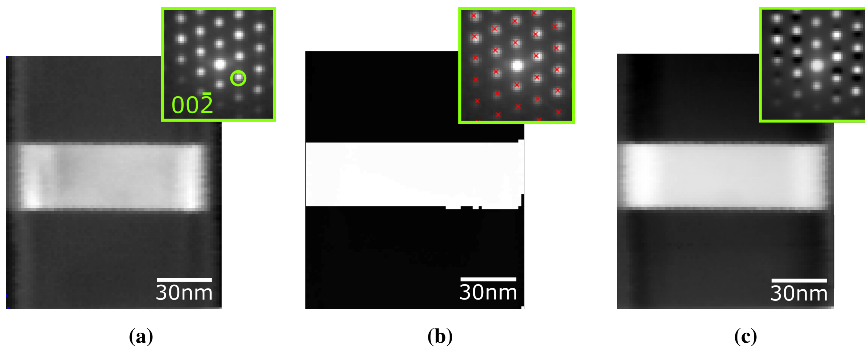

Figure 4.13: (a) VDF image of twin section from SPED measurement using the 002_{ZB} reflection marked in DP. (b) Orientation map from SPED measurements together with the real and simulated DP for the twin section. (c) NMF result for twin section together with the element found for the twin. NW was oriented at $[1\bar{1}0]_{ZB}$.

with the ZOLZ an estimate for the off zone tilts has been found as presented in the figure together with simulated DPs for the estimated tilts.

4.3 Composition

Figure 4.14a presents an overview image of the NW where the region EDS measurements were performed has been marked by a black box. A HAADF image was collected at the same region as seen next to the overview BF image. The HAADF images give z-contrast images, meaning contrast due to difference in atomic numbers. Heavier atoms scatter more and give higher intensity in these images. Because the Sb is a heavier atom than Ga and As, a higher intensity is observed for the insert. A sum spectra from collected EDS measurements are seen in Figure 4.14b where the characteristic X-ray energies of Ga, As and Sb are marked. In Figure 4.14c quantified maps of As, Sb and C are presented showing the presence of Sb. From this the composition in the inserted heterostructure was found to be ~ 15at.$\%$ Sb, ~ 35at.$\%$ As and 50at.$\%$ Ga. More detailed compositional variations across an insert have been studied in detail before [11, 12] and was not a focus in this study.

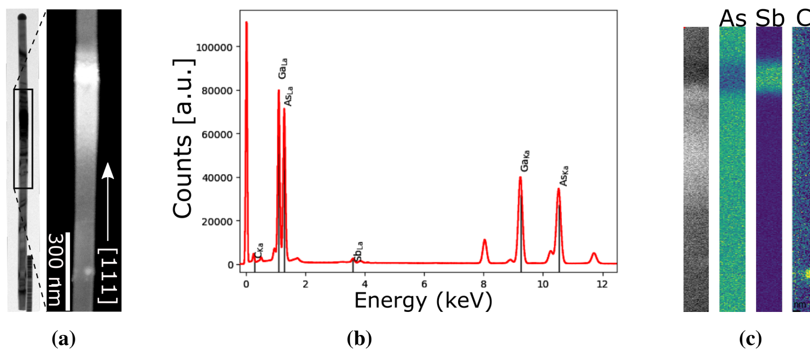

(a) (b) (c)

Figure 4.14: (a) HAADF TEM image of the region marked in the BF of the NW. (b) A sum spectrum of the detected X-ray photon energies collected in the EDS measurements where X-ray energies used for EDS map quantification are labelled. (c) A map of the raw EDS data is presented in grey next to quantified maps for As. The characteristic X-ray used for quantification are the $As_{K\alpha}$, $Sb_{L\alpha}$ and $C_{K\alpha}$. (The HAADF image and EDS data was collected by professor Antonius T. J. van Helvoort)

4.4 Strain

Finally the strain has been studied for the NW. The shape of the strained region can be seen in BF images of the insert as in Figure 4.15a where an increase in contrast can be seen due to the strain. The same effect can be seen in the VBF image obtained from the SPED data for the insert region as presented in Figure 4.15b. This gives an initial qualitative view of the strained area, but it does not give a quantitative measurement of the real strain in the insert nor does it distinguish between normal strains, shear strain and rotation. By using the pyXem packages for strain measurements on the SPED data the true strain has been estimated. This routine provides normal strains, shear strain and a rotation map. The shear strain is given as a relative change in the reflection distance and the rotation is given as angles in radians. This has been mainly done for two different camera lengths, 20 cm and 60 cm, and for two different convergence angles calibrated to be 1.3 mrad and 3.5 mrad (see Appendix C for α calibrations) with the NW oriented at the $[2\bar{1}\bar{1}]_{ZB}$ and $[1\bar{1}00]_{WZ}$ zone axis. Figures 4.18a-4.17c presents the strain found using the aforementioned parameters. Different reflections were also used for these strain maps as marked in the figures. In the $[2\bar{1}\bar{1}]_{ZB}$ and $[1\bar{1}00]_{WZ}$ orientation the DPs of WZ and ZB overlap and the corresponding reflections for WZ would be respectively 0002_{WZ} and $01\bar{1}0_{WZ}$. Strain and rotation maps have also been obtained for the NW when it is oriented at the $[1\bar{1}0]_{ZB}$ zone axis which is presented in Figure 4.20c. In this orientation the 111_{ZB} and $22\bar{4}_{ZB}$ reflections of the ZB phase has been used as these overlap with the 0002_{WZ} and $04\bar{4}0_{WZ}$ reflections of WZ.

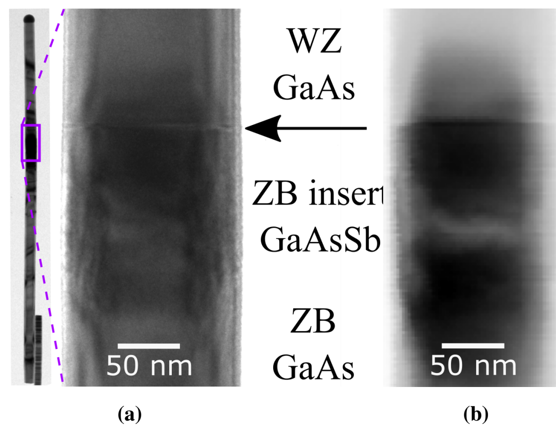

Figure 4.15: (a) A BF image of the insert region oriented at $[1\bar{1}0]_{ZB}$ and $[2\bar{1}\bar{1}0]_{WZ}$ and (b) a VBF image for the same region and orientation.

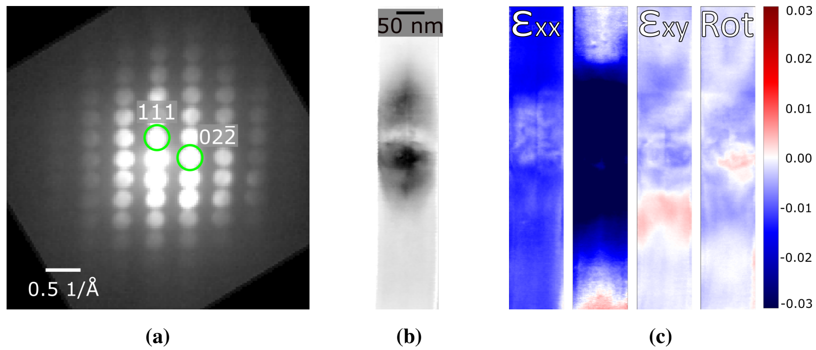

Figure 4.16: (a) DP obtained for NW oriented at $[2\bar{1}\bar{1}]_{ZB}$ and $[1\bar{1}00]_{WZ}$, camera length of 20 cm and $\alpha \approx 3.5$ mrad. (b) VBF image of strained region. (c) Strain and rotation maps from reflections marked in (a), strain is given as relative change in reflection distance and rotation is given in radians.

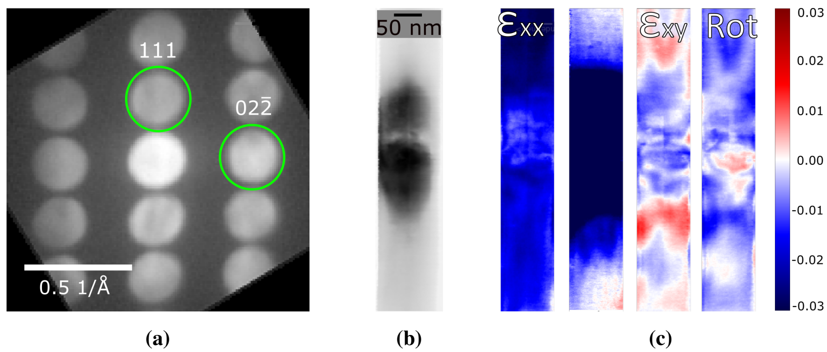

Figure 4.17: (a) DP obtained for NW oriented at $[2\bar{1}\bar{1}]_{ZB}$ and $[1\bar{1}00]_{WZ}$, camera length of 60 cm and $\alpha \approx 3.5$ mrad. (b) VBF image of strained region. (c) Strain and rotation maps from reflections marked in (a), strain is given as relative change in reflection distance and rotation is given in radians.

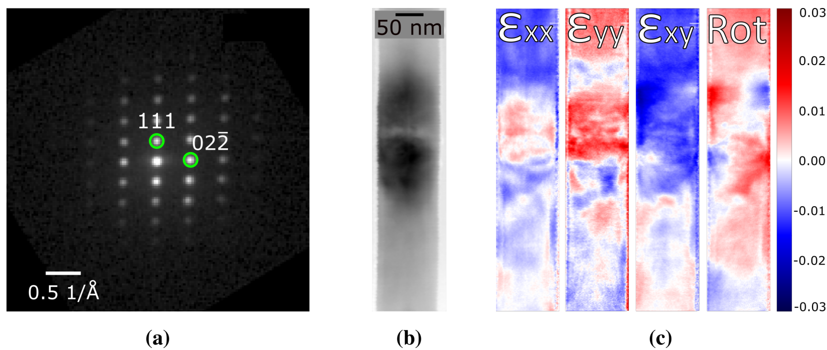

Figure 4.18: (a) DP obtained for NW oriented at $[2\bar{1}\bar{1}]_{ZB}$ and $[1\bar{1}00]_{WZ}$, camera length of 20 cm and $\alpha \approx 1.3$ mrad. (b) VBF image of strained region. (c) Strain and rotation maps from reflections marked in (a), strain is given as relative change in reflection distance and rotation is given in radians.

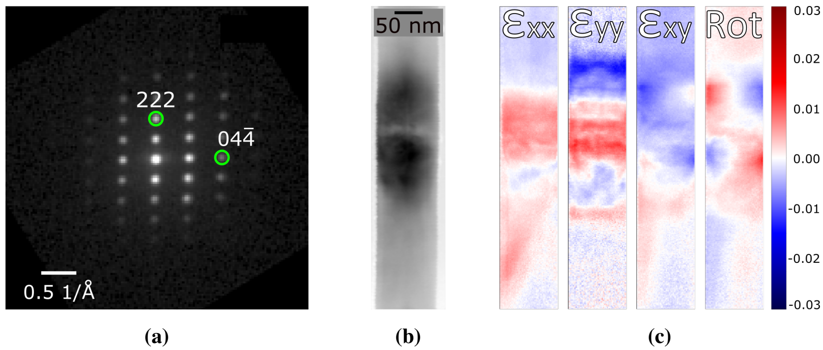

Figure 4.19: (a) DP obtained for NW oriented at $[2\bar{1}\bar{1}]_{ZB}$ and $[1\bar{1}00]_{WZ}$, camera length of 20 cm and $\alpha \approx 1.3$ mrad. (b) VBF image of strained region. (c) Strain and rotation maps from reflections marked in (a), strain is given as relative change in reflection distance and rotation is given in radians.

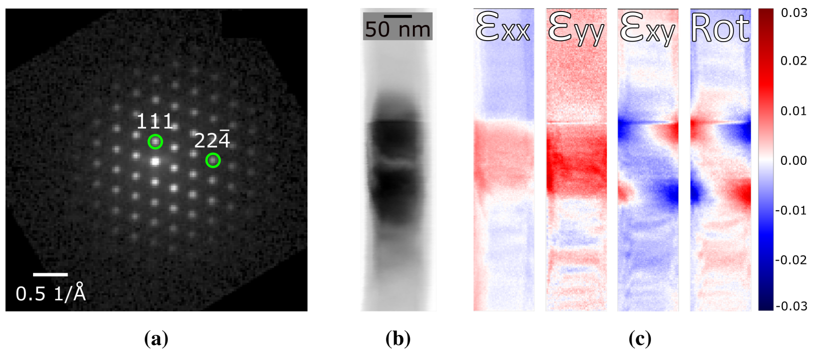

Figure 4.20: (a) DP obtained for NW oriented at $[1\bar{1}0]_{ZB}$ and $[2\bar{1}\bar{1}0]_{WZ}$, camera length of 20 cm and $\alpha \approx 1.3$ mrad. (b) VBF image of strained region. (c) Strain and rotation maps from reflections marked in (a), strain is given as relative change in reflection distance and rotation is given in radians.

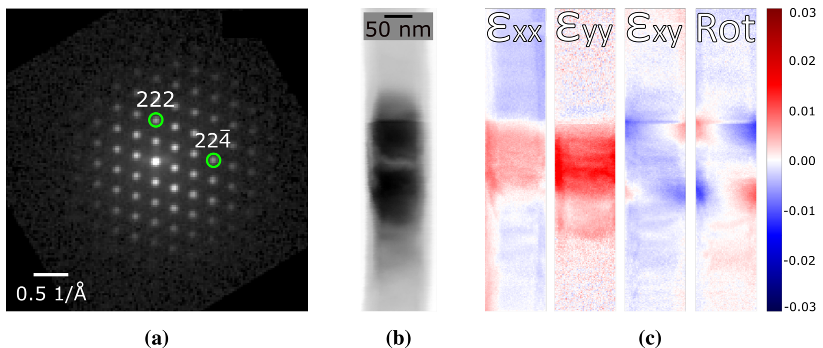

Figure 4.21: (a) DP obtained for NW oriented at $[1\bar{1}0]_{ZB}$ and $[2\bar{1}\bar{1}0]_{WZ}$, camera length of 20 cm and $\alpha \approx 1.3$ mrad. (b) VBF image of strained region. (c) Strain and rotation maps from reflections marked in (a), strain is given as relative change in reflection distance and rotation is given in radians.

Chapter 5

Discussion

The goal of this work is to characterise all aspects relevant for a NWs properties including crystal phases, defects, composition and strain. Several NWs were investigated (See Fig. 4.1) from which a characteristic NW were chosen containing all structural features of interest (Fig. 4.1a). In the following the results found, using both conventional TEM techniques and SPED measurements, for this NW will be discussed in separate sections for crystal structure, orientation, composition and strain.

5.1 Crystal structure

Conventional TEM offers different ways to identify the crystal phase. Here only two phases are expected as presented in the theory, which can be readily identified by their characteristic DPs (See Fig. 2.9 and 2.11). Characterising the phases using DF imaging in the TEM for these NWs is a straight forward method when the crystal structure and relevant zone axis are known and chosen wisely. In Figure 4.3 a clear transition between the different phases and twin planes are seen. The DF imaging is convenient for analysing larger areas, but the best spatial resolution is obtained from HRTEM imaging. In the JEOL JEM 2100F used here the resolution is not high enough to distinguish single atom columns, but individual stacking layers can be seen for the $[1\bar{1}0]_{ZB}$ and $[2\bar{1}\bar{1}0]_{WZ}$ orientation (See Fig. 4.5a). Stacking fringes are also discernible for the $[2\bar{1}\bar{1}]_{ZB}$ and $[1\bar{1}00]_{WZ}$ orientation (Fig. 4.5c), but requires a very precise NW orientation and is on the limit of what can be resolved. But this increased resolution comes at the cost of low field of view as a high magnification is required. Figure 5.1 shows a schematic of roughly the maximum field of view achievable with HRTEM resolution. Thus investigating larger areas is work intensive using HRTEM imaging. Separating the phases using SAED to find the DP for a selected area is the method used (See Fig. 4.5b) with the lowest spatial resolution. An aperture is then introduced in the image plain of the TEM to choose which parts of the NW is to be illuminated. The smallest aperture available limits the interaction area to ~ 150 nm, or roughly the width of the NW as illustrated in Figure 5.1. The DF method is a good compromise for analysing larger areas with a decent resolution. Also small details are noticeable in the DF images like the SFs in the WZ region above the insert (see Fig. 4.3b).

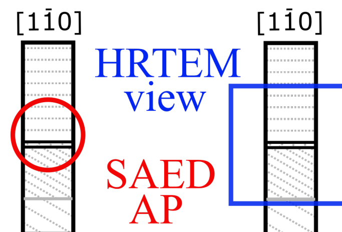

Figure 5.1: The size of the smallest SAED aperture available in the JEOL JEM 2100F (red circle) relative to the width of the NW illustrated by a schematic drawing of the insert area. The blue square illustrates the approximate max field of view using HRTEM where the fringes characteristic for the phases can still easily be distinguished.

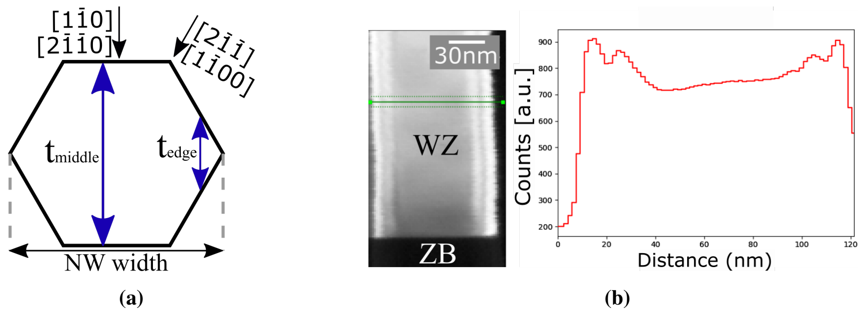

Figure 5.2: (a) A cross-section model from the hexagonal NW. (b) VDF of WZ created from $01\bar{1}0_{WZ}$ reflection together with intensity profile across the width of the NW.

In the DF images the contrast is changing making the interpretation more demanding. The precession reduce this effect as seen in the VDF in Figure 4.6b. When creating VDF images from SPED scans, using reflections within the precession angle, the intensity fluctuations can be seen to decrease for the main area too (Fig. 4.8) when compared to the DF images of the NW. This is because when the electron beam is processed, dynamical effects are averaged out as explained in section 2.15 which lead to a more even contrast along the NW. This effect has been reported by others [31]. But some change in contrast within each phase is still observed. In Figure 5.2b a closer view of the VDF image obtained for the WZ region in the results (Fig. 4.8b) is given. The intensity profile across the NW can be seen to fluctuate towards the NW edges. As the NWs have an hexagonal shape as modelled in Figure 5.2a, the thickness vary towards the edges of the NW. In section 2.11 the intensity of a reflection in DPs was explained to follow equation 2.29 which reveals a sinusoidal relationship between the observed intensity and sample thickness. When the NW is oriented at $[1\bar{1}0]_{ZB}$ and $[2\bar{1}\bar{1}0]_{WZ}$ the middle of the NW have the flat sides facing upwards as seen in Figure 5.2a. A more even intensity profile will therefore be seen at the middle. And so, three dimensional qualities can be inferred from the two dimensional virtual images created from SPED stacks.

When studying the phases of the NW using template matching for the main area (Figure 4.9a) the structures were found to be correctly determined for most of the ZB region, but the top part of the scanned region was observed to be deviating. This is coupled to the NW bending as seen from the DPs in Figure 4.9a. As the NW bends, less reflections are present in the DPs and towards the higher part of the SPED scan the number of reflections available for the template matching procedure seem to result in a mismatching. The reason for this is that the template match is performed with a fixed maximum excitation error. But when the NW bends in the direction of the electron beam the reciprocal lattice is rotated as schematically drawn in Figure 5.3. This changes the effective excitation error and for large enough tilts the scattering condition (Eq. 2.23) is no longer satisfied and the reflections are not seen in the DP. The phase is however identified as WZ above the insert. Smaller sections, which experience less bending across the scan, give better results as was seen in Figure 4.9b. A closer view of the phase change is given here in Figure 5.4b. A slightly uneven transition from ZB to WZ is observed where the ZB phase can be seen to

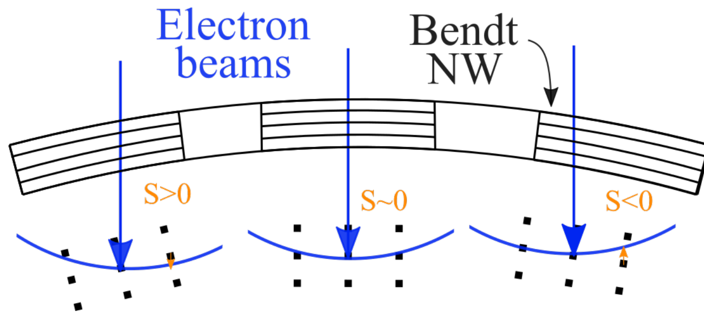

Figure 5.3: Schematic representation of the change in scattering excitation error for a bendt NW.

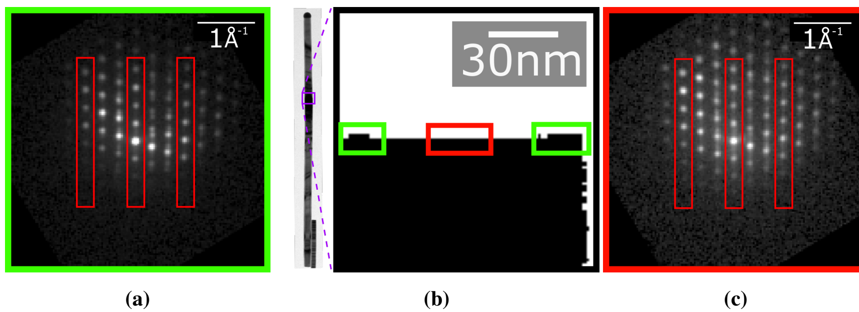

(a) (b) (c)

Figure 5.4: (a) DP seen towards edges of the NW inside green squares in (b) at the phase change. (b) Close view of the phase transition from template matching of insert region. (c) DP seen in the middle of the NW at the phase change marked by red square in (b).

extend further in the growth direction towards the edges of the NW. As the NWs grow in monolayers the phase change should be happening in between growth planes, not within one plane. The transition from ZB to WZ is also observed to be straight for the insert region in HRTEM images (Figure 4.5a). When looking at the DPs collected close to the edges of the NW in Figure 5.4a, the patterns strongly resemble the DP as seen from two twinned ZB regions where the reflections inside the red boxes in the DPs are the same for two ZB twin orientations. From the HRTEM in Figure 4.5a a small twin (6 111-layers wide) region at the phase change was indeed found. But moving into the NW, at the same height in the scan, the observed DPs starts to get more intensity (i.e. maxima) between the reflections in the common ZB columns in the red squares in the DPs as seen in Figure 5.4c. The DP obtained from WZ should have reflections in between the ZB reflections and this could make the template matching recognise it as WZ at the middle.

One reason why the edges have been labelled differently than the middle could be a result of the NW being tilted slightly. Imagine that the electron beam is positioned just below the WZ phase as illustrated in Figure 5.5a. Towards the edges of the NW the effective specimen thickness experienced by the electron beam is less than in the middle as illustrated by the dashed lines. This is a result of the the hexagonal shape of the NW as illustrated earlier in Figure 5.2a. In this case the electron beam could pass through only

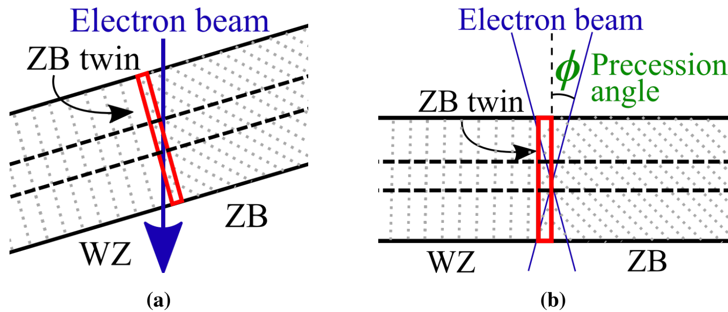

Figure 5.5: (a) A model of the tilted NW at the phase change. Dotted grey lines symbol phase stacking, dashed black lines are effective thickness towards thinner edge of NW (b) A model of precessed electron beam passing through NW. ϕ is the precession angle.

ZB towards the edges resulting in the DP seen in Figure 5.4a. If the beam passes through the middle of the NW the increased thickness could cause some WZ interaction as the electron beam might then pass through both phases due to the tilt. Looking at the intensity in the DP presented in Figure 5.4c the Ewald sphere intersection with the reciprocal space can be seen to be shifted slightly in the vertical direction corresponding to a tilt of the NW along the growth direction at that point. Assuming a NW tilt of $1°$ and a NW thickness of 130 nm, simple geometric considerations gives that the beam passes through about 2.3 nm along the length of the NW. The thickness of the small twin section at the phase change was about 2 nm. When the electron beam is closer to the NW edges the effective thickness experienced by the beam would be thinner as illustrated with dashed lines in Figure 5.5a. Thus the NW beam would pass through only the ZB at the thinner edges, where the tilt has less of this effect, and both ZB and WZ at the thicker middle.

An alternative explanation worth considering which could cause a similar effect is broadening of the beam within the sample, especially when precessing the electron beam in the SPED measurements. This makes the precessed beam width increase away from the eucentric height which it precesses about. A sketch for this can be seen in Figure 5.5b. The result is that more of the crystalline material in the growth direction of the NW is being interacted with as the specimen thickness increase. For the middle of the NW where it has a thickness of more than 100 nm the beam would then interact with more of the WZ phase. For the SPED measurements taken here, a precession angle of about $0.65°$ was used (see Appendix D). If we assume the NW is positioned with the eucentric height in the middle of the NW, whose width is 130 nm, the beam width at the side of the NW would be ~ 0.7 nm wider corresponding to about two d_{111} stacking layers. A similar argument could be made for the convergence angle of the electron beam which would also increase for a higher sample thickness. These effects are much smaller than the sample tilt, but will add to the total increase of beam width and thus the amount of crystalline material in the growth direction which is interacted with. In addition to the aspects of beam tilt and precession, the thicker part in the middle will increase both dynamical scattering and the background noise which results in increased intensity between reflection in the common reflection columns in Figure 5.4 as well. The combination of these effects results in the template

matching getting a better fit for the WZ as this phase would have intensities between the ZB reflections in the common columns. All of that being said, the pixel size corresponds to 1.69 nm (see Appendix F) in the real space and so this uncertainty is not a big problem if the goal is to simply characterise the phases and transition point. In conclusion thinner samples are better as the effects discussed above are then less significant.

In the images obtained from NMF routines for the main area seen again in Figure 5.6b, artefacts which seem to be caused by the bending present in the NW is again observed. The NMF routine does not consider the observed DPs as anything else than random independent images which it here has been forced to divide into three different groups, also called components. As the beam is scanned along the NW the Ewald sphere cuts out a circle in the ZOLZ which is gradually shifted in opposite directions at the top and bottom of the scan. When the NMF algorithm sorts out the patterns, the position of the Ewald sphere in reciprocal space becomes an additional difference between DPs obtained from the top, middle and bottom part of the NW. For the lower ZB orientation in the main area (Green box in Fig 5.6b) the NMF routine give results in good agreement with the DF TEM and VDF images. But for the ZB orientation seen towards the higher part of the NW, and which borders to the WZ region, the NMF routine is less successful in classifying the correct phases (Orange and red squares in Figure 5.6b). For the middle of the scanned area the NW is very close to the $[1\bar{1}0]_{ZB}$ zone axis. Towards the top on the other hand it is bent away as seen in the red square in Figure 5.6b. The collected DPs can be seen as a convolution of the Ewald circle and the on zone DPs as illustrated in Figure 5.6a. This results in the NMF routine to separate the higher ZB phase into two different, one of which also includes the WZ region on top (Orange and red squares Figure 5.6b. At this point the bending of the NW is large enough for most reflections to not fulfil the scattering condition anymore. This gives the NMF routine less reflections to use for sorting the patterns. On the other hand, as the NW bends, the Ewald sphere intersection with the ZOLZ becomes an ever more characteristic feature of the observed DPs. As for the phase map from template matching, also the NMF routine can be seen to give a more clear result for the smaller scan of the insert area in Figure 4.10b. For this region less bending is present due to the smaller scan, and a sharp transition between ZB on the bottom to WZ at the top is observed. So, NMF can work giving clear maps and components in agreement with observed physical DPs, however bending in the beam direction can lead to sorting errors.

And so to sum up this section, the conventional TEM methods provide a very high resolution using HRTEM imaging which the SPED cannot achieve. The DF TEM imaging is a good compromise between field of view and resolution, but a lot of contrast variation is seen. The VDF images from SPED data show less intensity variation than the DF TEM imaging and as the choice of reflections to use for the VDF is done virtually on the data set in post-processing it allows for far greater amounts of information. In addition to VDF, the template matching and NMF routines can be used to great effect when the bending is not too large. But these should be interpreted with care.

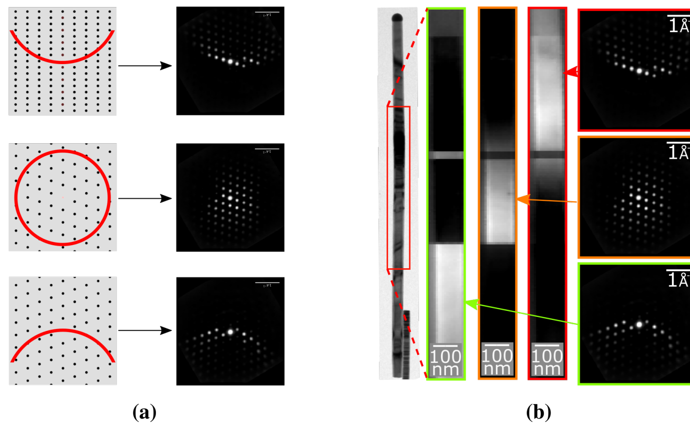

(a)

(b)

Figure 5.6: (a) Intensity observed when the reciprocal lattice and Ewald sphere intersect. (b) NMF results from main area with forced sorting in three groups.

5.2 Orientation

Separating the different orientations of the NW using the orientation mapping procedure of pyXem yielded the map presented in Figure 4.11a where the different orientations of ZB in the lower part of the NW are clearly distinguished and in agreement with the orientations found from DF images for reference. The orientation mapping encounter the same deviations due to NW bending as the template matching. This is expected as the same template library is used for the orientation mapping as in phase mapping. For the orientation mapping we are only interested in the orientation of a phase and so the WZ part of the main area has been left out in the orientation map. Orientation information can also be found from NMF results. Looking at Figure 4.10a in terms of orientation mapping the two twinned ZB orientations are separated, although the higher ZB orientation is separated into two groups. Information about the change in orientation due to bending can also be be found from the NMF results due to the Ewald sphere shift as discussed in the previous section. For a closer scan of the insert area as seen in Figures 4.13a - 4.13c the same tendency as for the insert area is seen that the images obtained from all SPED procedures give good and clear results in agreement with what is observed using conventional TEM techniques.

The bending observed for the NW was presented in Figure 4.11b. By comparing the coordinates between the central beam and the centre of an estimated Ewald circle, an estimate for the amount of bending was found. This circle was estimated for the four points as marked in Figure 4.11b. At the centre of the SPED scan the NW is oriented approximately at the $[1\bar{1}0]_{ZB}$ zone axis. Above the insert in the WZ phase the NW was found to be tilted in the vertical growth direction relative to the $[2\bar{1}\bar{1}0]_{WZ}$ zone axis by an angle of $\theta_y \approx 4.84°$. Approximately 250 nm lower, just below the insert in the ZB phase, a tilt of $\theta_y \approx 3.07$ ° was found. In the middle of the scan a deviation of $\theta_y = 0.12°$ was

found and for the lower $\theta_y = -2.21°$. The distance between the measurements in the ZB phase are ~ 500 nm. And so the NW seems to bend along the growth direction in the ZB phase by $2 - 3°$ every 500 nm or $\sim 5.3 \cdot 10^{-3}$ °/nm. Over the insert the NW can be seen to bend more at $\sim 7.1 \cdot 10^{-3}$ °/nm. Looking back at the overview BF image of the NW (Fig. 4.1a) an increase in the bending can be directly observed as well. When the NW composition is changed and strain is introduced as a result, defects and stacking faults can often be introduced [32]. Here it can be seen to also result in additional bending of the NW.

As for the crystal phase studies also the orientation studies, to separate the twinned ZB orientations, must be done on the $[1\bar{1}0]_{ZB}$ and $[2\bar{1}\bar{1}00]_{WZ}$ zone axis. In this orientation the difference in stacking layers can be detected. From HRTEM imaging a precise value for the length of a twin section can be determined if that is of interest. But the low field of view for HRTEM imaging makes the DF more convenient when larger areas are studied using convention TEM. The SPED measurements provide VDF, orientation maps and NMF results which look very good for the small twin section. The SPED results all show less complicating contrast variations than conventional DF. For larger regions where more bending is present the results are more challenging to interpret. From the SPED results also information about the amount of bending can be extracted in post-processing. The same process would have been much more work intensive using conventional TEM techniques where DPs from different regions would have to be collected individually.

5.3 Composition

For the HAADF images taken of the NW in Figure 4.14a, carbon contamination from the electron beam can be seen in the lower part of the image. The carbon leads to more scattering due to the sample being thicker there resulting in the increased intensity. From a line trace performed on the HAADF image in Figure 5.7a shows that the intensity falls below the insert where the composition is constant GaAs. This is a result of the NW bending through the oriented zone axis affecting the scattering. The intensity can be seen to be higher in the region close to the insert where it has been oriented on zone. As it slowly bends away from this zone, less electrons are fulfilling the scattering condition, and lower intensity is observed in the HAADF image. This can also be seen to have an effect on the EDS measurements [14]. In the raw EDS map presented in Figure 4.14c a varying intensity for the evenly thick GaAs below the insert can be seen as the NW bends away from the oriented zone axis. When creating quantified EDS maps of the NW these effects can be accounted for (See Appendix O). The EDS measurement are used qualitatively to prove that there is a GaAsSb insert and where in the NW it is located. For quantitative analysis of EDS measurements it is advised to avoid low index zones to reduce the effects of bending [14].

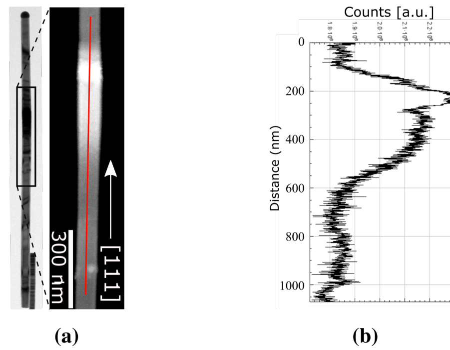

Figure 5.7: (a) A line trace has been taken from red line marked in HAADF (b) Intensity along NW from line trace in HAADF in (a).

5.4 Strain

The main added technique developed here, which is not covered well by established conventional TEM, was to deduce strain levels around heterostructures within NWs. The open-source pyXem package perform strain measurements by measuring the distance to a given reflection in the obtained DPs for all scan points. For the collection method used on the Jeol Jem 2100F, as explained in section 3.3, a pattern size of 144 by 144 pixels is obtained for the DPs. This limits the precision at which the position of a reflection can be determined. DPs collected with a camera length of 20 cm were found to have a resolution in terms of reciprocal Ångstrøm of 0.032 Å^{-1}/pixel (Appendix B). The lattice parameter of pure GaSb is $\sim$ 1.078 times larger than pure GaAs, so the distance to the 111_{ZB} reflection for GaSb would be $\sim$ 0.927 of the GaAs distance due to the inverse relationship expressed by Eq. 2.12. In terms of Å^{-1} this is a change of $\sim$ 0.022 Å^{-1} in the DP, smaller than the image resolution. For the studied NWs only some percentage of the As is changed for Sb. Assuming that Vegards law holds [33], which state that the lattice parameter changes linearly with the composition, the change in lattice parameter will always be less than this value. This means that the change in reflection distances is far below the resolution of the DPs collected at a camera length of 20 cm. However, as the centre of mass for a reflection is estimated, a sub-pixel precision determination of the reflections is possible. The precision of this method should increase with increasing width of a reflection in the DPs. For this reason a beam convergence angle α that maximise the reflection diameters, without individual reflections touching, was thought to be a good starting point for collecting reliable strain maps using a centre of mass method.

The largest possible convergence angle α, where the reflection disks don't overlap, depends on the zone axis at which the NW is oriented. Figure 5.8 presents a magnified view ($\sim$ 50x50 pixels) from the centre of DPs obtained from the SPED scans for strain measurements. To maximise the reflections, a convergence angle α that gave a ratio between the diameter of the reflections a in Figure 5.8a and the distance between the closest spaced reflections b to be 0.9 was chosen (see Appendix C and J). If the NW is oriented at the

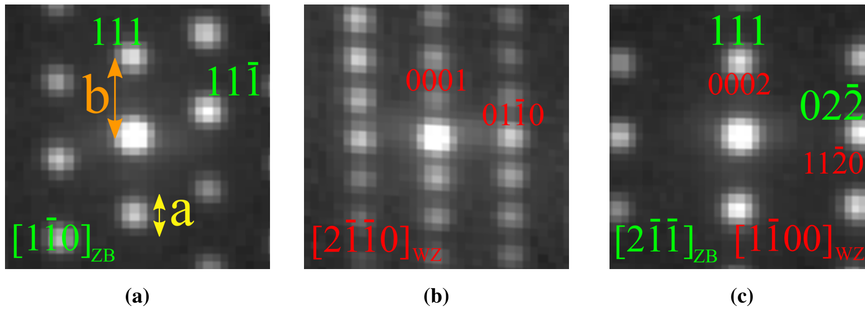

(a) **(b)** **(c)**

Figure 5.8: Magnified view of collected DPs for (a) ZB at $[1\bar{1}0]_{ZB}$ zone axis, (b) WZ at $[2\bar{1}\bar{1}0]_{WZ}$ zone axis and (c) both ZB and WZ when crystal structure is rotated 30° about $111_{ZB}/0001_{WZ}$ from zone axis in (a) and (b).

$[1\bar{1}0]_{ZB}$ and $[2\bar{1}\bar{1}0]_{WZ}$ zone axis, the theoretically maximum value would be $\alpha \approx 1.72$ mrad due to the densely spaced 0001_{WZ} WZ reflections in Fig. 5.8b. If the NW is rotated by 30° around the $[111]_{ZB}$-growth direction to the $[2\bar{1}\bar{1}]_{ZB}$ and $[1\bar{1}00]_{WZ}$, the densest reflections would be the 111_{ZB}/0002_{WZ} reflections seen in Figure 5.8c. This allows for a larger maximum convergence angle of $\alpha \approx 3.56$ mrad, giving more pixels to determine the centre of mass position of a reflection. Another advantage with this orientation is that the DPs look the same for both WZ and ZB. This makes it easier to measure the strain across the phase change as it essentially can be done for all observed reflections. SPED measurements were first collected in the $[2\bar{1}\bar{1}]_{ZB}$ and $[1\bar{1}00]_{WZ}$ orientation to compare the different choices of α angles (Fig. 4.16 and 4.18). All SPED data used for strain measurements were performed with precession to make the reflections more even as visualised in Figure 4.7. In the Jeol Jem 2100F used for the SPED measurements collected for this thesis, two convergence angles of $\alpha_1 = 1.3 \pm 0.3$ mrad and $\alpha_2 = 3.5 \pm 0.3$ mrad (see Appendix C) were used at a camera length of 20 cm. From Figure 4.16a, presenting the results for a large α_2 angle, the $111_{ZB}/0002_{WZ}$ reflection can be seen to overlap with the central beam making the centre of mass calculations fail resulting in unlikely strain maps (Fig. 4.16). The strain maps created from the smaller convergence angle however yields better results (Fig. 4.18). Here the strain profiles from the ϵ_{yy} obtained from the two α angles, at the same camera length of 20 cm, can be seen in Figure 5.9a and 5.9b for a closer comparison. For the GaAsSb heterostructure, a positive strain should be observed due to the larger lattice parameter. For the large α_2 however, the ϵ_{yy} strain is found to fall towards the insert, which is nonphysical. For the smaller α_1 on the other hand, a positive strain is observed towards the heterostructure and less negative strain is present for the unstrained GaAs regions below the insert. Thus a lower convergence angle α is found to be preferred where the center-of-mass method is not affected by overlapping reflections and the uneven intensity of the reflections (See 4.7). However, large fluctuations are observed for the unstrained GaAs regions far from the insert where the strain profile should be smooth and values low.

The next step attempted to improve the measurements was to increase the camera length. This would make the reflections cover more pixels in the image to hopefully further

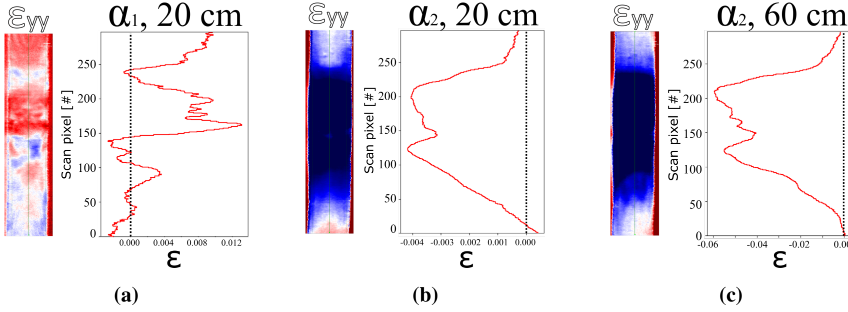

Figure 5.9: ϵ_{yy} strain profiles found using (a) a camera length of 20 cm, $\alpha \approx 1.3$ mrad, (b) a camera length of 20 cm, $\alpha \approx 3.5$ mrad and (c) a camera length of 60 cm, $\alpha = 3.5$ mrad. For all these the $111_{ZB}/0002_{WZ}$ and $02\bar{2}_{ZB}/11\bar{2}0_{WZ}$ reflections were used. The dotted line marks zero strain.

increase the precision of the strain analysis. In Figure 4.17 this was presented for the larger convergence angle where the reflections can be seen to no longer intersect. However, the change of camera length does not result in much improvement as can be seen for the ϵ_{yy} in Figure 5.9c compared to the strain profile obtained for the lower camera length next to it. Hence the number of pixels inside the reflections are found to not be the limiting factor for these measurements. The same comparison was also done for the small convergence angle α_1 from which similar results were found (See Appendix I). The larger camera length reveals that the intensity within the reflections is uneven for the large convergence angle, making the centre of mass calculation problematic (Fig. 4.17a).

Next, reflections further out in reciprocal space were investigated as these will move more and therefore might provide better measurements. In terms of field of view in reciprocal space at a camera length of 20 cm, the $666_{ZB}/000(12)_{WZ}$ reflection could theoretically be reached. But this far from the central beam, the reflection is weak and disappears for even small deviations from the zone axis. The bending present in this NW limits this choice of reflection to the $222_{ZB}/0004_{WZ}$ for ϵ_{yy} measurements. In Figure 4.19 the results from using the $222_{ZB}/0004_{WZ}$ and $04\bar{4}_{ZB}/22\bar{4}0_{WZ}$ reflections was given. From Figures 5.10a and 5.10c the ϵ_{xx} strain profile along the NW is presented for comparison of the effects of increasing the reflection distances. Above the insert the strain is observed to be less negative for the unstrained GaAs WZ region when the $04\bar{4}_{ZB}/22\bar{4}0_{WZ}$ reflection is used as pointed out by red arrows in the figures. The strain profile still has a nonphysical shape for the GaAs regions as this should be unstrained, however less fluctuations are observed in the map in Figure 5.10c. Improvements are also observed for the ϵ_{yy} strain in Figures 5.10b and 5.10d where the fluctuations in the unstrained GaAs regions again decrease for increased reflection distance as indicated by green arrows. Far better precision is achieved in the GaAs regions far from the insert and less deviation from the unstrained value. Thus reflections further out in reciprocal space are found to be preferred.

Strain measurements on this NW based on SPED have been done before by Duncan N. Johnstone et al. [17], one of the main developers of the pyXem library. These strain measurements were performed on GaAsSb NWs similar to the one studied in the present

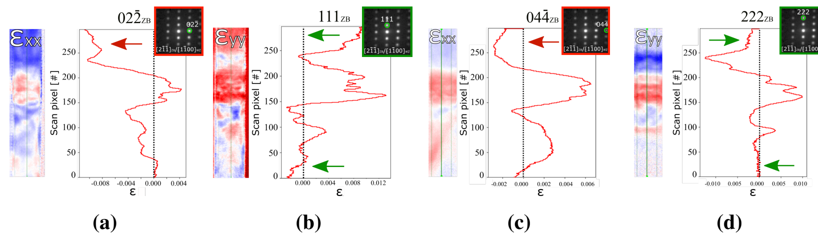

Figure 5.10: Strain maps obtained from $[2\bar{1}\bar{1}]_{ZB}$ and $[01\bar{1}0]_{WZ}$ zone, camera length 20 cm and $\alpha_1 \approx 1.3$ mrad. (a) ϵ_{xx} strain profile using reflection $02\bar{2}_{ZB}$, (b) ϵ_{yy} strain profile using reflection 111_{ZB} (c) ϵ_{xx} strain profile using reflection $04\bar{4}_{ZB}$ and (d) ϵ_{yy} strain profile using reflection 222_{ZB}. The dotted line marks zero strain.

work, oriented at the $[1\bar{1}0]_{ZB}$ and $[2\bar{1}\bar{1}0]_{WZ}$ zone axis. A strain measurement in this orientation was performed here too as presented in Figure 4.20 to investigate if this is a better orientation. As a smaller α angle was found to be preferred, the dense WZ DP for the $[2\bar{1}\bar{1}0]_{WZ}$ orientation (Fig. 5.8b) is no longer a restricting factor. For this orientation the chosen reflections are the 111_{ZB} and $22\bar{4}_{ZB}$ as they are perpendicular to each other and oriented along respectively the growth and radial direction of the NW. They also have the same position for both ZB and WZ, making it possible to map continuously across the phase change. For the WZ phase they would be indexed as 0002_{WZ} and $03\bar{3}0_{WZ}$ respectively. Considering first the ϵ_{xx} obtained from the two orientations in Figure 5.11a and 5.10c, a higher precision is observed for the unstrained GaAs material for the $[1\bar{1}0]_{ZB}$ orientation. The same is observed when comparing ϵ_{yy} using the $111_{ZB}/0002_{WZ}$ reflection (Fig. 5.10b and 5.11b). Thus the $[1\bar{1}0]_{ZB}$ orientation is found to provide better results with higher precision for the unstrained GaAs.

The choice of reflections can also be studied in the $[1\bar{1}0]_{ZB}$ orientation. Increasing the $22\bar{4}_{ZB}/03\bar{3}0_{WZ}$ reflection to $44\bar{8}_{ZB}/06\bar{6}0_{WZ}$ result in low signal-to-noise ratio, but the 111_{ZB} can be increased to 222_{ZB} as for the other orientation. A comparison for the ϵ_{yy} determined by using the 111_{ZB} and 222_{ZB} reflection for this orientation is presented here in Figure 5.11b and 5.11c. From this, increased accuracy and precision is observed for the 222_{ZB} reflection where the strain is approximately zero for the unstrained GaAs away from the insert and less fluctuation is present as marked by the green arrows in Figure 5.11. One could potentially go to 333_{ZB} reflection as well, however the bending present in the NW makes this problematic as the 333_{ZB} reflection is only present in the higher part of the SPED scan. A workaround for this could be to measure strain using the 333_{ZB} for the lower part of the SPED scan and then $\bar{3}\bar{3}\bar{3}_{ZB}$ for the upper part as this has intensity only for the upper part of the SPED scan (see Appendix I). Doing this requires a different reference region to be used for the two scans potentially giving an unequal offset on the two strain maps making interpretation of the strain difficult. Thus the same conclusion is found for the $[1\bar{1}0]_{ZB}$ orientation that improved results are obtained for reflections further out in reciprocal space, although NW bending limits the possible distance.

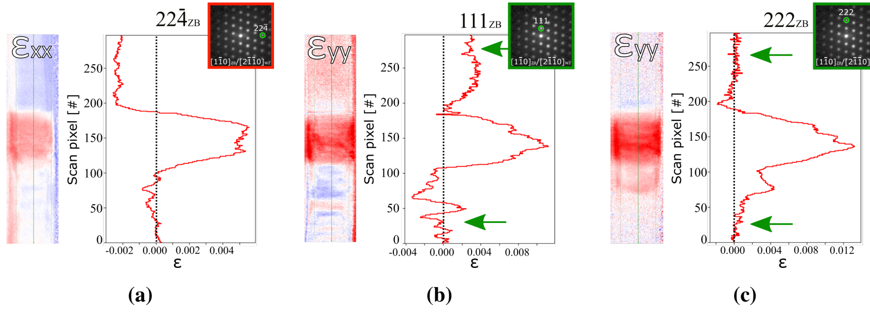

Figure 5.11: Strain maps obtained from $[1\bar{1}0]_{ZB}$ and $[2\bar{1}\bar{1}0]_{WZ}$ zone, camera length 20 cm and $\alpha_1 \approx 1.3$ mrad. (a) ϵ_{xx} strain profile using reflection $22\bar{4}_{ZB}$, (b) ϵ_{yy} strain profile using reflection 111_{ZB} and (c) ϵ_{yy} strain profile using reflection 222_{ZB}. The dotted line marks zero strain.

To sum up so far, the large α_2 value cause fluctuations in the intensity within each reflection in the DP and makes it difficult to estimate the strain using a centre of mass calculation. When decreasing α, the reflections get a more uniform intensity and normal strains are observed for the insert area as expected. Changing the camera length does little to the results as seen from comparing Figures 4.16c and 4.17c and so the number of pixels is found to not be the limiting factor. The choice of reflections further out in reciprocal space is limited due to the NW bending but are found to provide higher precision strain maps. In addition to the reflection choice the zone axis also affects the strain maps obtained. From the discussions here the optimal parameters for collecting strain maps are thus found to be a small convergence angle α, low camera length, using reflections as far out in reciprocal space as possible with a good signal and with the NW oriented at the the $[1\bar{1}0]_{ZB}$ and $[2\bar{1}\bar{1}0]_{WZ}$.

The strain presented in Figure 4.21 is then taken to be the strain present in the NW. In the VBF image of the insert area in Figure 4.21b the strained region seems to extend into the GaAs regions, both above and below the insert, than what is observed in the measured normal strains. Thus the contrast in the VBF images seem be a result of shear strain and rotation which is seen to extend further into the GaAs regions in Figures 4.18 and 4.20. This shear strain and rotation is present at the interface between the GaAs and GaAsSb as the insert will be pulled inwards due to the smaller lattice spacing of GaAs as illustrated in the model in Figure 5.12a. At the edges of the NW this would cause the crystal structure to be tilted relative to the sides of the NW as it gradually changes dimension. At the edges of the NW this would be seen as a rotation which will be in opposite direction for opposing edges of the NW. For the middle of the NW the two opposing sides along the beam path will also be tilted, but along the beam direction as illustrated in Figure 5.12b for the NW oriented at the $[1\bar{1}0]_{ZB}$ and $[2\bar{1}\bar{1}0]_{WZ}$. This will not cause a rotation in 2D representation of the reciprocal space seen in the ZOLZ, but rather a small shift of the Ewald circle. From the rotation map in Figure 4.20c, a maximum rotation of ~ 0.01 radians or $\sim 0.57°$ is found at the edges.

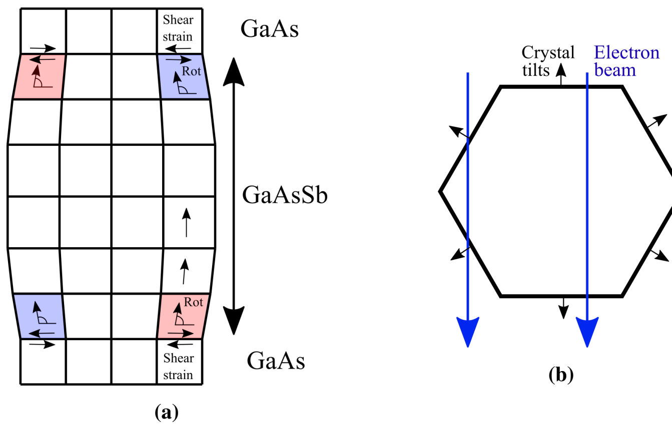

Figure 5.12: (a) A model of a NW as seen from the side with larger lattice parameter at the centre. Red squares represent clockwise rotation and blue counterclockwise. (b) NW seen along $[111]_{ZB}$ and $[0001]_{WZ}$. The black arrows illustrate the tilting crystal due to expanding lattice parameter.

From these studies the SPED measurements are to allow for much more information about the strain to be investigated. Where the conventional TEM techniques used here stop at a qualitative view of the strain field, the SPED measurements goes further to provide quantitative estimates for the strain. Care must be taken when choosing reflections as material characteristics, here in particular bending, can render some unsuitable. The precession available in the SPED technique however improves the field of view in reciprocal space counteracting this. The precession also allows for the electron beam to be focused so that a high spatial resolution is achieved whilst maintaining DPs with reflections of even intensity for smaller convergence angles [16].

Chapter 6

Conclusion

To understand and optimize the properties of NWs with axially inserted heterostructures the crystal structure have to be characterised with a high spatial resolution. Conventional TEM techniques are useful for characterising large areas of a NW through SAED and DF imaging. Using HRTEM imaging, also a very high spatial resolution can be achieved for selected areas. The studied structure here is a GaAs NW with an axially inserted heterostructure of GaAsSb. It has an cross-sectional hexagonal shape and is found to be 4 μm long and 133 nm in diameter. Below the GaAsSb insert, the NW is crystallized in the ZB phase and grow in the $[111]_{ZB}$ direction with the $\langle 110 \rangle_{ZB}$ orientations at the facets. From EDS measurements the position and presence of the GaAsSb heterostructure is determined with 15 at.% Sb. At the top of the ZB GaAsSb heterostructure a ZB twin plane is observed before the phase changes to WZ as the NW composition returns to GaAs.For the WZ phase the growth direction is the $[0001]_{WZ}$ and the facets are on the $\langle 1120 \rangle_{WZ}$ orientations. The NW is observed to bend along the length. Through SPED measurements, local diffraction data can be obtained by scanning a small electron probe across the sample to create a stack of DPs. The precession of the beam improve the DPs by giving more visible reflections, makes it more on zone and makes the intensity of the reflections more even. This is beneficial for further processing of the data stack. The SPED measurements provide vast amounts of information which can be extracted through several post-processing routines. When the crystal structure is aligned on the $[1\bar{1}0]_{ZB}$ and $[2\bar{1}\bar{1}0]_{WZ}$ zone axis, differences in the DPs are observed for the ZB and WZ phases and this is good for all studied post-processing. In this case, the SPED measurements can be used to separate the phases through VDF, template matching and unsupervised machine learning (NMF). The area that can be reliably analyzed by these approaches is limited by the bending of the NW.

Studying strain using the conventional techniques of TEM gives an initial qualitative view of the strained region through interpreting the image contrast in BF images. From

these images strain is observed to be present in both the ZB and the WZ GaAs adjacent to the axial GaAsSb insert. SPED measurements has then been utilised to estimate the strain in these segments. Two orientation of the NW are studied, the $[1\bar{1}0]_{ZB}$ (the orientation seen at the hexagonal NW facets) and the $[2\bar{1}\bar{1}]_{ZB}$ (corners of the hexagonal NW). The strain measurements are affected by several parameters in the collection of DPs. It is performed by measuring the change in distance of selected reflections in the DPs from the direct beam. Post-processing allows for a wide choice of reflections are available as the entire DPs are collected in the SPED data. The position of the reflections is determined with a center-of-mass method. In order for this to give good final results, good DPs are important. The focused electron beam used when scanning across the sample in SPED measurements allows for small areas to be probed. This requires a slightly convergent beam resulting in the reflections in the DPs to broaden with an intensity that varies due to dynamical electron diffraction. By precessing the electron beam the reflections get a more constant intensity making the center-of-mass position estimate better. The precession also gives reflections further out in reciprocal space that could be used. In this work two different beam convergence angles are compared for strain measurements where the optimum angle is found to be $\alpha = 1.3$ mrad as even with precession there are intensity variations within the discs which compromise the center-of-mass approach. Another important collection parameter is the camera length as this affect both the field of view in reciprocal space and the pixel size of the reflections in the collected data. Two camera lengths are therefore used for SPED measurements for comparison. The optimal parameters for strain measurements were found to be a small camera length allowing for reflections further out in reciprocal space to be used. Reflections as far out in reciprocal space as possible before the signal to noise ratio becomes too weak are found to be preferred. The best results were obtained with the NW oriented at the $[1\bar{1}0]_{ZB}$ and $[2\bar{1}\bar{1}0]_{WZ}$ zone axis using the $222_{ZB}/0004_{WZ}$ and $22\bar{4}_{ZB}/0\bar{3}30_{WZ}$ reflection.

In conclusion, the possibilities of the post-processing routines on a collected SPED data stack makes the SPED measurements a very useful tool to deduce different crystal characteristics such as phase, orientation and strain across heterostructures within NWs. The collected stacks of DPs can be used to characterise the crystal structure through virtual imaging, template matching and unsupervised machine learning (NMF). It can also be used to distinguish crystal orientation changes, bending and provide qualitative information about strain fields, similar to conventional TEM techniques. Beyond this, the SPED measurements can provide qualitative insight into strain fields, and decompose the strain into normal strains and shear strain making it a valuable addition to a characterization toolbox of the microscopist.

Chapter 7

Future work

7.1 Ideal nanowire strain measurements

Distortions are introduced to the images for the current collection method as the DPs are collected from an inclined flourescent screen. Additional distortions can also be introduced by the projector lens and the external camera position changing between measurements as it is not mounted in a fixed manner. A distortion correction routine is available through the PyXem package using patterns from a polycrystalline Au cross grating. This approach was attempted on the used system, but the collected patterns were not of sufficient quality for the procedure to determine the distortion correction. The current fixed engineering correction within ASTAR was assumed to be sufficient. In the near future a direct detection method will be made available at the TEM Gemini centre for the JEOL JEM 2100F. This will use a CCD camera that is placed at the bottom of the TEM fixed on the optical axis. This will provide higher resolution and signal to noise ratio, and no afterglow as is present for the fluorescent screen. As a result less distortions should be experienced, reflections at higher angles could potentially be used and better measurements are then to be expected. For this reason these measurements would be of interest to perform on this new detector and compare the results to the ones reported here. The NWs investigated also seemed to have a varying degree of bending. Students recently highlited to an enourmous gain in direct electron detectors over the current CCDs and even more so relative to the optical data collection used here [34]. An issue that could arise with this detector is large data size due to the dynamic range that is stored. This could mean that the data processing routines need to be improved to handle these larger data sets.

7.2 Additional convergence angles

In this study two convergence angles were investigated at ~ 1.3 mrad and ~ 3.5 mrad. The smaller convergence angle provide clear reflections with a small radii and the larger provide as large reflections as possible without individual reflections touching. Two problems are experienced for the larger α setting. One is that the WZ reflections when oriented at the $[2\bar{1}\bar{1}00]_{WZ}$ orientation will overlap making the strain measurements for WZ difficult. The other is that the reflections no longer have a uniform intensity distribution making the center of mass position estimate difficult. The largest convergence angle possible which would allow both phases in both orientations to be measured would be $\alpha \approx 1.72$ mrad. This value has been found by requiring the relation between the densest reflection distance b and the reflection radii a to be 0.9 (See Appendix C). With this setting the reflections could still have a uniform intensity while increasing the radii for position determination possibly providing the best α angle setting for GaAs NWs crystallising in both the ZB and WZ phases. This was not performed in this study due to alignment issues for the required TEM setting to achieve this convergence angle.

7.3 Routine characterisation

This work established the best practice to collect and process SPED data stacks for structural characterisation. There are different processing routines but for large bending of the NW the area that can be analysed from one scan is limited. Using flat electron transparent support such as SiN thin films reduce bending and extend areas that can be analysed reliably. Together with the established optimal microscope and detector settings, SPED can become a routine tool for structural analysis of heterostructures in NWs.

7.4 Beyond nanowires

NWs are to some extent a model structure, a well understood 1D object. The complete structural characterisation based on SPED should be extended to specimens of 2D nanostructures (thin films on substrates) for which strain is crucial as well. The imaging, detecting and processing settings could be similar as found in the present study, however the optimal orientations and reflections to be used will likely vary.

Bibliography

[1] E. C. Garnett, M. L. Brongersma, Y. Cui, and M. D. McGehee. Nanowire solar cells. *Annual Review of Materials Research*, 41(1):269–295, 2011.

[2] H. Riel, L. E. Wernersson, M. Hong, and J. A. Del Alamo. III-V compound semiconductor transistors - from planar to nanowire structures. *MRS Bulletin*, 39(8):668–677, 2014.

[3] A. Bao. Group III-nitride nanowires. *Materials Science and Technology (United Kingdom)*, 33(7):765–776, 2017.

[4] J. Singh. *Smart Electronic Materials: Fundamentals and Applications*. Cambridge University Press, 2005.

[5] E. Barrigón, M. Heurlin, Z. Bi, B. Monemar, and L. Samuelson. Synthesis and Applications of III–V Nanowires. *Chemical Reviews*, 119(15):9170–9220, 2019.

[6] J. Svensson, A. W. Dey, D. Jacobsson, and L. Wernersson. Iii–v nanowire complementary metal–oxide semiconductor transistors monolithically integrated on si. *Nano Letters*, 15(12):7898–7904, 2015. PMID: 26595174.

[7] E. Lind, E. Memisevic, A. W. Dey, and L. Wernersson. III-V heterostructure nanowire tunnel FETs. *IEEE Journal of the Electron Devices Society*, 3(3):96–102, 2015.

[8] H. Weman and D. Dheeraj. III-antimonide nanowires. *Advances in III-V Semiconductor Nanowires and Nanodevices*, 89-104, 2011.

[9] M. de la Mata, C. Magén, P. Caroff, and J. Arbiol. Atomic Scale Strain Relaxation in Axial Semiconductor III–V Nanowire Heterostructures. *Nano Letters*, 14(11):6614–6620, 2014.

[10] R. Teissier, D. Sicault, J. C. Harmand, G. Ungaro, G. Le Roux, and L. Largeau. Temperature-dependent valence band offset and band-gap energies of pseudomorphic gaassb on gaas. *Journal of Applied Physics*, 89(10):5473–5477, 2001.

[11] J Todorovic. *Correlated Transmission Electron Microscopy and Micro-photoluminescence Studies of GaAs-based Heterostructured Semiconductor Nanowires*. Phd-thesis, Norges teknisk-naturvitenskapelige universitet (NTNU), Trondheim, 2012.

[12] H. Kauko. *Quantitative scanning transmission electron microscopy studies on heterostructured GaAs nanowires*. Phd-thesis, Norges teknisk-naturvitenskapelige universitet (NTNU), Trondheim, 2013.

[13] I. Robinson and R. Harder. Coherent x-ray diffraction imaging of strain at the nanoscale. *Nature Mater*, 8:291–298, 2009.

[14] D. B. Williams and C. B. Carter. *Transmission electron microscopy*. Springer, 2009.

[15] M.J. Hÿtch, E. Snoeck, and R. Kilaas. Quantitative measurement of displacement and strain fields from hrem micrographs. *Ultramicroscopy*, 74(3):131 – 146, 1998.

[16] D. Cooper, T. Denneulin, N. Bernier, A. Béché, and J. Rouvière. Strain mapping of semiconductor specimens with nm-scale resolution in a transmission electron microscope. *Micron*, 80:145 – 165, 2016.

[17] D. N. Johnstone, A. T. J. van Helvoort, and P. A. Midgley. Nanoscale Strain Tomography by Scanning Precession Electron Diffraction. *Microscopy and Microanalysis*, 23(S1):1710–1711, 2017.

[18] D. N. Johnstone, P. Crout, L Laulainen, S. Høgås, B. Martineau, T. Bergh, S. Smeets, C. Francis, E. Opheim, E. Prestat, S. Collins, M. Danaie, T. Furnival, H. W. Ånes, J. Morzy, A. Iqbal, T. Doherty, M. von Lany, T. Ostasevicius, R. Tovey, E. Jacobsen, and T. Poon. pyxem/pyxem: pyxem v0.11.0, May 2020. `https://doi.org/10.5281/zenodo.3831473`.

[19] C. Kittel. *Introduction to Solid State Physics*. John Wiley & Sons Inc, 8th editio edition, 2005.

[20] F. C. Frank. On Miller–Bravais indices and four-dimensional vectors. *Acta Crystallographica*, 18(5):862–866, 1965.

[21] R. S. Wagner and W. C. Ellis. Vapor-Liquid-Solid Mechanism of Single Crystal Growth. *Applied Physics Letters*, 4(5):89–90, 1964.

[22] A. Chowdhury and A. Misra. Nanostructure growth using VLS methods. 1-30, 2010.

[23] J. Harmand and et al. Atomic step flow on a nanofacet. *Phys. Rev. Lett.*, 121:166101, Oct 2018.

[24] D. V. Lang, H. G. Grimmeiss, E. Meijer, and M. Jaros. Complex nature of gold-related deep levels in silicon. *Physical Review B*, 22(8):3917–3934, 1980.

[25] Lattice Imaging in Transmission Electron Microscopy. *Materials Structure*, 8(1):3–16, 2001.

[26] J. S. Barnard, D. N. Johnstone, and P. A. Midgley. High-resolution scanning precession electron diffraction: Alignment and spatial resolution. *Ultramicroscopy*, 174(December 2016):79–88, 2017.

[27] P. Hoyer. Non-negative matrix factorization with sparseness constraints. *Journal of Machine Learning Research*, 5:1457–1469, 2004.

[28] D. D. Lee and H. S. Seung. Learning the parts of objects by non-negative matrix factorization. *Nature*, 401(6755):788–791, 1999.

[29] K. Momma and F. Izumi. *VESTA3* for three-dimensional visualization of crystal, volumetric and morphology data. *Journal of Applied Crystallography*, 44(6):1272–1276, 2011.

[30] Yusuke Seto. Recipro, v4.778, 2020. `https://github.com/seto77/ReciPro/releases/tag/v.4.778`.

[31] B. Martineau, D. Johnstone, A.T.J. Helvoort, P. Midgley, and A. Eggeman. Unsupervised machine learning applied to scanning precession electron diffraction data. *Advanced Structural and Chemical Imaging*, 5, 12 2019.

[32] S. Conesa-Boj and et al. Plastic and Elastic Strain Fields in GaAs/Si Core–Shell Nanowires. *Nano Letters*.

[33] A. Denton and N. Ashcroft. Vegard's law. *Phys. Rev. A*, 43:3161–3164, 03 1991.

[34] M. Nord, R. W. H. Webster, K. A. Paton, S. McVitie, D. McGrouther, I. MacLaren, and G. W. Paterson. Fast Pixelated Detectors in Scanning Transmission Electron Microscopy. Part I: Data Acquisition, Live Processing and Storage. 1-16, 2019.

Appendix

A Scan step calibration

For the calibrations of the SPED scanning steps and pixel width in the viewing screen a poly-crystalline Au cross grid as depicted in Figure A1 has been used. This grid is supplied from Ted Pella Inc. and is originally intended for calibration of the microscope magnification. The distance between the lines on the grid is 463 nm.

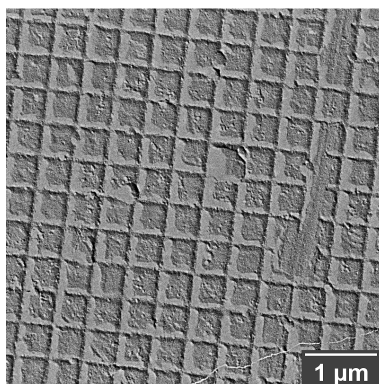

Figure A1: TEM image of a Au cross grid supplied by Ted Pella Inc.

As explained in chapter 2.15 the SPED measurements are done by scanning the sample with a small probe to create a map of DPs for each point on the sample. To calibrate the true size of the steps taken in the TEM two methods has been used in this thesis. The first method is to use the Au cross grid. A SPED scan is performed of the sample for a sufficiently large area to preferably cover multiple squares. A VDF image from a 200 by 200 SPED scan of the Au cross grid can be seen in Figure A2a. From this VDF the number of pixels, or steps, per square can be found. Combining this with the given Au square width of 463 nm allows for the $^{nm}/_{step}$ ratio to be determined. However this method is limited to larger scans as at least 1 square must be covered to get a calibration and using more squares will reduce the error.

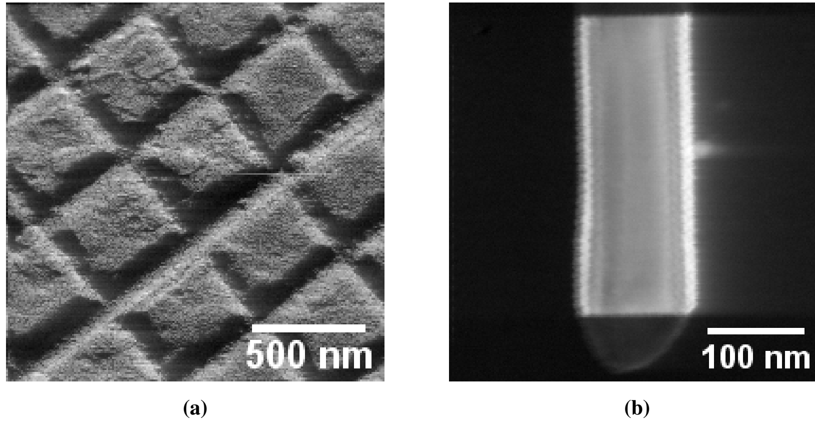

Figure A2: VDF images from a SPED scan of (a) the Au cross grating and (b) a GaAs NW in the ZB phase with a twin region.

Table 1: Scan step sizes. Step number 2 is obtained from SPED scan of NW feature, others from Au cross grid measurements.

Step number [#]	Software size [nm]	True size [nm]
2	1.28	1.69
10	6.4	8.3
20	12.8	16.54
50	32	41.7

To calibrate smaller step sizes a very large scan would be required for the Au cross grid to cover multiple squares. A better solution is to use a feature on a sample which it is possible to determine the exact length of from HRTEM imaging. This can be done on the NWs studied here by finding a twin region of appropriate size and take both a HRTEM and a SPED scan over the entire twin region. In Figure A2b a 300 by 300 SPED scan of a twin region in a GaAs NW can be seen. From a HRTEM, of the same region, the length of the twin can be found by scaling the image from the known d_{111} spacing of GaAs (as was found for the HRTEM image in Figure 4.12a). The length of the twin in terms of pixels, or steps, in the SPED scan can be found with a line trace. It is then possible to determine the step size of the SPED scan. Table 1 shows the values found for four different chosen step sizes in the TEM.

B SPED diffraction calibration

The scale of DPs taken at a camera length of about 19.65cm using SPED techniques has been found using two different methods. One is to use the diffraction pattern from a ZB region oriented at zone axis $[1\bar{1}0]_{ZB}$. The distance to a 111_{ZB} reflection was found to be

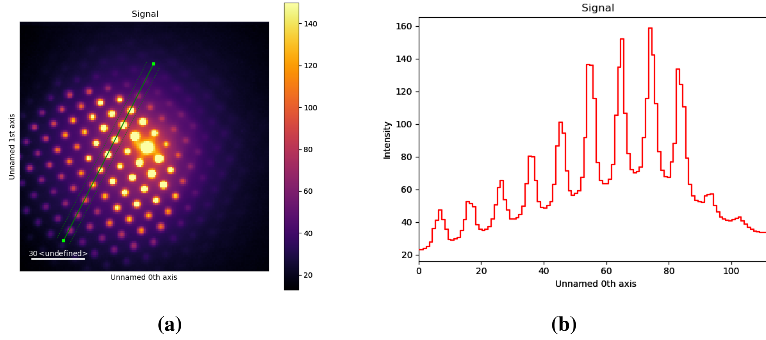

(a) (b)

Figure A3: (a) DP of $[1\bar{1}0]_{ZB}$ used for calibration of scale and (b) a line trace from the DP in (a).

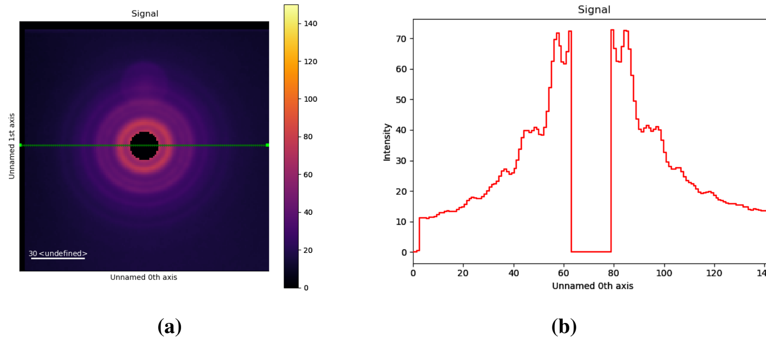

(a) (b)

Figure A4: (a) DP of poly-crystalline Au used for calibration of scale and (b) a line trace from the DP in (a). A mask has been applied to the central beam.

9.6 ± 0.2 pixels in the image giving a calibration value of 0.0319 ± 0.0007 Å^{-1}/pixel. The measurement used for this calibration is displayed in FigureA4. The same procedure was performed for a camera length of 60 cm where the resolution was found to be 0.011 Å^{-1}/pixel.

The other method was to use DP rings of a Au cross grating. The Au crystallises in the diamond structure. This means that the five closest kinematically allowed scatterings are from the $\{111\}$, $\{002\}$, $\{022\}$, $\{113\}$ and $\{222\}$ planes. By measuring the distance to the closest rings, a calibration for the DP can be found by comparison to the calculated value using (2.11). The measurements taken for this procedure is displayed in Figure A4. Some care should be taken when analysing this data however. Due to the resolution of the camera used to acquire the DP some rings overlap. This happens for the $\{111\}$ and $\{002\}$ planes which have a distance in the reciprocal space of about 0.066 Å^{-1}. For the resolution found from the GaAs NW of 0.0319 Å^{-1}/pixel this would mean that the distance between the two peaks is about two pixels. As the width of the peaks is about three pixels this becomes indistinguishable. The same problem is encountered for the $\{311\}$ and $\{222\}$ peaks which are even closer in reciprocal space. The $\{002\}$ and $\{222\}$ reflections are not kinematically

allowed for the Au diamond structure, but due to dynamical effects these reflections are still detectable.

C Convergence angle (α) calibration

As explained in section 2.15 the electron beam used in SPED measurements is not parallel but has a convergence angle α as seen in Figure A5. The value of the convergence angle

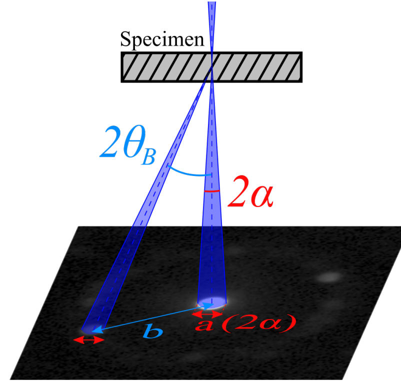

Figure A5: The electron beam on the sample is focused with some convergence angle α affecting the reflection width a in the DP. This width together with the spacing b between reflections allows for α to be determined.

can be found from measuring the width, a, of the diffraction spots in the DP and the distances, b, between the spots and using the following equation

$$2\alpha = 2\theta_B \frac{a}{b}. \quad (1)$$

Doing these measurements at a high camera length is convenient as it makes determining the width of the DP spots easier. For my calculations a camera length of 60 cm was used and a DP from an unstrained GaAs region of the studied NWs. The electrons in the TEM have been accelerated using a voltage of 200 kV which results in electrons with a wavelength of $\lambda_{e^-}^{200keV} \approx 2.5079$ pm. Using Braggs law 2.20 the value of θ_B can be found mathematically for a given reflection. The measurements taken in this thesis used two different convergence angles with the TEM using a spot size of 1 nm and an alpha setting of $\alpha_{software\#} = 3$ for both, and the condenser aperture changed between them for two different angles. Using the smallest condenser aperture available resulted in a DP as seen in Figure A6a for which the convergence angle was found to be $\alpha_1 = 1.3 \pm 0.3$ mrad. The next smallest condenser aperture was used for the other setting yielding $\alpha_2 = 3.5 \pm 0.3$ mrad. The DP seen for α_2 is presented in Figure A6b. For the measurements presented here the condenser mini lens was put in setting number 3. This could be changed to alter the convergence angle, but changing the condenser mini lens affects the SPED alignments and was therefore avoided. A small python script for determining the required α to achieve

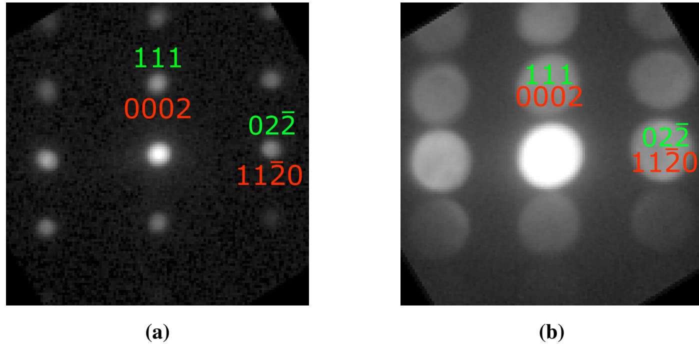

Figure A6: DPs seen at the $[2\bar{1}\bar{1}]$ and $[01\bar{1}0]$ zone axis for convergence angles. Indexing for ZB is green and indexing for WZ is red. (a) α_1 and (b) α_2. These images have been acquired from the TEM viewing screen using the StingRay camera whilst in precession mode

a desired $^a/_b$ ratio, or a required ratio for a desired α, has been made and can be seen in Appendix J.

D Precession angle (ϕ) calibration

The calibration of the precession angle can be done by turning off the descan during measurements of vacuum or a low scattering region. This will make the direct beam create a circle due to the precession. Figure A7 shows a schematic of the beam trajectory from the sample, or eucentric height, to the viewing screen. From somple trignonometric consider-

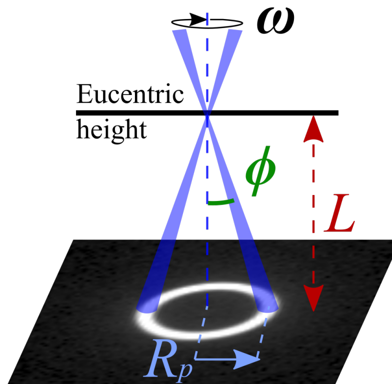

Figure A7: If the electron beam is passed through vacuum and precessed with a precession angle $\phi > 0$ and no descan, the resulting DP seen on the viewing screen is a circle with some radius R_g depending on the camera length L and precession angle ϕ.

ations it can be seen that the precession angle can be found by the following equation

$$\tan\phi = \frac{R_p}{L}, \tag{2}$$

where R_p is the radius of the precessed circle on the viewing screen, L is the camera length and ϕ is the precession angle. Figure A7 shows the DP of a precessed beam with a camera length of $L = 20$ cm. This has been precessed an amount of $0.7°$ in the SPED software on the TEM and this is the amount that has been used in all the SPED measurements described in this thesis. It was found that $R_p = 2.2$ mm on the viewing screen, which results in a value for the precession of $\phi \approx 0.64° = 11.2$ mrad. It should be mentioned that this measurement depends on both the camera length and the pixel width calibration described in sections E and F. Both has been re-calibrated as best as possible.

E Camera length calibration

When studying materials in the TEM it is important to know the instruments camera length. Figure A8 presents a schematic of the relationship between the camera length

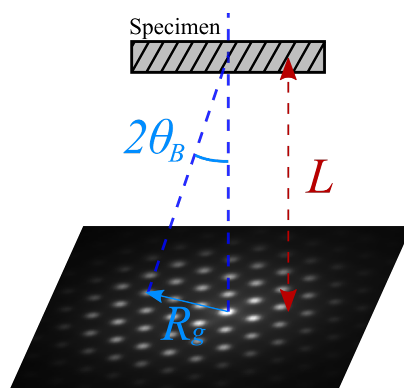

Figure A8: A DP can be seen from a GaAs NW with the ZB phase. The distance R_g to a specific spot in the DP together with the Bragg angle θ_B can be used to determine the effective camera length through (3).

L and the distances on the viewing screen. From trigonometric considerations of the figure it can be seen that $R = L\tan(2\theta_B)$. And from Braggs equation (section 2.8) we know that $\lambda = 2d\sin(\theta_B)$. Since the angle θ_B is very small, we can approximate $\tan(2\theta_B) \approx 2\theta_B \approx 2\sin(\theta_B)$. Using these equations the camera length can be found as

$$L = \frac{R_g d}{\lambda}. \tag{3}$$

Using a known material the value of θ_B can be calculated, the wavelength for an electron with kinetic energy of 200 keV can be calculated and the distance R_g to a reflection is measured on the viewing screen.

For my measurements of GaAs NWs a camera length on the TEM of $L = 20$ cm has been chosen on the machine. From my own calibrations the true value of the camera length on the viewing screen, in SPED mode, was found to be $L = 19.65$ cm.

F SPED camera pixel width calibration

For the calibration of the camera length and precession angle it is important to be able to measure the distances on the viewing screen. The DP collection in SPED measurements is performed indirectly by imaging the fluorescent screen with a camera outside the TEM. The camera used is a StingRay with a setting to collect images with a resolution of 144 by 144. The pixel width cannot be directly interpreted as for a direct collection with a CCD camera inside the TEM. In this case the pixel width of the camera on the fluorescent screen needs to be found. For this a Au cross grid sample has been used as described in Appendix A. In Figure A9 an image taken with the SPED camera is superimposed on an

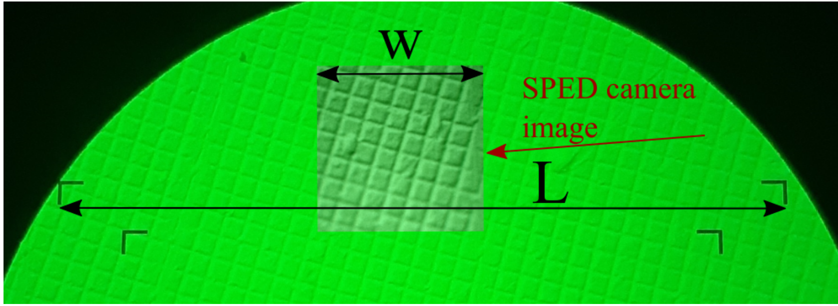

Figure A9: Image of the Au cross grid taken by the SPED camera superimposed on the same view as seen from outside the TEM. Relating the distances labelled w and L in the image allows for an estimate of the mm/pixel value of the SPED camera.

image of the viewing screen and scaled to the same magnification. The real width w_{real} of the image on the viewing screen can be found as

$$w_{real} = \frac{w}{L} \cdot L_{real}, \tag{4}$$

where L_{real} is the length of L on the viewing screen. This means that the width of a pixel in the SPED camera images is

$$\frac{mm}{pixel} = \frac{w_{real}}{w_{pixels}}. \tag{5}$$

For the instrument used this was found to be ${}^{mm}/_{pixel} \approx 0.157$.

G Fast Fourier transform of high-resolution TEM images

As described in the theory section the reciprocal crystal space of a periodic material is connected to the real space crystal. This connection can be utilised to present the result in both real and reciprocal space by taking the FFT of an observed crystal structure in the HRTEM which essentially brings the observed two-dimensional real lattice lattice to the Fourier space. The result is an image with intensities at specific distances in the Fourier space depending on the spacial frequency seen in the HRTEM. This process then creates a pattern similar to the DP one would see for the same region. Figure A10 shows this case for the HRTEM image taken of the insert region in the studied NW. This can in some cases help to visualise weak lattice fringes.

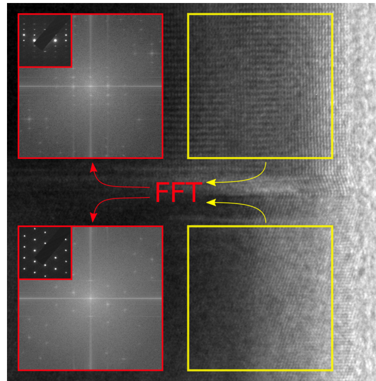

Figure A10: FFTs have been performed on each side from the phase change from inside the yellow squares. The results are patterns with the same symmetry relations as would be observed from DP created from the same regions in a TEM as seen in the upper left corner of the FFTs for reference.

H Crystal orientation from Ewald sphere considerations

As mentioned in section 2.8 the observed DP for a crystal structure can be conveniently described by the intersection between the Ewald sphere and the reciprocal crystal space. When the crystal is oriented perfectly on a low index zone the DP is symmetric around the central beam where the Ewald sphere cuts out a 2D plane around the central beam in the ZOLZ. But when the crystal is tilted off the zone axis, the Ewald sphere is tilted relative to the ZOLZ and the observed intensities are located around a circle in the reciprocal space whose centre is shifted from the central beam by a distance d depending on the specimen tilt. Figure A11 demonstrates this for an angle between the incoming beam and the zone axis of θ.

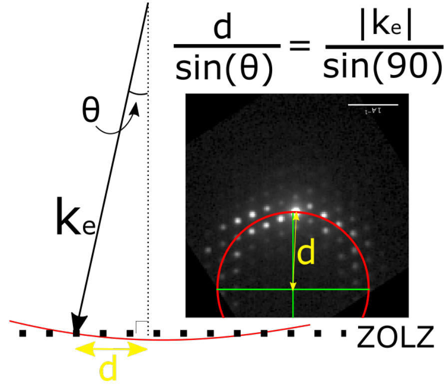

Figure A11: When the Ewald sphere is tilted in reciprocal space it intersects the ZOLZ in a circle displaced a distance d from the central beam.

Simple geometric considerations together with the law of sines gives a relation between the tilt angle θ and the distance d as

$$\sin(\theta) = \frac{d}{|\mathbf{k_e}|}, \tag{6}$$

where $\mathbf{k_e}$ is the wave vector of the electron beam. This allows for the off zone tilt to be estimated by fitting an Ewald circle in the observed experimental DPs.

I Additional strain maps

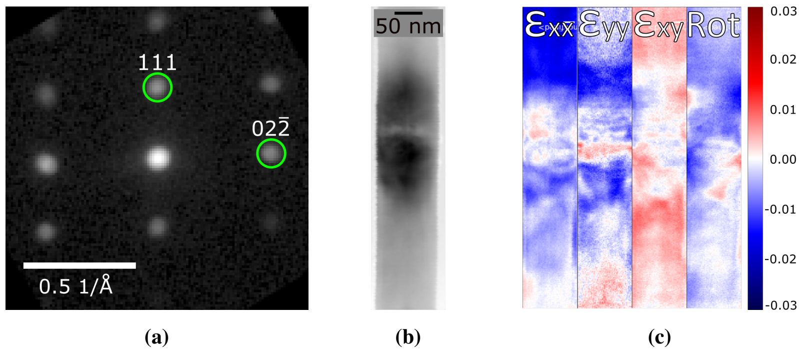

Figure A12: (a) DP obtained for NW oriented at $[2\bar{1}\bar{1}]_{ZB}$ and $[1\bar{1}00]_{WZ}$, camera length of 60 cm and $\alpha \approx 1.3$ mrad together with marked reflections used for strain mapping. (b) VBF image of strained region. (c) Strain and rotation maps from reflections marked in (a), strain is given as relative change in reflection distance and rotation is given in radians.

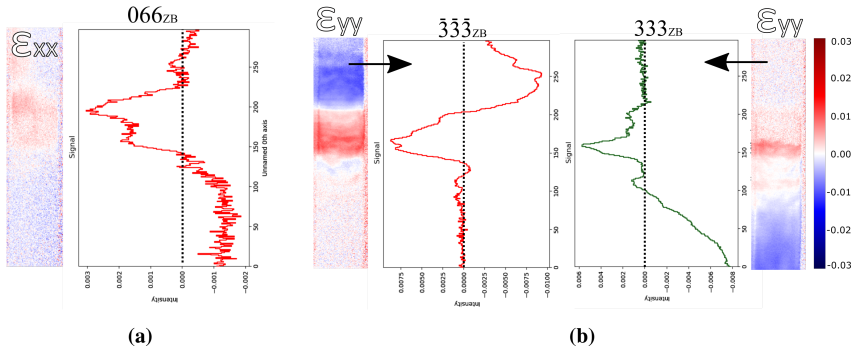

Figure A13: Strain measurements from $[2\bar{1}\bar{1}]_{ZB}$ zone, camera length 20 cm (a) ϵ_{xx} using 066_{ZB} reflection and (b) ϵ_{yy} using 333_{ZB} and $\bar{3}\bar{3}\bar{3}_{ZB}$.

J Code for convergence angle determination

Using the highest possible camera length which would include a desired reflection is calculated here to maximize reflection size in SPED DPs.

```
import numpy as np

################################
### ------ Parameters ------ ###
################################

a_ZB      = 5.65325       #A, GaAs
a_WZ      = 3.989         #A, GaAs
c_WZ      = 6.564         #A, GaAs

a_Au      = 4.065         #A, Au
L_w       = 0.025079      #A

to_rad    = np.pi/180
to_deg    = to_rad**-1

################################
### -------- Funcs -------- ####
################################

def dist_cubic(A, a):              # |d_hkl| for cubic
   h, k, l = A[0], A[1], A[2]
   d_inv = (h**2 + k**2 + l**2)/a**2
   return np.sqrt(d_inv**(-1))
```

```
def dist_hcp(A, a, c):           # |d_hkil| for hcp
   # A    : d_hkl as list [h,k,i,l]
   # a, c : lattice parameter (WZ)
   h, k, i, l = A[0], A[1], A[2], A[3]
   d_inv = (4/3)*(h**2 + h*k + k**2)/(a**2) + (l/c)**2
   return np.sqrt(d_inv**(-1))

def theta_B_d(d):                # Bragg angle for d_hkl,
    d=|d_hkl|
   # d    : |d_hkl|
   return np.arcsin(L_w/(2*d))*to_deg

def alpha_from_ratio(ratio, a, refl):
   # ratio : |d_hkl|/(reflection radii)
   # a     : lattice parameter (ZB/WZ)
   # refl  : d_hkl as list [h,k,l]/[h,k,i,l]
   if (a == a_WZ):
      result = ratio*theta_B_d(dist_hcp(refl, a, c_WZ))
   else:
      result = ratio*theta_B_d(dist_cubic(refl, a))
   return result

def ratio_from_alpha_mrad(alpha, a, refl): # Result given in mrad
   # alpha : desired alpha in deg
   # a     : lattice parameter (ZB/WZ)
   # refl  : d_hkl as list [h,k,l]/[h,k,i,l]
   if (a == a_WZ):
      result = alpha/(theta_B_d(dist_hcp(refl, a,
          c_WZ))*to_rad*1000)
   else:
      result = alpha/(theta_B_d(dist_cubic(refl, a))*to_rad*1000)
   return result

def ratio_from_alpha_deg(alpha, a, refl): # Result given in
    degrees
   # alpha : desired alpha in mrad
   # a     : lattice parameter (ZB/WZ)
   # refl  : d_hkl as list [h,k,l]/[h,k,i,l]
   if (a == a_WZ):
      result = alpha/(theta_B_d(dist_hcp(refl, a, c_WZ)))
   else:
      result = alpha/(theta_B_d(dist_cubic(refl, a)))
   return result

################################
### ------ Changeable ------ ####
################################

refl     = [0,0,0,1]      # [111] spot used as closest spot in DP
ratio    = 0.9            # ratio between a/b =
```

```
    spot_diameter/dist_to_spot

alpha_deg = alpha_from_ratio(ratio, a_WZ, refl)
alpha_rad = alpha_deg*to_rad*1000

print("For a ratio of a/b =","%.3f" % ratio, "you need alpha =",
    "%.5f" % alpha_deg+" =","%.5f" % alpha_rad,"mrad.")
```

K Code for determining camera length for desired reflection

```
import numpy as np

################################
### ------ Parameters ------ ###
################################

a_ZB      = 5.65325      #A, GaAs
a_WZ      = 3.989        #A, GaAs
c         = 6.564        #A, GaAs
a_Au      = 4.065        #A, Au
L_w       = 0.025079     #A, wavelength electron 200keV

to_rad    = np.pi/180
to_deg    = to_rad**-1

cam_w     = 144          # pixel width of camera view
mm_px     = 0.157        # mm/pixel on viewing screen

safety    = 0.8          # safety multiplied with calc L to ensure
    enitre spot in DP

################################
### -------- Funcs -------- ####
################################

def dist_cubic(A):
   h, k, l = A[0], A[1], A[2]
   d_inv = (h**2 + k**2 + l**2)/a_ZB**2
   return np.sqrt(d_inv**(-1))

def dist_hcp(A):
   h, k, i, l = A[0], A[1], A[2], A[3]
   d_inv = (4/3)*(h**2 + h*k + k**2)/(a_WZ**2) + (l/c)**2
   return np.sqrt(d_inv**(-1))

def theta_B_d(d):
```

```
    return np.arcsin(L_w/(2*d))*to_deg

def camera_length_to_reach_d(d):
    R = (cam_w/2 * mm_px*10**-3)
    return (R*d/L_w)*10**2                # returns camera length in
        cm

def camera_length_to_reach_d_plus(hkl):
    hkl = np.array(hkl)
    if (hkl.size==3):
        d_hkl = dist_cubic(hkl)
        d_2hkl= dist_cubic(hkl*2)
    else:
        d_hkl = dist_hcp(hkl)
        d_2hkl= dist_hcp(hkl*2)

    f = camera_length_to_reach_d(d_hkl)
    g = camera_length_to_reach_d(d_2hkl)
    return f-g/2                  # returns camera length in cm

def print_info_reflection(hkl):
    has_neg = False
    hkl = np.array(hkl)
    if(hkl.size==3):
        if (hkl[0] < 0 or hkl[1] < 0 or hkl[2] < 0):
            has_neg = True
        d_hkl = dist_cubic(hkl)
    else:
        if (hkl[0] < 0 or hkl[1] < 0 or hkl[2] < 0 or hkl[3] < 0):
            has_neg = True
        d_hkl = dist_hcp(hkl)

    L      = camera_length_to_reach_d(d_hkl)
    L_ratio = L*safety
    A_px   = d_hkl**-1/(cam_w/2)

    print('#============================================================#')
    if (hkl.size==3 and has_neg):
        print('#',hkl, "\t -> max cam length \t=","%.4f" %
            L,"cm\t\t\t#")
    elif (hkl.size==3 and not has_neg):
        print('#',hkl, "\t -> max cam length \t\t=","%.4f" %
            L,"cm\t\t\t#")
    elif (hkl.size==4 and has_neg):
        print('#',hkl, " -> max cam length \t=","%.4f" %
            L,"cm\t\t\t#")
    else:
        print('#',hkl, " -> max cam length \t\t=","%.4f" %
            L,"cm\t\t\t#")
    print("# This gives a resolution of \t\t~","%.5f" % A_px,
```

```
    "(A*pixel)^-1\t#")
  print("# Camera length *", safety, "\t\t\t\t=","%.4f" %
      L_ratio,"cm \t\t\t#")
  print('#============================================================#')

################################
### ------ Changable ------ ####
################################

list = np.asarray([[2,2,4], [0,4,4]])#, [0,0,0,4], [1,1,-2,0],
    [2,2,-4,0]])
for reflection in list:
  print_info_reflection(reflection)
```

L Code for pre processing SPED data

```
%matplotlib qt
import pyxem as pxm
import numpy as np
import hyperspy.api as hs
from matplotlib import pyplot as plt

file =' ./torit_NW2_300x300-2_L20_A3_AP3_x_y_z_tx_ty_20ms.hdf5'
NW_crop = pxm.roi.RectangularROI(left=138, top=0, right=210,
    bottom=300)
print('Now using: ', file.split('\\')[-1][0:31])

save_hdf5 = False

# Upload file and plot:
dp = pxm.load(file)
dp.set_signal_type('electron_diffraction')
dp.metadata.set_item("General.title", file.split('\\')[-1][20:30])
dp.set_scan_calibration(1)

dp.plot()

# Crop data and do pre-processing:
NW = NW_crop(dp)
theta     = np.deg2rad(-31)
R         = np.asarray([[ np.cos(theta), -np.sin(theta), 0],
                    [ np.sin(theta), np.cos(theta), 0],
                    [          0,            0, 1]])
NW.apply_affine_transformation(R, preserve_range=True)

if (True):
```

```
    NW.center_direct_beam(method='cross_correlate',
                          radius_start=2,
                          radius_finish=10,
                          half_square_width=10)
if (True):
    NW = NW.remove_background('gaussian_difference',
                              sigma_min=2, sigma_max=8)
    NW.data -= NW.data.min()
    NW.data *= 1 / NW.data.max()

NW.set_diffraction_calibration(0.032)
NW.plot()

# Save pre processed file:
save_dir = file[0:-5] + '_preProcessA.hdf5'
save_hdf5 = True
if (save_hdf5):
    NW.save(save_dir)
    print('Pre processed NW saved to ' + save_dir)
else:
    print('Pre processed NW will be saved to ' + save_dir)
```

M Code for crystal characterisation

```
file =
    './torit_NW2_300x300-2_L20_A3_AP3_x_y_z_tx_ty_20ms_preProcessA.hdf5'
print('Now using: ', file.split('\\')[-1][0:30])

NMF      = False
template = False
VDF      = False

# Collection parameters:
alpha1 = 1.3 # mrad
alpha2 = 3.85 # mrad

recip_60 = 0.011 # A^-1/px
recip_20 = 0.032 # A^-1/px

scan_2 = 1.69 # nm/px
scan_10 = 8.3 # nm/px

accelerating_voltage = 200 # keV

# Setting important variables from filename:
camL  = int(file.split('_')[-10][1:3])
```

```
expT  = np.int(file.split('_')[-2][0:2])
alpha = file.split('_')[-9]+file.split('_')[-8]
step  = np.int(file.split('-')[1].split('_')[0])

intensity = expT*10

if (alpha == 'A3AP3'):
   alpha = alpha2
elif (alpha == 'A3AP4'):
   alpha = alpha1
else:
   alpha = 0
   print('UNKNOWN ALPHA')

if (camL == 60):
   recip_cal = recip_60 # A^-1/px
elif (camL == 20):
   recip_cal = recip_20 # A^-1/px

if (step == 2):
   scan_cal = scan_2 # nm/px
elif (step == 10):
   scan_cal = scan_10 # nm/px

print('camL =', camL, '; expT =', expT, '; alpha =', alpha, ';
    recip_cal =', recip_cal, '; scan_cal =', scan_cal)

#Upload files:
NW = pxm.load(file)
NW.set_signal_type('electron_diffraction')
NW.set_experimental_parameters(beam_energy = accelerating_voltage,
                              exposure_time    = expT,
                              camera_length    = camL,
                              convergence_angle = alpha,
                              rocking_frequency = 100,
                              rocking_angle    = 11.2)
NW.metadata.set_item("General.title", file.split('\\')[-1][20:30])
NW.metadata

NW.set_scan_calibration(scan_cal)
NW.set_diffraction_calibration(recip_cal)
NW.data = NW.data.astype('float64')

NW.plot()

#NMF:
if (NMF):
   NW.decomposition(True, algorithm='nmf', output_dimension=5)
   NW.plot_decomposition_results()
```

```
#VDF:
g_000 = np.asarray([ 0.00, 0.00]) # A^-1
g_111 = np.asarray([ 0.03,-0.32]) # A^-1
g_220 = np.asarray([ 0.32,-0.44]) # A^-1
g_002 = np.asarray([ 0.32, 0.18]) # A^-1
g_022 = np.asarray([ 0.50,-0.01]) # A^-1
g_0001= np.asarray([ 0.03,-0.15]) # A^-1

g_111l= np.asarray([-0.29,-0.23]) # A^-1 for twin section

g_hkl = g_0001            # reflection used for VDF
if (VDF):
   roi = pxm.roi.CircleROI(cx=g_hkl[0],cy=g_hkl[1], r_inner=0,
       r=0.05)
   NW.plot_integrated_intensity(roi)

# Template matching:
if (template):
   import diffpy

   from diffsims.libraries.structure_library import
       StructureLibrary
   from diffsims.generators.diffraction_generator import
       DiffractionGenerator
   from diffsims.generators.library_generator import
       DiffractionLibraryGenerator

   from diffsims.generators.zap_map_generator import
       get_rotation_from_z_to_direction
   from diffsims.generators.rotation_list_generators import
       get_grid_around_beam_direction

   from pyxem.generators.indexation_generator import
       IndexationGenerator

   diffraction_calibration = recip_cal

   structure_zb =
       diffpy.structure.loadStructure('./GaAs_mp-2534_conventional_standard.cif'
   structure_wz =
       diffpy.structure.loadStructure('./GaAs_mp-8883_conventional_standard.cif'

   za110c = get_rotation_from_z_to_direction(structure_zb,
       [-1,1,0])
   rot_list_cubic =
       get_grid_around_beam_direction(beam_rotation=za110c,
       resolution=1, angular_range=(0,180))

   za110h = get_rotation_from_z_to_direction(structure_wz,
       [1,0,0])
```

```
rot_list_hex =
    get_grid_around_beam_direction(beam_rotation=za110h,
    resolution=1, angular_range=(0,180))

struc_lib = StructureLibrary(['ZB','WZ'],
    [structure_zb,structure_wz], [rot_list_cubic,rot_list_hex])


diff_gen =
    DiffractionGenerator(accelerating_voltage=accelerating_voltage,
    max_excitation_error=1/8)

lib_gen = DiffractionLibraryGenerator(diff_gen)

target_pattern_dimension_pixels =
    NW.axes_manager.signal_shape[0]
half_size = target_pattern_dimension_pixels // 2
reciprocal_radius = recip_cal*(half_size - 1)

# create diffraction library and save:
if (True):
   diff_lib = lib_gen.get_diffraction_library(struc_lib,
                                          calibration=diffraction_calibration,
                                          reciprocal_radius=reciprocal_radius,
                                          half_shape=(half_size,
                                              half_size),
                                          with_direct_beam=False)

   diff_lib.pickle_library('./GaAs_cubic_hex.pickle') #saving
else: # Or upload saved library
   from diffsims.libraries.diffraction_library import
       load_DiffractionLibrary

   diff_lib =
       load_DiffractionLibrary('./GaAs_cubic_hex.pickle',
       safety=True)

indexer = IndexationGenerator(NW, diff_lib)
indexation_results = indexer.correlate(n_largest=3)

crystal_map = indexation_results.get_crystallographic_map()

crystal_map.get_phase_map().plot()

crystal_map.get_orientation_map().plot(cmap='viridis')

indexation_results.plot_best_matching_results_on_signal(NW,
    diff_lib, diff_gen, reciprocal_radius)
```

N Code for strain mapping

```
# For external figs:
%matplotlib qt
# div packages:
import pyxem as pxm
import numpy as np
import hyperspy.api as hs
from matplotlib import pyplot as plt
# For strain map:
from pyxem.generators.subpixelrefinement_generator import
    SubpixelrefinementGenerator
from pyxem.signals.tensor_field import *
from pyxem.generators.displacement_gradient_tensor_generator
    import *

NW2 =
np.asarray(['./torit_NW2_300x300-2_L20_A3_AP3_x_y_z_tx_ty_20ms_preProcessA.hdf5',
         './torit_NW2_300x300-2_L20_A3_AP4_x_y_z_tx_ty_20ms_preProcessA.hdf5'])

# Set true if named as in NW2 list to automatically set
    parameters:
used_naming_convention = True

# Select file if more in NW2 list...
use_index = 1
file = NW2_bottom[use_index]

# Printing selected filnename:
if (used_naming_convention):
   print('Now using: ', file.split('\\')[-1][0:30])
else:
   print('Now using: ', file)

# Collection parameters:
alpha1 = 1.3 # mrad
alpha2 = 3.5 # mrad

recip_60 = 0.011 # ^-1/px
recip_20 = 0.032 # ^-1/px

scan_2 = 1.69 # nm/px
scan_10 = 8.3 # nm/px

# Setting important parameters from filename:
if (used_naming_convention):
   #Setting parameters from filename:
   camL     = int(file.split('_')[-10][1:3])
```

```
    expT      = np.int(file.split('_')[-2][0:2])
    alpha     = file.split('_')[-9]+file.split('_')[-8]
    step      = np.int(file.split('-')[1].split('_')[0])
    intensity = expT*10

    #Setting alpha value from filename:
    if (alpha == 'A3AP3'):
        alpha = alpha2
    elif (alpha == 'A3AP4'):
        alpha = alpha1
    else:
        alpha = 0
        print('!!!UNKNOWN ALPHA!!!')
    #Setting scan and DP calibration from filename:
    if (camL == 60):
        recip_cal = recip_60 # ^-1/px
    elif (camL == 20):
        recip_cal = recip_20 # ^-1/px
    if (step == 2):
        scan_cal = scan_2 # nm/px
    elif (step == 10):
        scan_cal = scan_10 # nm/px

else:
    camL    = 20
    expT    = 10
    alpha   = alpha1
    recip_cal = recip_20
    scan_cal = scan_2

# Print values to double check if things are correct...
print('camL =', camL, '; expT =', expT, '; alpha =', alpha, ';
    recip_cal =', recip_cal, '; scan_cal =', scan_cal)

# Upload file and set calibration:
NW = pxm.load(file)
NW.set_signal_type('electron_diffraction')
NW.set_experimental_parameters(beam_energy = 200.,
                        exposure_time    = expT,
                        camera_length    = camL,
                        convergence_angle = alpha,
                        rocking_frequency = 100,
                        rocking_angle    = 11.2)
NW.metadata.set_item("General.title", file.split('\\')[-1][20:30])
#print(NW.metadata)

NW.set_scan_calibration(1) # Easier to crop with pixel dimensions
print(recip_cal)      # I like printing stuff for checking...
NW.set_diffraction_calibration(recip_cal)
NW.plot()
```

```
#Find unstrained reference DP:
if (camL == 20):
   if (alpha == alpha1):
      ref_reg = pxm.roi.RectangularROI(left=150, top=10,
          right=170, bottom=30)
   elif (alpha == alpha2):
      ref_reg = pxm.roi.RectangularROI(left=160, top=10,
          right=180, bottom=30)
elif (camL == 60):
   if (alpha == alpha1):
      ref_reg = pxm.roi.RectangularROI(left=150, top=10,
          right=170, bottom=30)
   if (alpha == alpha2):
      ref_reg = pxm.roi.RectangularROI(left=150, top=10,
          right=170, bottom=30)

ref_dp = ref_reg(NW)
ref_dpm = ref_dp.mean((0,1)) # take mean of region
ref_reg.add_widget(NW) # add in scan green square
ref_dpm.plot(vmax=intensity)

# DP reflections: (Approximate positions)
# y:
g_111 = np.asarray([0., 0.3])
g_222 = np.asarray([0., 0.63])
g_333 = np.asarray([0., 0.93])
g_444 = np.asarray([0.02, 1.24])
# x:
g_022 = np.asarray([ -0.5, 0.]) #02-1
g_044 = g_022*2
g_066 = np.asarray([-1.52, 0.])
#[110]:
g_224 = np.asarray([-0.88, 0.0]) #22-4/03-30
g_448 = np.asarray([-1.77, 0.0])

# Finding strain:
#Choose refelctions to use:
y_peak = g_333  # [211]
x_peak = g_066
if (use_index == 8):
   y_peak = g_333 # [110]
   x_peak = g_224

# Determine pixel width of reflection from camera length:
if (camL == 20):
   if (alpha == alpha1):
      reflection_px_width = 6 # width of reflection in pixels
   elif (alpha == alpha2):
      reflection_px_width = 12 # width of reflection in pixels
```

```
elif (camL == 60):
   if (alpha == alpha1):
      reflection_px_width = 12 # width of reflection in pixels
   if (alpha == alpha2):
      reflection_px_width = 30 # width of reflection in pixels
else:
   reflection_px_width = 6    # random value...

# Finding neutral strain value from avg DP from ref region:
spg_ref = SubpixelrefinementGenerator(ref_dpm,
    np.asarray([x_peak,y_peak]))
V_ref = spg_ref.center_of_mass_method(reflection_px_width)
unstr_gs = V_ref # c-o-m determined ref vectors

#Printing
print('camL =', camL, ', expT =', expT, ', alpha =', alpha)
print('used reflections:', x_peak, 'and', y_peak)
print('Used pixel width =', reflection_px_width)
print('com determined unstrained vectors:', np.asarray(unstr_gs))

# Creates matrix w. approx pos of DP spot in every DP:
spg = SubpixelrefinementGenerator(NW, np.asarray([x_peak,y_peak]))
# find center of mass pos of reflection:
Vs = spg.center_of_mass_method(reflection_px_width)
# find displacement from unstrained reflection unstr_gs:
D = get_DisplacementGradientMap(hs.signals.Signal2D(Vs), unstr_gs)

# Plot strain maps:
strain_map = D.get_strain_maps()
strain_map.plot(cmap='seismic', vmax=0.03, vmin=-0.03)

#Do line trace for normal strains:
# Select strain map to tak line trace of:
for i in range(2):
   strain = strain_map.inav[i]
   strain.plot(cmap='seismic', vmax=0.03, vmin=-0.03)

   # Trace along chosen strain map from start to stop:
   start = 1
   stop = 299
   trace_len = np.arange(stop-start+1)
   line = pxm.roi.Line2DROI(x1=35, y1=start, x2=35, y2=stop,
       linewidth=50)
   line.add_widget(strain)
   trace = line(strain)
   trace.plot('b')

   # Selection region to average and mark in strain map:
   if (use_index != 8): #211
      start_avg = 148
```

```
        stop_avg = 213
    else: #110
        start_avg = 114
        stop_avg = 185
    avg_len = stop_avg-start_avg

    # Plot averaging region on strain map:
    if (False):
        top = pxm.roi.Line2DROI(x1=5, y1=start_avg, x2=65,
            y2=start_avg, linewidth=1)
        bottom = pxm.roi.Line2DROI(x1=5, y1=stop_avg, x2=65,
            y2=stop_avg, linewidth=1)
        bottom.add_widget(strain)
        top.add_widget(strain)

    # Find avg strain and plot:
    insert = np.asarray(trace)
    insertStrain = insert[start_avg:stop_avg]
    print('avg strain in region',i,' = ',
        insertStrain.sum()/(stop_avg-start_avg))
```

O Code for EDX mapping

This code was developed by Aleksander B. Mosberg and edited by Dipanwita Chatterjee and given to me for EDS mapping.

```
%matplotlib qt
import hyperspy.api as hs
import numpy as np
import pandas as pd
import matplotlib as mpl
import matplotlib.pyplot as plt

eds = hs.load('./Run1\run1.hdf5')

elements = ["Ga", "As", "Sb", "C"]
eds.set_elements(elements)

eds.change_dtype('float')
eds_bin = eds.rebin(scale = (2,2,1)) #take care of the numbers
    you want to put in the scale parenthesis
eds_bin.plot()
eds_bin
```

```
eds.plot(xray_lines=True)
eds.sum().plot(xray_lines=True, only_lines=None)

#EDS quantification
eds_s = eds.sum()
eds_s.add_elements(elements)
eds_s.add_lines()
ms = eds_s.create_model()
ms.components

ms.plot()
ms.fit()
ms.plot(True, xray_lines='from_elements', only_lines=None)
ms.fit_background()
msi = ms.get_lines_intensity()
msi

k_lines_all = ['As_Ka', 'As_La', 'C_Ka', 'Cu_Ka', 'Cu_La',
    'Ga_Ka', 'Ga_La', 'O_Ka', 'Sb_La', 'Si_Ka']
k_factors_all = [ 2.835, 4.315, 2.283, 2.023, 5.281, 2.419,
    4.719, 1.815, 3.976, 1.0 ]

k_lines = ['As_Ka', "Ga_Ka", 'Sb_La']
k_factors = [ 2.835, 2.4919, 3.976 ]
k_elements = ['As', 'Ga', 'Sb' ]

msi_q = []

for line in k_lines:
   for peak in msi:
      if line == peak.metadata.General.title[12:18].replace("
         ",""):
         msi_q.append(peak)

msi_q

eds_s.set_elements(k_elements)
eds_s.set_lines(k_lines)

eds_s.set_elements(k_elements)
eds_s.set_lines(k_lines)
msq = eds_s.quantification(intensities=msi_q, method='CL',
    factors=k_factors)

totp = 0
for result in msq:
   name = result.metadata.General.title
   if name.startswith('atomic percent of'):
      name = name[18:]
   print("{:>10s} | At%: {:.2f} ".format(name,result.data[0]))
```

```
    totp += result.data[0]
print("\nPercentages sum: {:.6f}".format(totp))

cutoff = 12.5
print("Original cutoff {:.3f}
     kV".format(eds.axes_manager[-1].size*eds.axes_manager[-1].scale))
if eds.axes_manager[-1].size*eds.axes_manager[-1].scale > cutoff:
    eds.crop(-1, end=cutoff)
    print("New cutoff {:.3f}
         kV".format(eds.axes_manager[-1].size*eds.axes_manager[-1].scale))
else:
    print("Keeping cutoff")
eds.axes_manager

eds.add_elements(elements)
eds.add_lines()
meds = eds.create_model()

meds.components

meds.plot()

for comp in ms.as_dictionary()['components'][1:]:
    print(comp['name'])
    for param in comp['parameters']:
        print("    ", param['_id_name'], " ", param['value'])


params = ms.as_dictionary()['components']
params

for comp in params:
    print(comp['name'])
    for param in comp['parameters']:
        print(param['name'], " ", param['value'])
        meds.set_parameters_value(param['name'], param['value'],
            component_list=[comp['name']])

meds.print_current_values(only_free=False)

ms.print_current_values(only_free=False)

meds.assign_current_values_to_all()

meds.multifit()

#save:
meds.save('EDS with model GaAsSb', 'modelfit')
#load:
eds = hs.load('EDS with model GaAsSb.hspy')
```

```
meds = eds.models.restore('modelfit')

meds.plot(xray_lines='from_elements', only_lines=None)

medsi = meds.get_lines_intensity()
medsi

for map in medsi:
   map.T.plot()
   map.T.save(filename='Hyperspy
       plots/'+map.metadata.General.title, overwrite=True,
       extension='png')

k_lines_all = ['As_Ka', 'As_La', 'C_Ka', 'Cu_Ka', 'Cu_La',
    'Ga_Ka', 'Ga_La', 'O_Ka', 'Sb_La', 'Si_Ka']
k_factors_all = [ 2.835, 4.315, 2.283, 2.023, 5.281, 2.419,
    4.719, 1.815, 3.976, 1.0 ]

k_lines = ['As_Ka', "Ga_Ka", 'Sb_La']
k_factors = [ 2.835, 2.4919, 3.976 ]
k_elements = ['As', 'Ga', 'Sb'  ]

medsi_q = []

print(k_lines)

for line in k_lines:
   for peak in medsi:
      if line == peak.metadata.General.title[12:18].replace("
          ",""):
         medsi_q.append(peak)

medsi_q

eds.set_elements(k_elements)
eds.set_lines(k_lines)
edsq = eds.quantification(intensities=medsi_q, method='CL',
    factors=k_factors)

eds.metadata

for map in edsq:
   map.T.plot(cmap='viridis')
   #map.T.save(filename='Hyperspy
       plots/'+map.metadata.General.title, overwrite=True,
       extension='png')
```

P Other smaller calibration codes

```
%matplotlib qt
import numpy as np
import pyxem as pxm

# PRECESSION ANGLE CALIBRATION:
myFile = './torit_Au_20cm_100x100-10_noDescan.hdf5'

intensity = 150

pre_process = False

radial_profile_mthd = True
line_mthd = False
DF_ring_mthd = False
save_dpm = False
#upload file and plot:
dp = pxm.load_hspy(myFile, assign_to='electron_diffraction2d')
dp.set_experimental_parameters(accelerating_voltage = 200., #kV
                               camera_length    = 20,     #cm
                               exposure_time    = 10.)    #IDK, 10 for
                                    now...
dp.metadata.set_item("General.title", 'Au grid')

# --- Set calibration of DP and scan: --- #
recip_d111 = np.sqrt((3/5.6535**2))                    # -> 5.6535=a_GaAs
recip_cal = 1#recip_d111 / 9.6                          # From random
    GaAs w. cam L = 20cm
dp.set_diffraction_calibration(recip_cal)
print(recip_cal)

scan_cal = 8.3                                         #(nm/pix)
    200x200_10 = 8.3, 200x200_20 = 19.9
dp.set_scan_calibration(scan_cal)                      # 1 for pixel
    dimensions

if (pre_process):
   dp.remove_background(method='median', footprint=12)

# Find radii of precessed beam on viewing screen:
if (recip_cal == 1):
   roi = pxm.roi.CircleROI(cx=-4,cy=-4, r_inner=0, r=14)
   line = pxm.roi.Line2DROI(x1=-25, y1=-4, x2=20, y2=-4,
       linewidth=10)
else:
   roi = pxm.roi.CircleROI(cx=-0.14,cy=-0.14, r_inner=0, r=0.44)
   line = pxm.roi.Line2DROI(x1=-1, y1=-0.14, x2=1, y2=-0.14,
```

```
       linewidth=0.2)

if (radial_profile_mthd):
   dp.plot(cmap='inferno', vmax=intensity)
   rp = dp.get_radial_profile()
   rp.plot()
elif (line_mthd):
   dpm = dp.inav[65:66, 57:58].mean((0,1))
   dpm.plot(cmap='inferno', vmax=intensity)
   if (save_dpm):
      dpm.change_dtype('float32')
      dpm.save(myFile[0:-5]+'_DP.tif')
   else:
      line.add_widget(dpm)
      trace = line(dpm)
      trace.plot()
elif (DF_ring_mthd):
   dp.plot_interactive_virtual_image(roi=roi, cmap='inferno',
       vmax=intensity)

#RECIPROCAL CALIBRATION AND ALPHA ANGLE CALIBRATION:
NW2_bottom = np.asarray([
   './torit_NW2_300x300-2_L20_A3_AP3_x_y_z_tx_ty_20ms_preProcessA.hdf5'])

use_index = 1
file = NW2_bottom[use_index]

NW    = pxm.load_hspy(file, assign_to='electron_diffraction2d')

camL  = int(file.split('_')[-10][1:3])
expT  = np.int(file.split('_')[-2][0:2])
alpha = file.split('_')[-9]+file.split('_')[-8]

intensity = expT*10

print('camL =', camL, ', expT =', expT, ', alpha =', alpha)

NW.set_scan_calibration(1) # 1 for pixel dimensions
NW.set_diffraction_calibration(1) # 1 for pixel dimensions

# Find reflection width from linetrace:
NW.plot()
ref_reg = pxm.roi.RectangularROI(left=25, top=235, right=45,
    bottom=255)
ref_dp = ref_reg(NW)
ref_dpm = ref_dp.mean((0,1)) # take mean of region
ref_reg.add_widget(NW) # add in DP, green square
ref_dpm.plot(vmax=intensity)

line = pxm.roi.Line2DROI(x1=-72, y1=0, x2=72, y2=0, linewidth=15)
```

```
line.add_widget(ref_dpm)
trace = line(ref_dpm)
trace.plot()

#Do recipcal calculations from linetrace:
#Facts:
g_022 = 0.500 # A^-1
g_111 = 0.306 # A^-1

#Found from trace:
used_g = g_022
peak1 = 25.3
peak2 = 72
peaks = 1

g_spacing_px = (peak2-peak1)/peaks

recip_cal = used_g/g_spacing_px

print('recip_cal =', recip_cal, 'for camL =', camL)

#Do alpha calculations from linetrace:
L_e   = 2.5079*10**-12 # [m] wavelength e at 200keV
used_g = g_022*10**10 # [m^-1]
theta = np.arcsin(L_e*used_g/2)

#reflection edges found from trace:
edge1 = 21.4
edge2 = 29.4

spot_width_px = edge1-edge2

alpha = theta*np.abs(spot_width_px/g_spacing_px)

print('alpha angle =', alpha*1000, 'mrad')

#SCAN STEP CALIBRATIONS:
myIms = np.asarray(['./torit_Au_20cm_200x200-10_VDF.tif'])

myLns = np.asarray([pxm.roi.Line2DROI(x1=35, y1=5, x2=197,
    y2=197, linewidth=20)]) #200x200_10

#number of Au cross grid squares along line:
nSqr = [4]

#first grid and last grid positions:
myPos = [[15.,242.]]

to_do = 5
```

```
myIm = myIms[to_do - 1]
line = myLns[to_do - 1]

au_im = pxm.load_hspy(myIm, assign_to='electron_diffraction2d') #
    scan img for pixl calib

cal_lib = CalibrationDataLibrary(au_x_grating_im=au_im)

cal_lib.plot_calibration_data(data_to_plot='au_x_grating_im')

cal = CalibrationGenerator(calibration_data=cal_lib)

cal_lib.plot_calibration_data(data_to_plot='au_x_grating_im',
    roi=line)

trace = line(cal_lib.au_x_grating_im).as_signal1D(0)
trace.plot()
```

Tor Inge Thorsen

Master thesis at NTNU

NTNU
Norwegian University of
Science and Technology